Utrecht University

# Master Thesis – Final Report

Energy Science
Utrecht University

## Partial Shade-Mitigating Effects of Ideal Bypass Diode Insertion in Residential-Scale PV Systems


### Contact Details

Tom Rooijakkers
t.t.h.rooijakkers@students.uu.nl

### Host Institute

Solar Energy Application Centre
High Tech Campus 21, 5656AE, Eindhoven

### Supervisors

K. Sinapis MSc (SEAC Eindhoven)
G.B.M.A. Litjens MSc (Utrecht University)

### Readers

dr. W.G.J.H.M. van Sark (Utrecht University)
B. Elsinga MSc (Utrecht University)


### Date

April 17th, 2016

## Abstract

This study focuses on the partial shade-mitigating effects related to the insertion of additional ideal by-pass diodes in residential-scale photovoltaic (PV) systems. For this purpose, quantification of the resulting energy yield benefits is carried out in a representative residential environment. Similar studies addressed the effects of partial shading on PV system output. It is widely recognized that partial shading inflicts disproportional losses to the energy output of PV systems. By-pass diodes are perceived as a potentially promising measure to increase the shade-tolerance of photovoltaic devices. However, most of the similar work either applied time-independent shading characteristics in their analysis or neglected the effects of by-pass diode insertion. The research presented here uses a novel and flexible energy yield model that is based on the physical description of PV systems. In this model the amount of by-pass diodes is incrementally increased from 3 to 5, 10, 12, 30 and 60 per module of 60 cells. The three considered PV system architectures include a central string inverter, per-module power optimizers and per-module micro-inverters. In the main model simulation run, the PV system is located in Eindhoven, The Netherlands and oriented southward with a tilt of 40°. A sensitivity analysis includes various roof orientation directions and various geographic locations in Europe.

The results of this work show that up to 60% of the shade-induced system output losses occurring in the reference case of 3 by-pass diodes are recoverable in the case of 60 by-pass diodes per module depending on the chosen system architecture. Overall the output of the central string-inverter-based PV system is most beneficially affected by the implementation of additional by-pass diodes. Furthermore the validation results of the energy yield model used here show good agreement with a yield model applied in former work. Another observed trend is the profound degree of consistency related to the recoverable fraction of shade-induced system output losses throughout the sensitivity simulations. This means that increasing the amount of by-pass diodes gives way to PV system efficiency improvements in a wide range of partial shading conditions. Consequently, if the economic benefits of increased PV system energy output related to by-pass diode insertion turn out to exceed the associated implementation costs, a widespread sales market for PV systems containing high amounts of by-pass diodes may develop in the future. Therefore economic cost-benefit assessments are recommended to be the focus of interest in future research efforts.

---

Keywords: photovoltaics, modeling, ideal bypass diodes, residential PV system, partial shading, specific energy yield, string inverter, micro-inverter, power optimizer, residential built environment, maximum power point tracking granularity, by-pass diode topology, typical meteorological year simulation, c-Si module, PV substrings, system output optimization, simplified double-diode PV cell model, IV curve algorithm, cell shade algorithm.

## Acknowledgements

This Master Thesis provides an overview of the results of six months of full-time research efforts as a part of fulfilling the requirements for the Energy Science Master programme at Utrecht University (UU). The research efforts have predominantly been carried out at Solar Energy Application Centre (SEAC) in Eindhoven, while frequent progress meetings took place at Utrecht University.

First of all I would like to thank Kostas Sinapis for providing me the opportunity to conduct this research at SEAC, for the on-site supervision and for the valuable comments that significantly improved the quality of this study. I also want to thank Chris Tzikas in particular for his excellent outline of the essences of the energy yield model when I started this research project and for the detailed, high-quality feedback on intermediate versions of this report in later stages. Also the discussions with the fellow students and interns at SEAC have been very stimulating.

With regard to the proceedings on Utrecht University, I would firstly like to express my gratitude towards Geert Litjens for his frequent supervision, his excellent suggestions regarding the overall report and for his extremely helpful data visualization suggestions. Also a word of thanks to the fellow Energy Science students in the "Master Thesis Support Group" for the elaborate and fruitful feedback sessions. On top of that I would like to thank Boudewijn Elsinga for being the second reader of this Thesis assessment. Finally I would like to address words of thanks to Wilfried van Sark for the invitations to the PV research team meetings and for being the first reader with regard to the examination of this Master Thesis research.

Outside the Thesis research proceedings my family and closest friends provided me listening ears whenever needed. I would hereby also like to warmly thank them for their continuous support.

## Outline of Report

The general outline of this report is as follows. Chapter 1 treats the introduction, the justification of this research and the place of this work within literature in the same field. Chapter 2 elaborates on the scientific theories and key prior findings necessary for conducting the methodological framework in this study. Chapter 3 outlines the used methodology with regard to the modeling procedure. The focus lies on the determination of the input variables required for the modeling procedure and its individual steps. Chapter 4 lists the key results of this study. Chapter 5 discusses the results, approximations within the chosen methodology and the implications of the results. Chapter 6 of this work delivers the research conclusions. These answer the key research question and its related sub-questions. Chapter 7 finally mentions the key recommendations for future research.

# Table of Contents

## List of Acronyms & Abbreviations

| | |
|---|---|
| AC | Alternating current |
| AM | Air mass coefficient |
| AOI | Angle of incidence |
| BPD | By-pass diode |
| BS | Bisection search |
| CO | Carbon monoxide |
| $CO_2$ | Carbon dioxide |
| DC | Direct current |
| GHG | Greenhouse gas |
| GHI | Global horizontal irradiance |
| IAM | Incident angle modifier (factor) |
| IV | Current-voltage |
| LB | Left-bottom |
| LT | Left-top |
| MLPE | Module-level power electronics |
| MLPM | Module-level power management (former SEAC project) |
| MPP | Maximum power point in an IV curve |
| NOCT | Nominal operating cell temperature |
| $NO_x$ | Nitrogen oxides |
| NR | Newton-Raphson |
| POA | Plane-of-array |
| PB | Potential benefits of applying additional BPDs inside a PV system |
| PM | Particulate matter |
| PR | Performance ratio |
| PV | Photovoltaic |
| RB | Right-bottom |
| RHS | Right-hand side |
| RT | Right-top |
| SIDX | Shading index |
| SMF | Shade mitigation factor |
| $SO_2$ | Sulfur dioxide |
| SRH | Shockley-Read-Hall (recombination effect) |
| STC | Standard test conditions for solar cells ($G_{STC}$ = 1000 W/m², $T_{STC}$ = 25 °C, AM = 1.5) |
| TMY | typical meteorological year |
| VOCs | Volatile organic compounds |

## List of Symbols

| | | *Unit* |
|---|---|---|
| $\alpha_H$ | horizontal direction coordinate on cell panel grid | [-][1] |
| $\alpha_{RA}$ | apparent right ascension of the Sun | [°] |
| $\alpha_V$ | vertical direction coordinate on cell panel grid | [-] |
| $\gamma_{azi}$ | solar azimuth angle (0° = N; 90° = E; 180° = S; 270° = W) | [°] |
| $\gamma_{alt}$ | solar altitude angle (0° = horizon level; 90° = zenith point) | [°] |
| $\delta$ | solar declination angle | [°] |
| $\delta_{step}$ | step delta for variable in iteration algorithm | [-] |
| $\varepsilon$ | maximum allowed approximation error in (iteration) algorithm | [-] |
| $\varepsilon_{ecl}$ | angle of the ecliptic | [°] |
| $\varepsilon_I$ | maximum allowed error for current in iteration algorithm | [-] |
| $\varepsilon_P$ | maximum allowed error for power in iteration algorithm | [-] |
| $\zeta$ | cell number (horizontal cell configuration) | [-] |
| $\zeta_V$ | cell number (vertical cell configuration) | [-] |
| $\theta_{AOI}$ | direct sunlight angle of incidence on a plane | [°] |
| $\theta_R$ | radial arc angle | [rad] |
| $\theta_{ra}$ | angle of refraction | [°] |
| $\kappa_{azi}$ | point-of-array (POA) azimuth angle (0° = N; 90° = E; 180° = S; 270° = W) | [°] |
| $\kappa_T$ | point-of-array (POA) tilt angle (0° = horizon level; 90° = zenith point) | [°] |
| $\lambda_{lon}$ | longitudinal angle of location on Earth | [°] |
| $\nu$ | number of evaluated points per cell dimension (width and height) | [-] |
| $\nu_{ij}$ | evaluation point in cell grid ($0 < i, j \leq \nu$-1 for LB points) | [-] |
| $\nu_S$ | number of evaluated points of a cell lying in a shade polygon | [-] |
| $\xi$ | line-plane intersection point / on-plane shade projection point | [m] |
| $\xi_n$ | line-plane intersection point belonging to shade object edge point *n* | [m] |
| $\xi_p$ | interior shade object-plane intersection point | [m] |
| $\rho_A$ | albedo reflection factor | [-] |
| $\sigma_P$ | cell shading percentage | [%] |
| $\varphi_{i-1}$ | polar angle of shade intersection point with respect to point with $y_{min}$(, $x_{min}$) | [rad] |
| $\varphi_{lat}$ | latitude angle of location on Earth | [°] |
| $\omega_{GHA}$ | Greenwich hour angle | [°] |
| *a* | plane equation constant associated with *x*-component of normal vector | [-] |
| $B_s$ | semiconductor material coefficients related to series resistance | [-] |
| $B_{sh}$ | semiconductor material coefficients related to shunt resistance | [-] |
| *b* | plane equation constant associated with *y*-component of normal vector | [-] |
| $b_0$ | factor corresponding to refractive index of PV glass cover (~0.05) | [-] |
| $C_Y$ | ecliptic longitude of the Sun | [°] |
| *c* | plane equation constant associated with *z*-component of normal vector | [-] |
| D | circular diameter | [m] |
| *d* | plane equation constant related to position of plane in space | [-] |
| $E_g$ | band gap of silicon | [eV] |
| $E_{g,\,STC}$ | band gap of silicon @ STC (1.12 eV) | [eV] |
| $E_L$ | elevation above sea level | [m] |
| $E_{rated}$ | rated capacity of the PV system (2.385 $kW_p$ in this study) | [$kW_p$] |
| $E_{spec}$ | specific absolute energy yield | [$kWh/kW_p$] |
| $E_{tot}$ | total absolute energy yield | [kWh] |
| $F_{IAM}$ | incidence angle modifier (loss) factor | [-] |

[1] [-] represents a (net) dimensionless unit.

| | | |
|---|---|---|
| $G$ | irradiance casted on solar cell or module (general notation) | [W/m²] |
| $G_B$ | (normal) beam irradiance | [W/m²] |
| $G_{diff,k}$ | diffuse in-plane irradiance | [W/m²] |
| $G_{dir,k}$ | direct in-plane irradiance | [W/m²] |
| $G_{G,k}$ | global in-plane irradiance | [W/m²] |
| $G_{GHI}$ | global horizontal irradiance | [W/m²] |
| $G_{S,k}$ | shaded effective in-plane irradiance (= $G_{diff,k}$) | [W/m²] |
| $G_{U,k}$ | unshaded effective in-plane irradiance | [W/m²] |
| $G_Y$ | mean anomaly of Sun's position (0° – 360°) | [°] |
| $I$ | output current | [A] |
| $I_{in}$ | conversion step input current | [A] |
| $I_{MPP}$ | module output current @ MPP | [A] |
| $I_{o,1}$ | reverse saturation current of first diode in double-diode cell model | [A] |
| $I_{o,2}$ | reverse saturation current of second diode in double-diode cell model | [A] |
| $I_{ph}$ | photo-generated current | [A] |
| $I_{ph,\,STC}$ | photo-generated current @ STC | [A] |
| $I_{SC}$ | short-circuit current condition | [A] |
| $I_{SC,\,m}$ | module short-circuit current | [A] |
| $I_{SC,\,s}$ | substring short-circuit current | [A] |
| $I_{sys}$ | PV system (component) output current | [A] |
| $i_R$ | index of refraction of PV glass cover | [-] |
| $J$ | current density of a PV system component | [A/cm²] |
| $K$ | glazing extinction coefficient | [m$^{-1}$] |
| $K_I$ | module temperature coefficient of current | [A/K] |
| $K_P$ | module temperature coefficient of power | [W/K] |
| $K_V$ | module temperature coefficient of voltage | [V/K] |
| $k_B$ | Boltzmann's constant ($1.38064852 \cdot 10^{-23}$ J/K) | [J/K] |
| $k_{H,1}$ | line parameterization constant; first horizontal shade object rib direction | [-] |
| $k_{H,2}$ | line parameterization constant; second horizontal shade object rib direction | [-] |
| $k_V$ | line parameterization constant; vertical shade object rib direction | [-] |
| $L$ | list parameter | [-] |
| $L_g$ | glazing thickness | [m] |
| $L_Y$ | solar mean longitudinal term corrected for aberration (0° – 360°) | [°] |
| $M_{corr}$ | adjusted month number in Yallop's algorithm | [-] |
| $N_{bpd}$ | number of bypass diodes in a PV module | [-] |
| $N_H$ | amount of cells stacked horizontally on cell panel grid | [-] |
| $N_P$ | total number of points describing an object | [-] |
| $N_p$ | number of cells connected in parallel per module | [-] |
| $N_s$ | number of cells connected in series per module | [-] |
| $N_V$ | amount of cells stacked vertically on cell panel grid | [-] |
| $\hat{\boldsymbol{n}}$ | normal vector of unit length | [-] |
| $n$ | point number of shading object or panel edge point | [-] |
| $n_1$ | quality factor of first diode in double-diode cell model | [-] |
| $n_2$ | quality factor of second diode in double-diode cell model | [-] |
| $q_e$ | electron unit charge ($1.60217662 \cdot 10^{-19}$ A·s) | [A·s] |
| $P_{MPP}$ | module power output @ MPP | [W] |
| $P_{loss}$ | absolute power losses associated with conversion step | [W] |
| $R_s$ | cell series resistance in double-diode model | [Ω] |
| $R_{s,\,s}$ | substring series resistance in double-diode model | [Ω] |
| $R_{sh}$ | cell shunt resistance in double-diode model | [Ω] |

| | | |
|---|---|---|
| $R_{sh,\,s}$ | substring shunt resistance in double-diode model | [Ω] |
| $S_C$ | number of series-connected cells per substring | [-] |
| $s_X$ | *x*-component of Sun-to-Earth direction vector | [-] |
| $s_Y$ | *y*-component of Sun-to-Earth direction vector | [-] |
| $s_Z$ | *z*-component of Sun-to-Earth direction vector | [-] |
| T | temperature (general notation) | [K; °C] |
| $T_a$ | ambient temperature | [°C] |
| $T_c$ | solar cell temperature | [K] |
| $T_s$ | substring temperature | [K; °C] |
| $T_U$ | universal time (UTC) | [h] |
| $T_m$ | solar module temperature | [K] |
| $T_Y$ | Julian timestamp | [100 yr] |
| $T_{z,\,loc}$ | time zone (deviation from UTC) | [h] |
| t | line parameterization constant for determining shade-plane intersect | [-] |
| $t_n$ | line parameterization constant belonging to shade object edge point *n* | [-] |
| $U_0$ | constant heat transfer component in Faiman temperature model | [W/(m²K)] |
| $U_1$ | convective heat transfer component in Faiman temperature model | [W/(m³Ks)] |
| $\vec{u}$ | unit horizontal direction vector on cell panel grid | [-] |
| $\vec{V}_{BT}$ | bottom-top (vertical) directional vector on cell panel grid | [m] |
| $\vec{V}_{LR}$ | left-right (horizontal) directional vector on cell panel grid | [m] |
| $\vec{V}_N$ | vector normal to (panel) plane | [m] |
| $\vec{V}_{sol}$ | unit-length Sun-to-Earth direction vector with components $s_X$, $s_Y$, $s_Z$ | [-] |
| $V_c$ | solar cell voltage | [V] |
| $V_{sys}$ | PV system (component) voltage | [V] |
| $V_{MPP}$ | module voltage @ MPP | [V] |
| $V_{OC}$ | open-circuit voltage condition | [V] |
| $V_{OC,\,m}$ | module open-circuit voltage | [V] |
| $V_{OC,\,s}$ | substring open-circuit voltage | [V] |
| $V_{op}$ | operating voltage | [V] |
| $V_{th}$ | thermal voltage | [V] |
| $\vec{v}$ | unit vertical direction vector on cell panel grid | [-] |
| $\vec{v}_{H1}$ | first horizontal direction vector on first horizontal rib of shade object | [-] |
| $\vec{v}_{H2}$ | second horizontal direction vector on 2nd horizontal rib of shade object | [-] |
| $\vec{v}_V$ | vertical direction vector on vertical rib of shade object | [-] |
| $W_{FF}$ | wind speed | [m/s] |
| $x_c$ | central circular *x*-coordinate | [m] |
| $x_{LB,\,c}$ | *x*-coordinate of left-bottom cell edge point | [m] |
| $x_{p,\,n}$ | *x*-coordinate of point with point number *n* | [m] |
| $Y_{corr}$ | corrected year number in Yallop's algorithm | [-] |
| $y_c$ | central circular *y*-coordinate | [m] |
| $y_{LB,\,c}$ | *y*-coordinate of left-bottom cell edge point | [m] |
| $y_{p,\,n}$ | *y*-coordinate of point with point number *n* | [m] |
| $z_{BC}$ | *z*-coordinate of bottom cylindrical surface (center point) | [m] |
| $z_{LB,\,c}$ | *z*-coordinate of left-bottom cell edge point | [m] |
| $z_{p,\,n}$ | *z*-coordinate of point with point number *n* | [m] |
| $z_{TC}$ | *z*-coordinate of top cylindrical surface (center point) | [m] |

# Chapter 1: Introduction

This introductory chapter is structured as follows. § 1.1 illustrates the societal background and introduces the research topic. § 1.2 outlines the terminology of key definitions related to this work. The scientific background of similar literature is listed in § 1.3. The working principle of applying additional by-pass diodes in PV modules is illustrated in § 1.4. Finally, § 1.5 provides the research question framework related to the presented research.

## 1.1 – Societal background & study topic

Photovoltaic (PV) energy technologies are becoming increasingly prominent in the global energy mix. Global cumulative capacity rose from 3 GW in 2003 to 139 GW in 2013 (EPIA, 2014). EPIA (2014) further foresees a more-than-doubling of capacity to 375 GW in 2018 and a continuation of market growth towards 2030. What is more, PV is considered to be one of the fastest-growing industries worldwide (Tyagi, Nurul, Rahim, & Selvaray, 2013). These trends are thought to be closely related to vast PV cost reductions over the last years (IEA, NEA & OECD, 2015).

The environmental benefits of increasing the level of PV in the energy mix at the cost of fossil-fuel based technologies are widely recognized. One of the key factors is the low intensity of greenhouse gas (GHG) emissions associated with PV technologies. Another key issue is that, contrary to fossil fuel plants (EEA, 2008), PV plant energy generation is not associated with local pollution from the release of $SO_2$, $NO_x$, CO, volatile organic compounds (VOCs), particulate matter (PM) or residual flue gases. These compounds have a direct adverse effect on the environment as well as on human health (Kampa & Castanas, 2008). Additional societal benefits related to PV technologies include the potential development towards energy independency on residential, local and national levels and the opportunity to cost-effectively electrify remote rural areas in developing countries (Williams, Jaramillo, Taneja, & Ustun, 2015).

Besides industrially and commercially installed PV systems, the mentioned forecasted photovoltaic market growth (EPIA, 2014) is expected to boost the deployment of PV systems in the residential environment in the near and further future. However, inhomogeneous partial shading due to obstructions in the built environment has detrimental effects on performance in residential PV systems. Examples of these obstructions are chimneys, exhaust pipes and dormers. Residential PV systems traditionally consist of modules connecting cells in series and these systems are conventionally deployed with a single-phase central string inverter (Deline, Marion, Granata, & Gonzalez, 2011). This forces all modules in the system to operate at the same current and operating voltage levels. As a result the most heavily shaded cells limit the current and power that can be extracted from the system at the maximum power point (MPP) operating voltage.

If the irradiance on shaded cells is low compared to the irradiance on unshaded cells in the same series connection, the shaded cells can be forced to support current levels exceeding their characteristic short-circuit current. This may push the shaded into reverse voltage regimes where they start behaving as rectifying diodes (Twidell & Weir, 2006). As a consequence, thermal power dissipation by the cells in question causes excessive power losses, the formation of localized “hot spots” and possible permanent cell damage (Molenbroek, Waddington, & Emery, 1991). In extreme cases the negative voltage can reach levels sufficient for avalanche breakdown (McKay, 1954) to occur. This instantly and permanently disables the module. Nowadays most PV modules are equipped with bypass diodes per substring of 12-24 cells (MacAlpine, Brandemühl, & Erickson, 2011; Silvestre, Boronat, & Chouder, 2009) to prevent this type of breakdown. However,

this comes at a cost of performance due to a significant voltage drop (~0.4 V) for each bypass diode in operation (Pannebakker, 2014). This is one of the main reasons that the use of traditional Schottky-type bypass diodes is limited in standard PV modules.

Nevertheless, new products have been introduced on the market in recent years. This is caused by the commercial development of per-module PV power electronics. Generally these products fall into the categories of DC-DC conversion power optimizers and AC micro-inverters (Deline, Marion, Granata, & Gonzalez, 2011). These types of devices are also referred to as distributed power electronics or module-level power electronics (MLPE). This is because power optimizers (POs) and micro-inverters (MIs) optimize the MPP and distributed power per module instead of for the entire PV system at once. As discussed before, this system-level bulk treatment holds for residential PV systems with traditional string inverter (SI) power electronics.

Another important recent development is the introduction of active bypass diodes. The key benefit is that active bypass diodes are associated with much smaller voltage drops than the preceding Schottky-type bypass diodes (MacAlpine, Brandemühl, & Erickson, 2011). Therefore these recently emerged "smart" bypass diodes are applicable for high degrees of integration within solar modules. This could even be up to the per-cell level (MacAlpine, Brandemühl, & Erickson, 2011). Consequently, smart bypass diodes can be used to improve PV module and system performance under partial shading (Woyte, Nijs, & Belmans, 2003; Pannebakker, 2014).

Recent work in the field showed annual PV system output benefits of 5 % to 30% when increasing the amount of power-optimizing devices within PV systems. More details are explained in the scientific literature summary outlined in § 1.3. Social benefits related to these devices include promising increases in specific ($kWh/kW_p$) and spatial ($kW_p/m^2$) efficiencies of PV systems. However, the use of power optimizers and micro-inverters at system levels below the module level can become costly in economic terms. In this sense, combining an intensified amount of active by-pass diodes with per-module power optimization as in general PO- and MI-type system architectures may prove to be both a cost-effective and energetically favorable option that deserves more attention.

Consequently, the study presented here is set up to quantify the performance benefits of increasing the amount of bypass diodes (BPDs) per module in an exploratory fashion. The performance benefits are evaluated for string inverter (SI), power optimizer (PO) and micro-inverter (MI) residential PV systems placed on a representative Dutch reference roof. Obstacles common in the built environment are incorporated on this roof. These obstacles cause partial shading on the PV system from time to time.

As for the case of applying more power-optimizing devices in PV systems, the insertion of additional BPDs may result in promising increases in specific ($kWh/kW_p$) and spatial ($kW_p/m^2$) PV system efficiencies in densely packed residential areas. This can in turn accelerate the development towards (near) energy-neutral buildings since their roof space is generally limited. On a higher level, successful demonstration of intensified BPD insertion may facilitate faster penetration of renewables in the energy mix of countries with high degrees of densely populated areas. Generally the spatial limitations due to the presence of obstacles are severe in those areas. Furthermore, implementing additional BPDs in new PV systems only requires slight adaptations of the current standard technology. This facilitates easy implementation into new PV systems. Consequently there could be a future market for PV systems with intensified degrees of BPD implementation. In this light, this work assesses the energetic benefits in an exploratory fashion whereas future economic cost-benefit studies can be set out to assess the market (size) potential.

## 1.2 – PV system components & terminology

The terminological convention for PV system parts and frequently occurring concepts in this study are outlined here for clarity purposes. Figure 1.2a shows all PV system parts of interest here.

*Array*: Indicates the PV system as a whole. In this study the simulated PV systems are fully connected in series – equivalent to the term "string" (of modules) used in similar literature.

*Energy yield:* Annual energy production in kWh or specified to kWh/$kW_p$. Used in strong connection with performance and (system) efficiency in this report.

*Granularity*: Increasing the amount of groups or substrings in a panel means that the system granularity increases; vice versa for a decrease.

*Group (of cells)*: see Substring.

*Local MPP*: local maximum in the IV curve of a PV system (component). Usually *not* the maximum for which the maximum power is achieved.

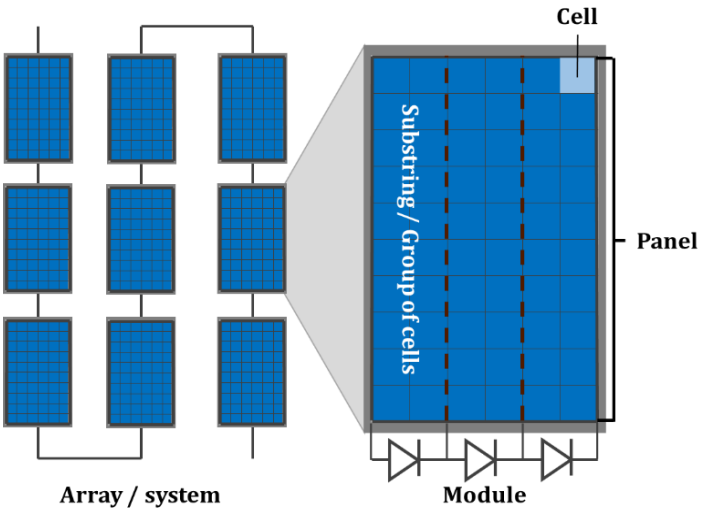


*Figure 1.2a: Visual representation of all PV system component levels of interest in this study. In this example, the PV panel containing 60 cells is sudivided into 3 substrings or cell groups of 20 cells each. The 9 series-connected modules form the PV system used in this study.*

*Micro-inverter (MI)*: Power electronic device architecture in which both the tracking of the MPP and DC-to-AC conversion are handled per module. Also see Figure 1.2d.

*Mismatch losses:* Usually PV module manufacturers bin modules within a nominal capacity range of 5W or 10W, meaning that PV modules sold within same rated power category will in reality have slight offsets in power generation under the same conditions[2].

*Module*: PV system component containing 60 cells, *X* bypass diodes, *X* substrings, 60/*X* cells per substring and an envelope on each rectangular side.

*MPP*: Maximum power point in the IV curve of a PV system (component). Indicates the global maximum (for which the maximum power output is achieved) unless mentioned in a general fashion.

*Panel*: Same as Module, but without the envelope on each rectangular side.

*Power optimizer (PO):* Power electronics configuration in which the MPP is set per module in this study. The power optimizer converts panel DC to DC at a steady voltage. In this study a grid-connected residential PV system is assumed. This requires the use of a special central inverter for DC-to-AC conversion. Also see Figure 1.2c.

[2] For instance, a 265$W_p$ panel sold on the market can have an actual rated capacity of 265 ± 2.5 $W_p$.

*String inverter (SI):* Power electronics configuration used in traditional PV system architectures. The entire (series-connected) system operates under the same MPP voltage and current. DC-to-AC conversion takes place at the central inverter. Despite its relative simplicity and high efficiency under homogeneous conditions, this system is rather inefficient in all other cases (including partial shading). Also see Figure 1.2b.

*Substring*: Series-connected part of a PV module covered by a single bypass diode. Used as a synonym for (cell) group in this study. In a panel of 60 cells, the number of (cell) groups $X$ is equivalent to substring sizes of $60/X$ cells each.

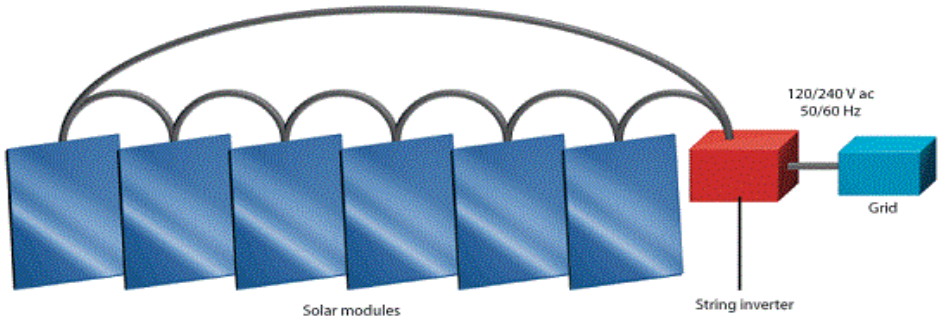


*Figure 1.2b: Conceptual illustation of a string inverter (SI) architecture for a PV system (Renewable Green Energy Power, 2015). System-level DC-to-AC conversion and MPP setting both take place at the central (string) inverter.*

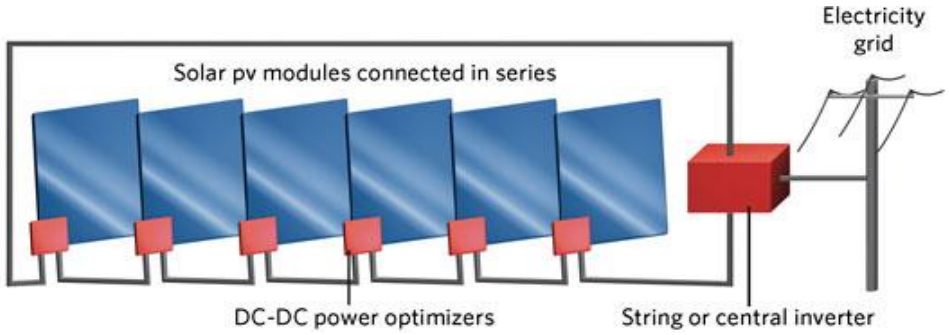


*Figure 1.2c: Conceptual illustration of a power optimizer (PO) architecture for a PV system (EnecSys, 2015a). Power optimizers set the MPP per individual module. For a grid connection, system-level DC-to-AC conversion takes place at the central inverter.*

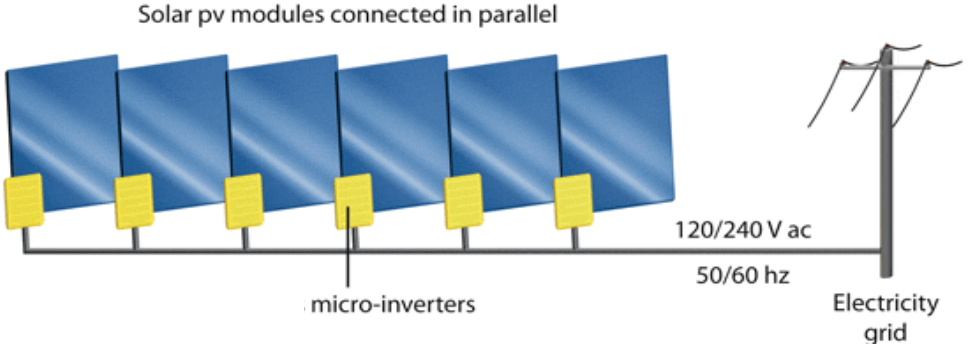


*Figure 1.2d: Conceptual illustration of a micro-inverter (MI) architecture for a PV system (EnecSys, 2015b). Micro-inverters set the MPP per individual module. DC-to-AC conversion is also done directly at the individual module level.*

## 1.3 – Scientific background

The relation between bypass diode configurations in solar energy modules and module response to conditions of partial shading was already identified in the 1980s (Swaleh & Green, 1982; Hasyim, Wenham, & Green, 1986). The recent commercial development of power optimizers, micro-inverters and smart bypass diodes as discussed in § 1.1 has led to widespread interest in quantifying the potential energy generation benefits related to applying these devices in common (c-Si) PV system architectures. The most important contributions in this field are listed in this paragraph.

Koirala & Henze (2009) compared current-voltage (IV) and power-voltage curves of string inverter (SI), power optimizer (PO) and micro-inverter (MI) module types with varying amounts of active bypass diodes by means of a mathematical simulation model. Simple shading scenarios with STC-irradiance as a benchmark and fixed-intensity shading on fixed amounts of cells were applied (Koirala & Henze, 2009). Although the quantified performance gains were highly sensitive to the applied shading scenario, PV systems with POs and MIs were generally found to lead to performance benefits compared to the SI-type reference.

Deline, Marion, Granata & Gonzalez (2011) found in their performance and economic analysis of POs and MIs that 10% to 30% of annual shade-related performance losses or more can be recovered depending on the PV system configuration and module specification. The authors of this reference listed increased safety, more flexibility in tailored system design, added monitoring and more thorough performance evaluation as additional benefits of PO/MI implementation. Listed disadvantages were implementation costs, additional system components prone to failure and insertion losses[3]. All in all, the authors concluded that the combination of all these factors "may or may not offset performance gains under particular mismatch conditions" (Deline, Marion, Granata, & Gonzalez, 2011). In the referenced work only the performance gains under individual shading and mismatch types (only row-to-row shading, only pole shading or string orientation mismatch) were studied or referred to.

Deline (2010) described a study with the full effect of partial shading conditions on annual energy yield figures of a residential PV system. However, no direct comparison assessment of PV system architectures (SIs, POs and MIs) was conducted. Shading was reported per hour and only related to energy losses using empirical relations rather than physical-principle-based relations.

Deline, Meydbray, Donovan & Forrest (2012) prepared shading test beds to test the effect of these test bed scenarios on the energy production of SI, PO and MI-type residential PV systems. The reported comparison of a MI-type with a SI-type system gave an annual energy gain of 4% to 12.6% in the MI-type compared to the SI-type depending on the shading intensity. The highest reported benefit figures were related to the most intense mesh shading used on specific parts of substrings. The meshes remained in fixed positions throughout the experiment. These findings also showed that significant energy yield benefits can arise from switching from array-level power optimization management (SI-type) to per-panel optimization (MI-type in the reference). However, the actual benefit again strongly depends on system-wise and environmental conditions. As a follow-up, Deline, Dobos, Janzou, Meydbrey & Donovan (2013) developed a simplified approach for predicting PV system yield figures under conditions of row-to-row shading in large-scale PV arrays.

[3] Insertion losses represent the system efficiency losses as a consequence of inserting more power-conversion devices (POs or MIs for example) into a PV system or its components. A similar convention can be used for BPDs.

Hanson, Deline, MacAlpine, Stauth & Sullivan (2014) reported on a partial shading assessment of over 500 PV installations via module-level monitoring. Power optimizer and string inverter system performances were compared. The referenced authors calculated that 36% of the power lost due to partial shading could be recovered by using per-module POs. This demonstrates a large benefit of distributing the power per module instead of for the bulk system. However, an important side note is that all PO systems were likely placed on roofs with higher-than-average shading effects. Therefore the recovered power figures may be above representative averages. In this referenced work shade was inferred from power losses. Consequently, no actual direct shade simulation related to any defined shading objects was done (Hanson, Deline, MacAlpine, Stauth, & Sullivan, 2014).

Belhachat & Larbes (2015) investigated different PV array configurations and their effect on optimal system power extraction under various conditions of partial shading. The studied electrical-circuit configurations are series, parallel, series-parallel, total-cross-tied, bridge-linked and honey-comb. Simple partial shading scenarios with the reference at STC-irradiance and shadow reductions as fractional reduced offsets from STC were used to make this assessment. The study found the optimal-performing array configuration to be highly dependent on the location and intensity of shading. Intensity of shading was measured as the irradiance reduction relative to STC-irradiance (Belhachat & Larbes, 2015).

Poshtkouhi, Palaniappan, Fard & Trescases (2012) quantified the benefits of incrementally increasing the amount of modeled DC-DC power optimizers from the system level to the module, substring and cell levels. Significant performance benefits were reported when the granularity was increased from the system level to the module level and from the module level to the substring level. In contrast, the benefits of increasing distributed power granularity from the substring level to the cell level were found to be limited. Absolute values of all results varied significantly depending on the intensity of shade in the modeled field. A SketchUp model was used to evaluate the shade on the studied systems on an hourly basis. It said to be the first report in the scientific field to adopt a strong simulation-oriented approach combined with real data measurements for validation and benchmarking (Poshtkouhi, Palaniappan, Fard, & Trescases, 2012).

MacAlpine, Brandemühl & Erickson (2011) modeled the potential for power recovery by the use of POs within a PV system to various degrees. A benchmark simulation using bypass diodes per cell was done for performance comparison purposes. Soiling[4] and inter-module mismatch losses were not considered. Two shading scenarios of one object each were investigated: a 1-foot diameter pole representing a utility pole and a 10-foot diameter opaque pole representing a tree. Both objects were centered 10 foot south of and extended 25 foot above a PV array on a single-story residence roof sloped ~22.5° facing due south[5]. It was found that the substring configuration strongly influenced the distributed PO power recovery potential. When the shadow was distributed along multiple (sub)strings, higher energy yield benefits were found compared to cases in which the shade only affects few or single (sub)strings. A cloudy climate (Orlando, Florida) harbored lower power recovery potential than a relatively sunny climate (Boulder, Colorado). This is explained by the fact that partial shading does not effectively occur on overcast days. The reason is that both the shaded and the unshaded parts of a PV system face the same (diffuse) irradiance levels on these days. Per-cell POs were demonstrated to offer the most pronounced energy yield benefits in both shading and climatological scenarios. This was very

[4] Soiling is defined as the accumulation of dust, debris and micro-organisms on solar panels, causing a decrease in the overall performance of a PV system (Mejia & Kleissl, 2013).
[5] The roof slope of 22.5° is a rounded approximation of the roof pitch value of 5/12 reported in the study.

closely followed by per-cell bypass diodes. However, the benefit offset of POs compared to per-cell bypass diodes increased for heavier shading scenarios. Another finding in the referenced work was that small shading obstacles generally gave less than 5 % potential power recovery without considering any insertion losses. This implies that shading must reach a certain level before power optimizers or extra bypass diodes in a PV system may start to become worthwhile from an energy perspective. Let alone if an economic perspective would be applied. This break-even level is highly dependent on PV system architecture, orientation, roof characteristics, direct environment and climatic conditions. Overall this conclusion reflects the key message of other similar work.

Pannebakker (2014) conducted a research in which a wide range of ways to improve the performance of PV modules under partial shading were studied. The application of additional by-pass diodes inside PV modules was studied as a part of that assessment. The partial shading conditions were created on a real module by the use of meshes of fixed opacity at fixed locations on the panel. The found performance benefits were strongly dependent on the shade intensity and the relative position of shade projections within the module. This is highly similar to the findings of the other studies listed here. Furthermore, Pannebakker (2014) reported a high endurance of the used smart bypass diodes. This was obtained from reliability tests done by Texas Instruments. Overall this fact is promising in terms of application of smart bypass diodes within PV modules.

Sinapis, Litjens, Van den Donker & Folkerts (2015) performed a field test to compare the real-time performance of SI, PO and MI-type PV systems placed adjacent to each other. The performance ratio (PR) was used as the primary performance indicator. PO and MI systems showed up to 35% higher PR-values than the SI system in certain partial shading conditions. However, the SI system showed the highest power conversion efficiency levels in unshaded conditions. Furthermore, the activation of a shadow function within the SI system marginalized the PO/MI advantage to 5%. This was caused by highly improved MPP tracking of this system compared to the non-shadow-mode setting. In a follow-up study, Sinapis et al. (in press) created a detailed energy yield model of the three aforementioned PV system architectures. The aim was to simulate the effect of various types of shades on their performance. In-field measurements were used to validate the simulation results of the model. Mesh shading experiments showed that shading half a cell of a module could impact the power up to fortyfold. Another finding was that the overall shade impact was significantly lower than anticipated. Overall the highest annual energy yield reduction found was 6.6 %. This value held for the string inverter system under partial shading. In turn, the shades were caused by a pole shading pattern (Sinapis, et al., in press). Also in this referenced work the calculated energy yield benefits were higher at locations facing higher levels of irradiance on a yearly basis. This was inferred from typical meteorological year (TMY) simulation results of locations throughout Europe (Sinapis, et al., in press). Tzikas (2015) elaborated on the technical methodology used to develop the referenced energy yield model.

Deeply intertwined with the recent emergence of power-optimizing electronics for PV applications is the interest in finding effective maximum power point tracking (MPPT) and PV cell modeling algorithms. The implementation of more devices within a PV system causes effective tracking of the MPP to become more cumbersome. This is caused by complicated current-voltage (IV) characteristics of the system under conditions of partial shading and high levels of inter-module mismatch. Examples of recent updated MPPT algorithm proposals and reviews are numerous (Bendib, Belmili, & Krim, 2015; Kotti & Shireen, 2015; Rizzo & Scelba, 2015; Sundareswaran, Vignesh, & Palani, 2015). This numerousness is also found on the scope of improving the electrical response simulation of PV cells and finding better-converging and faster

solar cell model algorithms[6] (Villalva, Gazoli, & Filho, 2009; Santos & Gaspar, 2011; Al-Hajri, El-Naggar, Al-Rashidi, & Al-Othman, 2012; Cotfas, Cotfas, & Kaplanis, 2013; Barth, Jovanovic, Ahzi, & Khaleel, 2015; Batzelis, Georgilakis, & Papathanassiou, 2015; Jena & Ramana, 2015). Development of faster and more accurate PV cell model algorithms is likely to continue to improve the computational performance PV system models under various irradiance conditions.

### 1.3.1 – Literature gap

Most of the work found on the performance of PV systems in relation to partial shading made use of fixed-position and fixed-intensity meshes and shading shapes for measuring or simulating the effects of partial shading. Proximate shading objects cast shade patterns on actual PV systems operating outdoors. These patterns move throughout the day and vary throughout the year. The cause of these shadow movements is seasonal differentiation of the Sun's path through the sky. PV system parts that are shaded receive in-plane diffuse irradiance while the unshaded areas receive full in-plane irradiance at a given time. Fixed shading fractions cannot be used to directly predict daily or annual effects of partial shading on the energy yield of a PV system. This is because the ratio of in-shade diffuse irradiance to total unshaded irradiance can vary substantially over the day. Some other studies used empirical relations and other means of indirect shading assessments to determine the shadow impact over extended periods of time. In these cases individual shading objects were not identified.

Four previous works with the aim to calculate annual energy yield figures for PV systems under partial shading by means of physical-principal-based simulation models and explicit use of proximal shading objects are identified here. As noted previously, Poshtkouhi, Palaniappan, Fard & Trescases (2012) and MacAlpine, Brandemühl & Erickson (2011) did so for the case of increasing the granularity of POs within central-inverter PV systems. The latter work also included a single case of applying active by-pass diodes per cell for comparison purposes. Sinapis, Litjens, Van den Donker & Folkerts (2015) and Sinapis et al. (in press) followed a similar methodology. The aim there was to compare the performance of a central string-inverter (SI) system with module-level distributed PO and MI residential-scale PV systems. In these two studies the amount of bypass diodes per module was kept fixed at three[7].

This work presents a novel study to simulate the effect of increasing the granularity of active by-pass diodes within three residential-scale PV systems of SI, PO and MI-type respectively. It directly builds forward on the work of Sinapis et al. (in press). The shading scenarios used in this study combine the effect of multiple types of shading objects frequently found in the built environment. This enables simulation of the aggregate system output loss effect and the influence of each separate shading object type on annual energy yield figures for all three system architectures.

From a scientific point of view, this research and its results are envisaged to encourage the further optimization of PV system simulation and monitoring procedures. Furthermore it is aimed to encourage the use of more advanced but representative shading conditions in future studies in the field. As explained in § 1.1, the study presented here is also aimed to provide valuable input for eventual future economic cost-benefit assessments related to intensified BPD-insertion in PV systems.

[6] Equation 2.17 provides an example of this equation under the assumption of a double-diode cell model.
[7] An alternative way of expressing this is that the amount of cells per substring in the modules of 60 cells each was fixed at 20 (= 60 / 3 BPDs). Also see § 1.2.

## 1.4 – By-pass diode insertion principle

This paragraph gives an example of the principle behind implementing additional of smart bypass diodes in a PV module, or, equivalently, decreasing the amount of cells per substring.

Figure 1.4a shows a schematic of a partially shaded module. The accompanying IV-curves and maximum power points (MPPs) of the module are provided in Figure 1.4b.

This procedure shows that the power benefits of distributing more ideal[8] BPDs inside a PV module can be intense. Performance benefits up to 110% relative to the 3 BPD-case are shown. However, this example represents an extreme case as both the shading intensity and the degree of shade localization are high. Only yearly simulated conditions are able to yield representative benefits on annual energy performance figures. The modeled module is a 265$W_p$ Yingli Panda. In this example the module temperature is fixed at 40 °C.

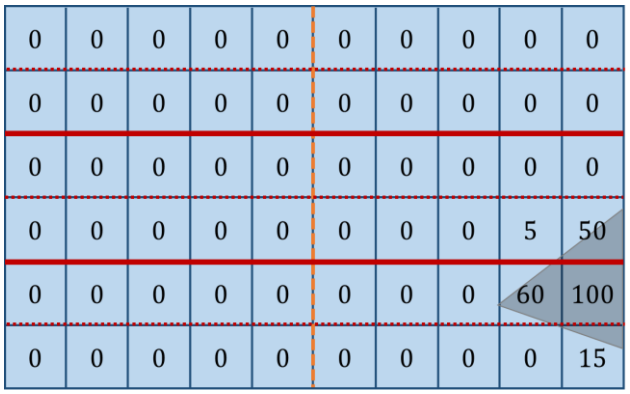


*Figure 1.4a: Partially shaded PV module with shaded cell percentages. The red thick horizontal lines indicate the edges between substrings if 20 cells per substring (3 BPDs) are used. Thin dashed horizontal red lines do so for substrings of 10 cells or 6 BPDs, and the dashed vertical orange line does so for substrings of 5 cells or 12 BPDs in this example.*

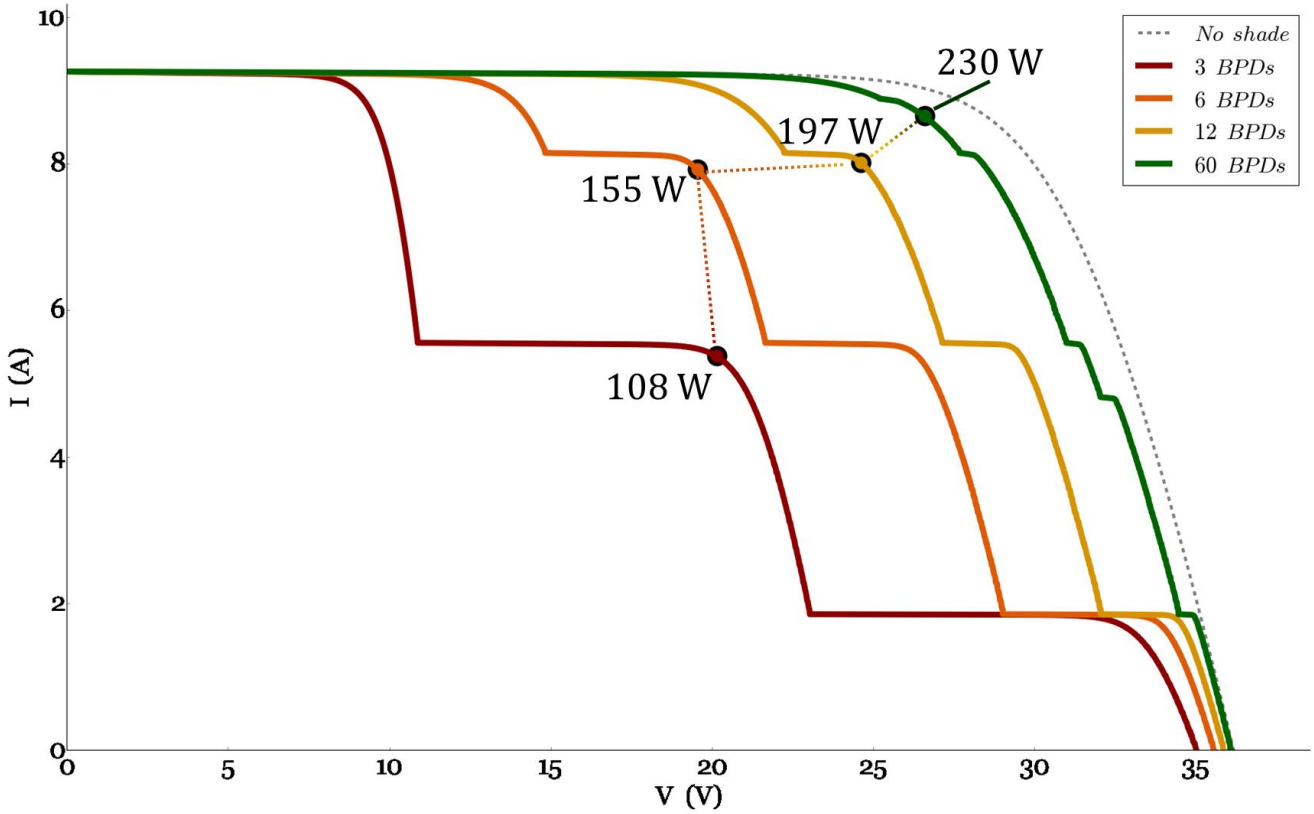


*Figure 1.4b: IV responses of example module under partial shading as in Figure 1.4a. The cases of 3, 6, 12 and 60 per-module BPDs are shown. All increases lead to increases in extractable power, as can be seen from the highlighted MPP-values. The grey dashed line represents the IV curve in unshaded conditions. Total irradiance: 1000 W/m²; diffuse irradiance: 200 W/m²; $T_{module}$: 40 °C.*

[8] Ideal in the sense that the activation of BPDs does not lead to drops in extractable module voltage.

## 1.5 – Research questions & framework

Following up on the line of thought explained in the literature gap (section 1.3.1) and the societal background (§ 1.1), the central research question of this study is as follows:

**What is the effect of increasing the amount of smart by-pass diodes per module on the expected annual energy yield in residential-scale PV systems?**

As noted before, this study serves as a follow-up of the work done by Sinapis et al. (in press). Therefore the studied PV systems are again of string-inverter (SI), power optimizer (PO) and micro-inverter (MI) architecture types. For the same reason the reference number of bypass diodes per module used is three. All three system architectures consist of the same c-Si 265$W_p$ Yingli Panda modules and are landscape-oriented. Each module contains 60 cells.

A selection of 3 (reference), 6, 12 and 30 horizontally aligned BPD substring groups along with 5 and 10 vertically aligned BPD groups and the cell-wise case of 60 BPDs is assumed to be representative. This incremental approach is set out to evaluate the performance effect of stepwise BPD additions. Refer to Figure 1.5a for a visual representation. As this research is set out for exploratory purposes, the BPDs modeled are assumed to be ideal smart by-pass diodes. This means that current leakages are neglected and that no voltage losses are assumed to occur when substrings are bypassed.

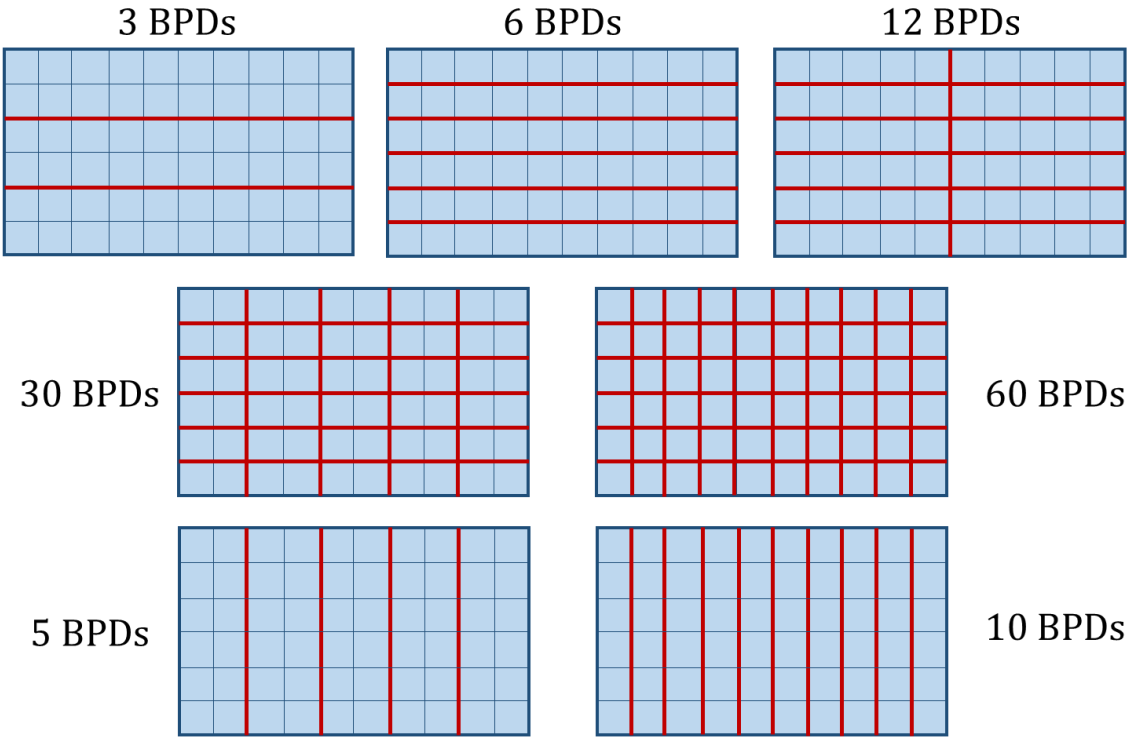


*Figure 1.5a: Substring granularities or variation of per-module BPDs investigated in this research. The 3, 6, 12 and 30 BPD cases are referred to as horizontally aligned substrings; the 5 and 10 BPD cases as vertically aligned substrings. Bypass diodes per cell are assumed in the 60 BPD case.*

A physical-principle-based modeling procedure is chosen in this work. The underlying reason is that this type of model describes PV systems relatively explicitly. Consequently, a thorough assessment of strong and weak spots within the used energy yield model and its individual components is made possible. Another advantage of this type of modeling approach is that it gives a high degree of flexibility in terms of adapting parameters of choice. As a result, conducting a sensitivity analysis becomes a relatively straightforward procedure. Moreover, a similar modeling approach was used by Sinapis et al. (in press) and validated by means of PV system field measurements in Eindhoven, The Netherlands. The energy model used there is generalized to fit the purposes of this research. Consequently, the updated energy model applied in this presented study can straightforwardly be benchmarked with respect to both the formerly created energy model and prior field performance measurements conducted by SEAC (Sinapis, et al., in press). Refer to § 3.8 for more information on this validation procedure.

The partial shading conditions opted for in this research are set to match typical shading objects on a representative "reference" rooftop. More details are outlined in § 3.1. The rooftop reference is determined for The Netherlands because the Dutch documentation on the housing stock is extensive. Furthermore the Dutch average is assumed to be similar to European averages and therefore expected to be representative for residential PV systems. In terms of sensitivity, both the individual and aggregate effects of the shading object types are investigated. As this study is set to explore a realistic high-end range of the by-pass energy recovery potential under partial shading conditions, and by absence of average Dutch dormer dimensions, the shading scenarios are set relatively aggressively in the dormer-incorporating cases.

In terms of roof orientation sensitivity, east and south-eastward alignments on one hand and south-west and westward examples on the other are assumed. The aim here is to provide a complete and representative range sufficient to assess the roof orientation sensitivity generally.

Another part of the sensitivity analysis examines the effect of geographical location on the presented relative energy yield results. On one hand, two cities with low irradiance profiles compared to Eindhoven are chosen: Reykjavik and Oslo. On the other hand, two cities with comparatively high irradiance profiles are considered: Paris and Madrid.

The set-up of this research as outlined in this paragraph leads to the following set of sub-questions:

*1. What are the characteristics of a representative residential (Dutch) PV system and its direct environment?*

*2. What are the effects of the used shading objects on the expected annual DC & AC yield of the studied PV systems and how does the insertion of additional BPDs affect these yield figures?*

*3. Sensitivity: How do roof orientation and geographical characteristics change the absolute and relative DC and system output levels and how does the insertion of additional BPDs affect these yield figures?*

*4. Reflection: What are the strong and weak parts of the updated energy yield model?*

# Chapter 2: Theory

This second chapter outlines the theoretical background that is required for fulfilling the methodological steps (Chapter 3). The principles outlined here follow from prior studies.

The derivation of the general equation for a plane is treated in § 2.1. This is a crucial building block for the in-plane irradiance modeling procedure summarized in § 2.3 and the location of panels and cells (section 3.2.2). § 2.2 provides an explanation of the solar position model used in this study. The solar position model facilitates the translation of the shade modeling procedure (§ 3.2) to a given time and location. The equations required for the IV modeling process (§ 3.5) are listed in § 2.4. This is followed by § 2.5 where the rationale of using lookup tables for various parts of the simulation procedure is explained. Finally, § 2.6 lists the system architecture power conversion steps used in previous work. Refer to Figure 3.a for an overview of all modeling steps and the accompanying direct links with sections of this chapter if applicable.

The BPD application principle shown in § 1.4 could also be placed in this chapter. The underlying reason for including it in the introductory chapter is that the reader is informed about the rationale related to the study topic in a relatively early instance.

## 2.1 – General plane equation

From linear algebra theory, the vector normal to a plane can be determined by the vectoral cross product of two non-parallel planar direction vectors (Boas, 2006). Two in-plane direction vectors are denoted $\vec{V}_{LR}$ and $\vec{V}_{BT}$ here. Their values can be determined if three non-collinear[9] points on the plane are known. In expression form this becomes:

$$\vec{V}_N = \vec{V}_{LR} \times \vec{V}_{BT} \tag{2.1}$$

The normal vector is adjusted to unit length by dividing each normal vector component by the magnitude (length) of the non-unitized normal vector:

$$\hat{\boldsymbol{n}} = \vec{V}_N / |\vec{V}_N| \tag{2.2}$$

Also see Figure 2.1a.

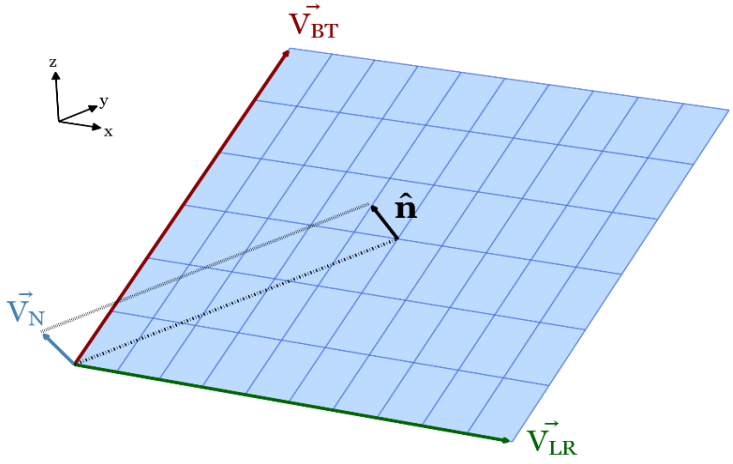


*Figure 2.1a: Normal and unit normal vectors $\vec{V}_N$ and $\hat{\boldsymbol{n}}$ resulting from in-plane direction vectors $\vec{V}_{LR}$ and $\vec{V}_{BT}$. Note: $\vec{V}_N$ is not to scale.*

[9] Non-collinearity means that the three points do not all lie on the same line.

A general form for the equation describing a plane is $ax + by + cz = d$, with $a$, $b$, $c$ and $d$ as constants and $x$, $y$, $z$ as the coordinates in three-dimensional space. From linear algebra theory, the $(x,y,z)$-components of vector $\hat{\boldsymbol{n}}$ are equal to constants $a$, $b$ and $c$ respectively (Boas, 2006).

Using the $(x,y,z)$-coordinates of any in-plane point $P$ and a second general plane equation in the form $a(x - x_P) + b(y - y_P) + c(z - z_P) = 0$ yields the final constant $d$:

$$d = ax_P + by_P + cz_P \tag{2.3}$$

## 2.2 – Solar position model

The solar position in the sky determines the incoming direction of direct irradiance and the relative position of all shading projections at a given time, date and location on Earth. Therefore it is crucial to incorporate a model giving reliable representations of the celestial location of the Sun at any given time step during the TMY.

The solar azimuth angle $\gamma_{azi}$ is measured as the horizontal clockwise deviation angle from north. The solar altitude angle $\gamma_{alt}$ (sometimes referred to as the solar elevation angle) is measured relative to the horizontal plane. At the zenith point perpendicular to Earth's surface, $\gamma_{alt}$ equals 90°. See Figure 2.2a for a graphical illustration of these solar position angles.

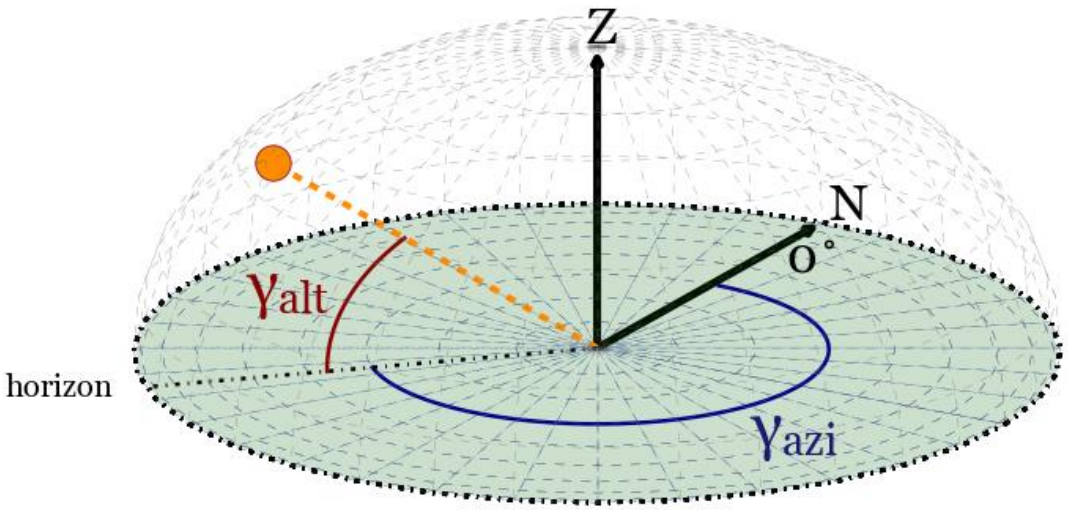


*Figure 2.2a: Definition of solar azimuth ($\gamma_{azi}$) and altitude ($\gamma_{alt}$) angles. N represents the vector pointing due North; Z represents the vector pointing towards the zenith point perpendicular to Earth's surface.*

For any solar altitude $\gamma_{alt}$ and azimuth $\gamma_{azi}$ under the given conventions, the vector pointing from the Sun towards Earth's surface can be described as follows:

$$s_X = -sin(\gamma_{azi})\,cos(\gamma_{alt}) \tag{2.4a}$$
$$s_Y = -cos(\gamma_{azi})\,cos(\gamma_{alt}) \tag{2.4b}$$
$$s_Z = -sin(\gamma_{alt}) \tag{2.4c}$$
$$\vec{V}_{sol} = (s_X, s_Y, s_Z) \tag{2.4d}$$

### 2.2.1 – Yallop method

In earlier similar work (Sinapis, et al., in press; Tzikas, 2015), Yallop's algorithm (Yallop, 1992) was used to determine the position of the Sun at any given time and location. The algorithm is characterized by a high computational speed and a high degree of reliability between the years 1980 and 2050 (Angus & Muneer, 1993).

Table 2.2.1: Yallop's algorithm (Litjens, 2013)

| Step | Parameter | Equation |
|---|---|---|
| 1 | $T_U$ | $Hour + (Minute/60) - T_{z,\,loc}$ |
| 2 | $T_Y$ | $(T_U/24+Day+[30.6\cdot M_{corr}+0.5]+[365.25\cdot(Y_{corr}-1976)]-8707.5)/36525$ |
| 3 | $G_Y$ | $357.528 + 35999.050\cdot T_Y$ |
| 4 | $C_Y$ | $1.915\cdot\sin(G_Y) + 0.020\cdot\sin(2\cdot G_Y)$ |
| 5 | $L_Y$ | $280.460 + 36000.770\cdot T_Y + C_Y$ |
| 6 | $\alpha_{RA}$ | $L_Y - 2.466\cdot\sin(2\cdot L_Y) + 0.053\cdot\sin(4\cdot L_Y)$ |
| 7 | $\varepsilon_{ecl}$ | $23.493 - 0.013\cdot T_Y$ |
| 8 | $\omega_{GHA}$ | $15.0\cdot T_U - 180.0 - C_Y + L_Y - \alpha_{RA}$ |
| 9 | $\delta$ | $\tan^{-1}(\tan(\varepsilon_{ecl}\cdot\sin(\alpha_{RA})))$ |

$M_{corr}$ and $Y_{corr}$ represent corrected year and month values. If the month number exceeds 2 (March or later), $Y_{corr} = Year$ and $M_{corr} = Month-3$. Else $Y_{corr} = Year-1$ and $M_{corr} = Month+9$. Also note that any angular variable calculated above 360° is clipped to 360° as a maximum. This is done by setting it equal to the remainder of the calculated number with respect to 360°.

Now the solar altitude (or elevation) angle can be calculated from Equation 2.5:

$$\gamma_{alt} = sin^{-1}(\sin\varphi_{lat}\cdot\sin\delta - \cos\varphi_{lat}\cdot\cos\delta\cdot\cos(\omega_{GHA}+\lambda_{lon}+180°)) \quad (2.5)$$

Similarly, Equation 2.6 is applied using the convention from Figure 1.3a that the solar azimuth is the clockwise angle between the vector pointing strictly north and the Sun's horizontal position in order to determine the solar azimuth angle:

$$\gamma_{azi} = \cos^{-1}(\cos\varphi_{lat}\cdot\tan\delta\cdot\sin\varphi_{lat}\cdot\cos(\omega_{GHA}+\lambda_{lon}+180°)\cdot\cos\delta/\cos\gamma_{alt}) \quad (2.6)$$

If $(\omega_{GHA} + \lambda_{lon}) < 180°$, the azimuth angle is corrected to 360° minus the result of Equation 2.6.

## 2.3 –In-plane irradiance model

In this paragraph the theory related to determining the effective irradiance $G$ is outlined. This variable is a crucial input required for the IV curve modeling procedure (§ 3.5). Section 2.3.1 lists the reflection losses caused by the glass cover of a PV module. Section 2.3.2 shows the principles of effective irradiance and their implications on the modeling procedure.

### 2.3.1 – Incident angle modifier

The fraction of direct solar irradiance reflected by the glass of a solar module increases if the plane-of-array (POA) solar incidence angle $\theta_{AOI}$ is increased. Consequently the fraction of absorbed direct irradiance decreases at high incidence angles. Models for this phenomenon make use of physical laws from optics. The parameter describing the remaining fraction of absorbed irradiance under a varying solar incidence angle $\theta_{AOI}$ is referred to as the incidence angle modifier (IAM) fraction ($F_{IAM}$).

As is also illustrated in Figure 2.3a, the angle of incidence can be calculated as follows:

$$\theta_{AOI} = cos^{-1}(\hat{\boldsymbol{n}} \cdot -\vec{V}_{sol}) \tag{2.7}$$

Note that $\vec{V}_{sol}$ follows from Equation 2.4 and $\hat{\boldsymbol{n}}$ from Equation 2.2. Both are defined as unit vectors in this study, so no magnitude term for either one of the vectors appears in Equation 2.7.

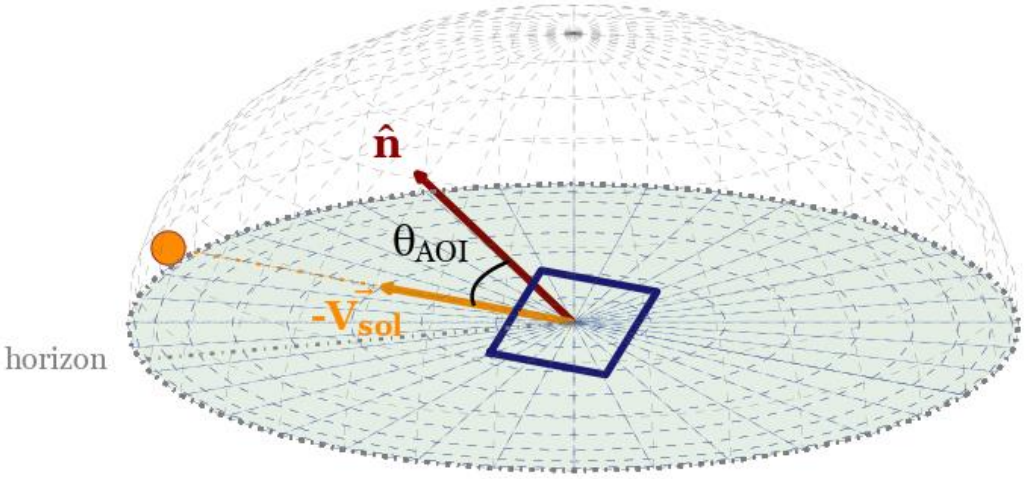


*Figure 2.3a: Derivation of the angle of incidence ($\theta_{AOI}$) as the angle between the Earth-to-Sun-direction (unit) vector $-\vec{V}_{sol}$ and the POA normal direction vector $\hat{\boldsymbol{n}}$.*

The incident angle modifier (IAM) fraction can be determined by use of the ASHRAE model with a reflector parameter $b_0$ of 0.05 (Souka & Safwat, 1966):

$$F_{IAM} = 1 - b_0((1/\cos\theta_{AOI}) - 1) \tag{2.8}$$

Although the ASHRAE model approach is relatively straightforward, irregularities arise at solar incidence angles near 90°. Therefore a physical-approach-based IAM model is used in this study. This approach makes use of a similar yet more accurate model that combines Snell's and Bougher's laws (De Soto, Klein, & Beckman, 2006). This IAM model is also referred to as the physical model (PVPMC/Sandia, 2014b):

$$\theta_{ra} = sin^{-1}(sin\,\theta_{AOI}/i_R) \tag{2.9}$$

$$\tau(\theta_{AOI}) = e^{-KL_g/cos\,\theta_{ra}} \cdot \left[1 - \frac{1}{2}\left(\frac{sin^2(\theta_{ra} - \theta_{AOI})}{sin^2(\theta_{ra} + \theta_{AOI})} + \frac{tan^2(\theta_{ra} - \theta_{AOI})}{tan^2(\theta_{ra} + \theta_{AOI})}\right)\right] \tag{2.10}$$

$$\tau(0) = \lim_{\theta_{AOI}\to 0} \tau(\theta_{AOI}) = e^{-KL_g} \cdot [1 - ((1 - i_R)/(1 + i_R))^2] \tag{2.11}$$

$$F_{IAM} = \tau(\theta_{AOI})/\tau(0) \tag{2.12}$$

In Equations 2.9 to 2.12, the PV glass cover's index of refraction $i_R$ is 1.526, the glazing coefficient $K$ is 4 $m^{-1}$ and the cover glazing thickness $L_g$ is 0.002 m (PVPMC/Sandia, 2014b).

Figure 2.3b below shows the relation between the IAM factor and the solar angle of incidence for the physical IAM model.

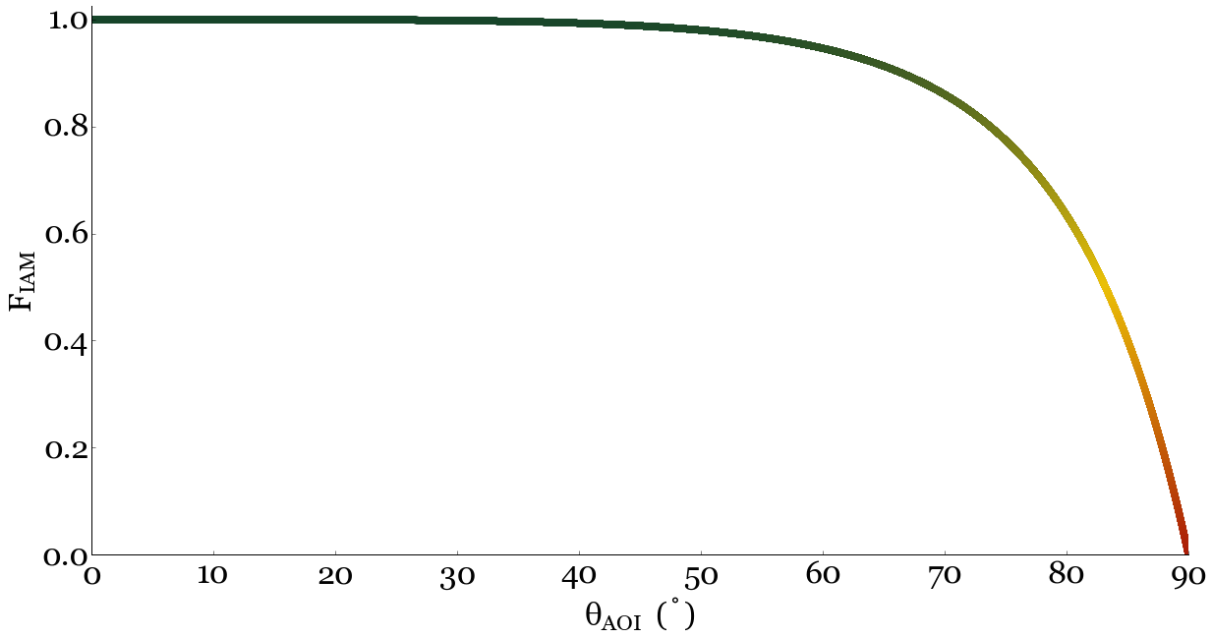


*Figure 2.3b: Relation between incident angle modifier factor ($F_{IAM}$) and the solar angle of incidence ($\theta_{AOI}$).*

### 2.3.2 – Effective in-plane irradiance

The effective in-plane irradiance in unshaded conditions can be expressed as follows (PVPMC/Sandia, 2014a):

$$G_{U,k} = F_{IAM} \cdot G_B \cdot cos\,\theta_{AOI} + G_{diff,k} \quad (2.13)$$

On the contrary, the in-plane shaded irradiance follows from the equation above if no beam irradiance is able to reach the plane:

$$G_{S,k} = F_{IAM} \cdot 0 \cdot cos\,\theta_{AOI} + G_{diff,k} = G_{diff,k} \quad (2.14)$$

Two crucial results for determining the effective irradiance on a substring experiencing partial shading were obtained in prior work (Sinapis, et al., in press; Tzikas, 2015):

**1.** The effective irradiance on a cell can be expressed as the area-weighted accumulation of its unshaded ($G_{U,k}$) and shaded ($G_{diff,k}$) irradiance-receiving fractions (where $\sigma_P$ represents the cell shade percentage):

$$G_{cell,eff} = \left[(100 - \sigma_P) \cdot G_{U,k} + \sigma_P \cdot G_{diff,k}\right] / 100 \quad (2.15)$$

**2.** The effective irradiance on a substring (connecting cells in series) depends on the irradiance received by the cell receiving the least irradiance – the cell shaded most heavily in the case of this study:

$$G = G_{eff} = min\left(G_{cell,eff}\right) = G_{cell,eff}(max(\sigma_P)) \quad (2.16)$$

An illustration of the principle leading to Equation 2.15 is provided in Figure 2.3c. The effective irradiance expressed in Equation 2.16 is used as the irradiance input value $G$ in the PV cell and substring model described in § 3.5.

The cruciality of determining the cell shade percentages in section 3.2.4 directly follows from the principles outlined in the text box containing Equations 2.15 and 2.16.

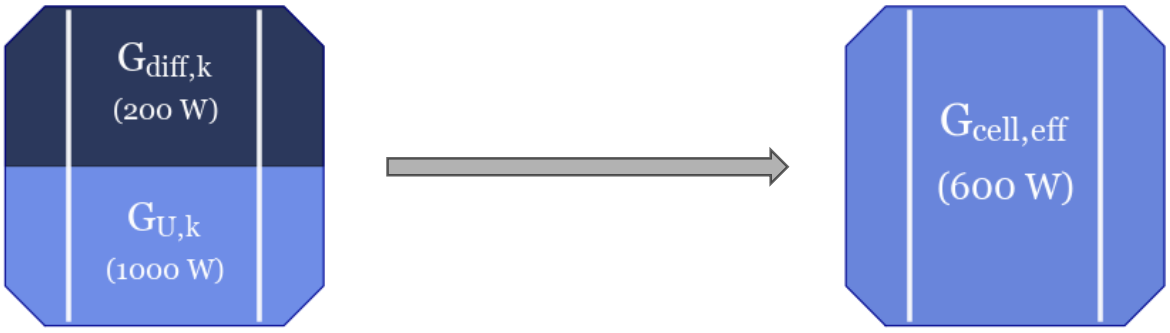


*Figure 2.3c: Principle of deriving the effective cell irradiance from its shaded and unshaded fractions. In this example, $\sigma_P$ = 50%. Modified from previous similar work (Sinapis, et al., in press; Tzikas, 2015).*

## 2.4 – Double-diode cell IV model

In this paragraph the equations for the double-diode model are briefly listed and explained. This background is necessary for the IV curve modeling procedure outlined in § 3.5.

### 2.4.1 – Cell current equations

The following implicit equation describes the final output current of a solar cell under application of the double-diode model:

$$I = I_{ph} - I_{o,1}\left(e^{\frac{V_c+IR_s}{n_1 V_{th}}} - 1\right) - I_{o,2}\left(e^{\frac{V_c+IR_s}{n_2 V_{th}}} - 1\right) - \left(\frac{V_c+IR_s}{R_{sh}}\right) \quad (2.17)$$

In the equation above, the thermal voltage $V_{th}$ is defined as:

$$V_{th} = N_s\, k_B T_c / q_e \quad (2.18)$$

Generally only the parameters $I_{SC,\,STC}$, $V_{OC,\,STC}$, $I_{MPP,\,STC}$, $V_{MPP,\,STC}$, $P_{MPP,\,STC}$ and the temperature coefficients of current, power and voltage ($K_I$, $K_P$ and $K_V$) are provided in PV manufacturers' data sheets (Sinapis, et al., in press). This means that all other required parameters appearing in Equation 2.17 have to be either calculated or approximated.

Firstly, the general photo-generated current ($I_{ph}$) is calculated as a function of irradiance $G$ and cell temperature $T_c$:

$$I_{ph} = (G/G_{STC}) \cdot I_{ph,STC} \cdot (1 + K_I \Delta T) \quad (2.19)$$

In turn, the photo-generated current at STC can be determined by making use of the short-circuit conditions in Equation 2.17. After reworking this gives:

$$I_{ph,STC} = \frac{I_{SC,STC} \cdot (R_s + R_{sh})}{R_{sh}} + I_{o,1}\left(e^{\frac{I_{SC,STC} \cdot R_s}{n_1 V_{th}}} - 1\right) + I_{o,2}\left(e^{\frac{I_{SC,STC} \cdot R_s}{n_2 V_{th}}} - 1\right) \quad (2.20)$$

Now assuming the last two terms to be negligible (Sinapis, et al., in press; Tzikas, 2015):

$$I_{ph,STC} \approx \frac{I_{SC,STC} \cdot (R_s + R_{sh})}{R_{sh}} \quad (2.21)$$

Combining Equations 2.19 and 2.21 gives $I_{ph}$ under various conditions for irradiance and temperature.

Secondly, the saturation current at STC is derived using the open-circuit condition in Equation 2.17. Reworking the obtained expression yields (Carrero, Rodriguez, Ramirez, & Platero, 2010):

$$I_{o,STC} = \frac{(1/R_{sh}) \cdot (I_{SC,STC}(R_s + R_{sh}) - V_{OC,STC})}{\sum_{\alpha=1}^{2} exp\left(V_{OC,STC}/(n_\alpha V_{th})\right)} \quad (2.22)$$

To avoid simulation time resulting from an additional iteration (Jinhui, Zhongdong, Bingbing, & Jun, 2009), to avoid ambiguity on determining $n_1$ and $n_2$ and for the sake of simplicity, it can be assumed that the two diode saturation currents are equal[10]. The general expression for the saturation current can then be written as (Ishaque & Salam, 2011):

$$I_o = I_{o,STC} \cdot (T_c/T_{STC})^3 \cdot exp(q_e/k_B \cdot (E_{g,STC}/T_{STC} - E_g/T_c)) \quad (2.23)$$

[10] In other words: $I_{o,1} = I_{o,2} = I_o$.

In Equation 2.23 the energy band-gap $E_g$ depends on cell temperature $T_c$ as shown in the following empirical relation (Van Zeghbroek, 2011):

$$E_g = E_{g,STC}\left(1 - 0.0002677(T_c - T_{STC})\right) \quad (2.24)$$

### 2.4.2 – Scalability of IV parameters

The equations used in section 2.4.1 particularly consider the case in which the electric response of a single solar cell is modeled.

However, Equations 2.25 to 2.28 can be used to model the electric response of a PV system with $N_p$ cells in parallel and $N_s$ cells in series (Adamo, Attivissimo, Di Nisio, & Spadavecchia, 2011; Tzikas, 2015):

$$I_{sys} = N_p \cdot I_{cell} \quad (2.25)$$

$$V_{sys} = N_s \cdot V_{cell} \quad (2.26)$$

$$R_{s,sys} = (N_s/N_p) \cdot R_s \quad (2.27)$$

$$R_{sh,sys} = (N_s/N_p) \cdot R_{sh} \quad (2.28)$$

Equations 2.25 to 2.28 hold under the assumption of homogeneous irradiance and temperature on the desired scale to consider. Although this approximation does not always hold in real conditions, this simplification only leads to minimal differences from real-life conditions (Sinapis, et al., in press).

Section 2.3.2 mentions that the electrical response of individual substrings of a PV module can be modeled as if they are irradiated homogeneously (also see Figure 2.3c). As a consequence of using the Faiman temperature model described in section 3.4.2, homogeneity over irradiance leads to homogeneity in temperature as explained in § 3.6. As a result the equations listed above can be used to switch the considered scale from the cell level to the substring level (Sinapis, et al., in press; Tzikas, 2015).

## 2.5 – Lookup tables

Lookup tables can be used in intermediate steps of the modeling procedure in order to save computation time for the final TMY simulation. In previous similar work (Tzikas, 2015; Sinapis, et al., in press) this procedure is undertaken after the shade modeling procedure and after the IV curve modeling procedures. This convention is also applied in this study. Refer to Figure 3.a for a complete overview of the modeling procedure used in this work.

## 2.6 – DC-to-AC losses

Various important expressions describing DC-to-AC conversion losses in the PO and MI power electronics used in the MLPM energy yield model (Sinapis, et al., in press; Tzikas, 2015) are listed here. Subsequently they are adopted in this work. As the chosen string inverter system does not align with the SI device used in the MLPM project, it is not included here. Refer to section 3.7.1 for a description of the treatment of power losses in that system architecture.

### 2.6.1 – Power optimizer system losses

The conversion in this system architecture takes place in two steps. First the DC power is collected for each panel and optimized in the power optimizer. In this conversion step the DC output voltage is set to 380 W. Order-two polynomial functions can be used to characterize the conversion losses of a Femtogrid PV300 power optimizer (Sinapis, et al., in press; Tzikas, 2015):

$$P_{loss,PO} = 0.006152 \cdot I_{in}^2 + 0.387 \cdot I_{in} + 0.1828 \quad (@V_{op} = 9.0\ V) \tag{2.29a}$$

$$P_{loss,PO} = 0.0232 \cdot I_{in}^2 + 0.4731 \cdot I_{in} + 0.4279 \quad (@V_{op} = 19.1\ V) \tag{2.29b}$$

$$P_{loss,PO} = 0.09431 \cdot I_{in}^2 + 0.1869 \cdot I_{in} + 0.6701 \quad (@V_{op} = 25.7\ V) \tag{2.29c}$$

$$P_{loss,PO} = 0.1045 \cdot I_{in}^2 + 0.1628 \cdot I_{in} + 0.7506 \quad (@V_{op} = 28.0\ V) \tag{2.29d}$$

$$P_{loss,PO} = 0.1261 \cdot I_{in}^2 - 0.04426 \cdot I_{in} + 1.594 \quad (@V_{op} = 29.6\ V) \tag{2.29e}$$

In Equations 2.29a to 2.29e, $I_{in}$ represents the input current, $P_{loss}$ the power losses in the PO and $V_{oc}$ the operating voltage values for which the polynomial power loss function was determined.

After the DC-DC conversion step for each module, a central inverter transforms the aggregated power branches to grid-compatible AC power at 230 V. For the power losses of a Femtogrid Kratos Inverter 2400 the corresponding best-fit equation is (Sinapis, et al., in press; Tzikas, 2015):

$$P_{loss} = -0.2255 \cdot I_{in}^2 + 10.48 \cdot I_{in} + 14.31 \tag{2.30}$$

### 2.6.2 – Micro-inverter system losses

In this system architecture the DC power is collected per panel, but now direct conversion towards AC power at 230 V takes place. For a Heliox SMI300 micro-inverter the conversion power losses can be expressed as follows (Sinapis, et al., in press; Tzikas, 2015):

$$P_{loss,MI} = 0.007729 \cdot I_{in}^2 + 1.038 \cdot I_{in} + 0.2514 \quad (@V_{op} = 16.6\ V) \tag{2.31a}$$

$$P_{loss,MI} = 0.06141 \cdot I_{in}^2 + 0.7701 \cdot I_{in} + 2.071 \quad (@V_{op} = 26.5\ V) \tag{2.31b}$$

$$P_{loss,MI} = 0.06441 \cdot I_{in}^2 + 0.8066 \cdot I_{in} + 2.103 \quad (@V_{op} = 27.8\ V) \tag{2.31c}$$

$$P_{loss,MI} = 0.06139 \cdot I_{in}^2 + 0.8753 \cdot I_{in} + 2.145 \quad (@V_{op} = 28.8\ V) \tag{2.31d}$$

$$P_{loss,MI} = 0.059 \cdot I_{in}^2 - 0.8869 \cdot I_{in} + 2.686 \quad (@V_{op} = 30.4\ V) \tag{2.31e}$$

In Equations 2.31a to 2.31e, $I_{in}$ represents the input current, $P_{loss}$ the power losses in the MI and $V_{oc}$ the operating voltage for which the respective polynomial power loss expression is constructed.

# Chapter 3: Methodology

This chapter explains the treatment of the energy yield modeling procedure in detail. The main contrast with the Theory chapter is that the focus lies on the approach of the present research instead of on prior fundamental findings. § 3.1 describes how the built environment of interest is created in SketchUp. The coordinates of all relevant modules and objects are transferred to a Python script. There the shade projections for any solar location in the sky are determined. § 3.2 explains this procedure. § 3.3 lists the geographical characteristics of the locations chosen in the simulation. Subsequently the procedure for determining the effective irradiance and temperature for each substring is elaborated on in § 3.4. These serve as required input for the modeling the electrical response of the substring as outlined in § 3.5. § 3.6 and § 3.7 explain the methodology regarding the determination of DC and AC outputs. Finally, § 3.8 outlines the method of the undertaken validation procedure and § 3.9 introduces the performance indicators used for the analysis in the Results chapter. Apart from the SketchUp procedure, Python is the used simulation environment throughout the methodology. However, the principles explained in this work are also applicable to other simulation environments.

Figure 3.a below shows a flowchart of the entire energy yield modeling procedure for a single time step within the typical meteorological year (TMY). This also illustrates how the explained theoretical and methodological principles build upon each other.

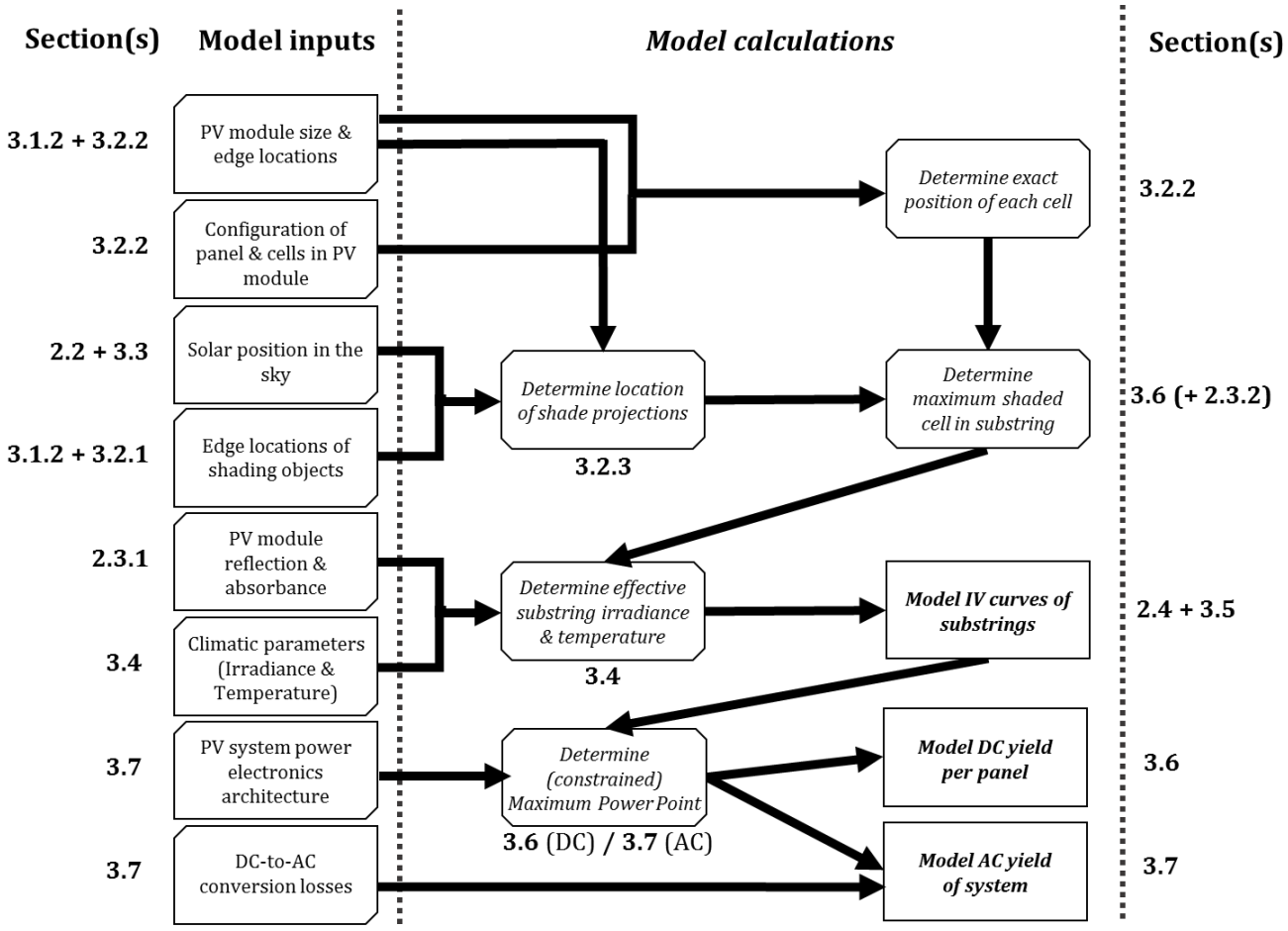


*Figure 3.a: Flowchart of the complete modeling procedure for each TMY time step. Also noted are the sections in which individual modeling steps are further explained. Modified from previous similar work* ***(Sinapis, et al., in press).***

## 3.1 – SketchUp model

As briefly touched upon in the text explaining the outline of this Methodology chapter, a SketchUp representation of the modeled environment is constructed as a first step. This is done in order to determine the location of the edge points of all objects of interest in 3D space on one hand and for visualization purposes on the other.

Besides providing the input required for the shade model, the SketchUp model has also been used to successfully benchmark the accuracy of the shadow model. Intermediary comparisons between the cell shade percentage distribution throughout the field and the SketchUp shade projection tool for selected times of day in various times of year have been conducted to do so.

Section 3.1.1 treats the derivation of properties for the reference house and house row in detail. Section 3.1.2 outlines the distribution of panels and shading objects throughout the modeled house row representation.

Visual representations of the modeled field setup are shown in Figures 3.1a and 3.1b.

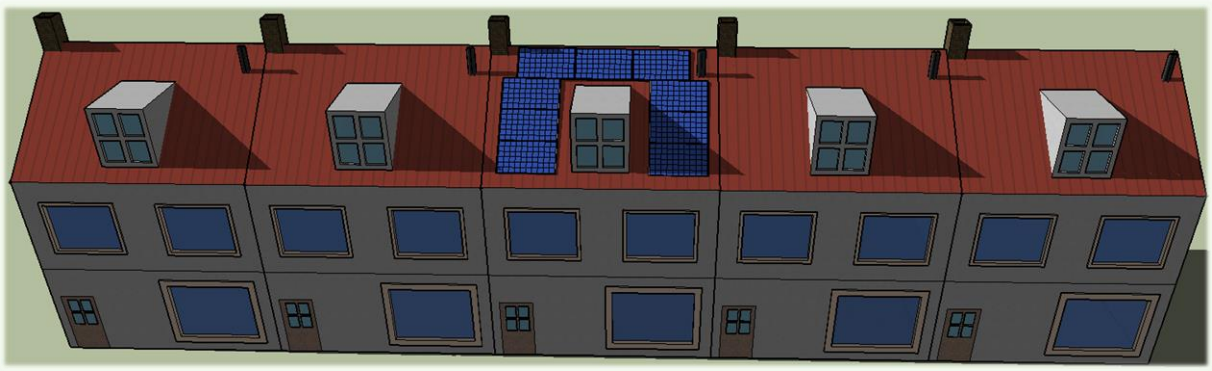

*Figure 3.1a: SketchUp representation of the modeled house row, the present shading objects (exhaust pipes, chimneys, dormers) and nine PV modules on the most central house roof.*

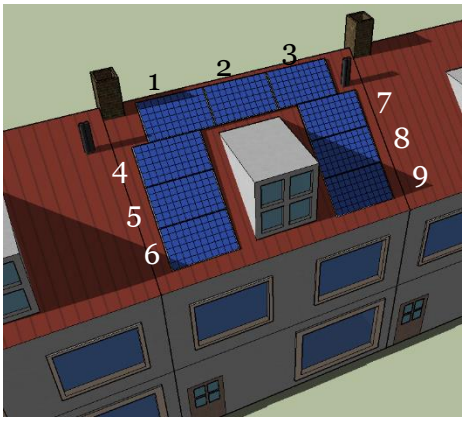


*Figure 3.1b: SketchUp representation of the most central house roof and corresponding panel numbers used for the PV system(s).*

### 3.1.1 – Reference house dimensions

As the vast majority of Dutch houses comprises terraced houses (Senter Novem & VROM, 2007), this is the reference house type chosen in this study. In order to investigate the maximum potential of module-level power granularity management on an average Dutch house with an average tilt angle and optimal south-facing orientation, an aggressive shading scenario has been chosen. For the same reason the studied PV system is set up on the roof of the most centrally located house.

In general a row of terraced houses may consist of three up to dozens of houses. Choosing three or four houses in a row most likely leads to a houses-per-row estimate that is too low. On the other hand, choosing any more houses in the row would have a negligible effect on the annual PV system yield of one of the central houses. This is due to their great distance to the studied PV system and the high degrees of casted shading overlap with regard to shading obstacles already present on neighboring houses in the modeled house row.

A saddle roof with a total surface of 60.0 $m^2$, an along-the-roof distance of 4.5 m, a ground floor area of 45.9 $m^2$ and a house width of 6.6 m are taken (Verberne, 2014). This fits a reference terraced house built between 1966 and 1975 (Senter Novem & VROM, 2007). That building period represents the largest terraced housing stock group in The Netherlands and nearly 10% of all houses on a national level (Senter Novem & VROM, 2007).

As other dimensional values are not found in the aforementioned references, the depth of the house was determined using the house width and the ground floor area. This leads to a rounded house depth of 6.9 m. On top of that, the height of the two storeys is based on the vertical dimensions of a reference post-2013 built terraced house: 2.86 m each (Agentschap NL, 2013). Combining the half-length of the house depth value with the cross-sectional rooftop distance gives a rounded rooftop tilt angle of 40°. When adding the storey heights as well, a rooftop height of 8.61 m can be defined.

Within the SketchUp test field the left-bottom point of the righter-most terraced house in the row lies on the origin. Note that *x* and *y* represent the eastward and northward directions throughout this work unless stated otherwise. This matches the convention used in SketchUp. Coordinate parameter *z* indicates the height above ground surface level.

Assumed is that other house rows are located too far from the studied house row. The reasons underlying the fairness of this assumption are threefold:

1) The studied roof faces strictly south;
2) The solar altitude in the southern sky parts in The Netherlands never falls below 10° to 15°;
3) The distance between house rows is generally more than 10 m due to gardens and/or streets generally marking the separation zone between different house rows.

### 3.1.2 – Roof accessories' properties

Note that each house roof in the house row of five has the same accessories except for the panels. As mentioned in section 3.1.1, the modules are set up only on the most central house roof. Also see Figures 3.1a and 3.1b. Consult Annex A for an example of the used coordinates of roof accessories on top of the middle house.

*Exhaust pipes*
Given that a relatively aggressive shading scenario is used in this study (as explained in section 3.1.1), two exhaust pipes will be set up on each house roof and are located directly next to each other. The typical height of exhaust pipes lies in the range of 0.4 to 1.2 m (Sinapis, Litjens, & Van den Donker, 2014). This gives an average estimate of 0.8 m. However, the average height of the exhaust pipes above the house roof surfaces is rounded to 0.75 m. This takes the height increase of the roof (as it is tilted 40°) with respect to the foot of the exhaust pipe into account. The diameter of each pipe is assumed to be 0.11 m (Ubbink, 2016). In terms of location, a scan of Dutch terraced house rooftop examples shows that exhaust pipes are generally set up slightly below the roof ridge. Consequently, a central location 1.0 m below the roof ridge and 0.5 m left from the rightmost roof ridge point on each house is chosen. The rightmost and leftmost edges of the two exhaust pipes on each house roof both touch this central location point.

*Chimneys*
Shown in an information leaflet on prefab chimneys (Muelink & Grol and Burgerhout, 2007) is that the available side lengths of chimneys with squared bases for tilted roofs lie in the range 0.28 m to 0.88 m. Combined with an estimation of chimney diameters on example roofs in the same document, a "best estimate" chimneys' side length of 0.5 m is derived. A representative estimate of the height of the chimneys is determined using the average of typical heating exhaust pipes typically used to discharge air or flue gases. This gives an average height estimate of 0.8 m measured relative to the roof ridge. As regulations cause chimneys to be located at the highest part of the roof in general (Sinapis, Litjens, & Van den Donker, 2014), the leftmost central location on the roof ridge is chosen here.

*Dormers*
The location and dimensions of Dutch dormers without requirement of a building permit are constrained by regulations (Dutch Ministry of Home Affairs, 2015). Taking into account the use of an aggressive shading scenario, the dormer height is set at the maximum allowed height of 1.75 m based on these regulations. The foot of each dormer is located 1.0 m above the roof bottom and is measured along the roof. Besides, the dormer width[11] chosen is 1.6 m. All dormers are located centrally on each house roof.

*Panels*
Nine Yingli Panda 265 $W_p$ PV modules are set up in landscape orientation on the central terraced house roof and numbered 1 to 9 respectively (Figure 3.1b):

- Three modules 0.17 m along-roof above the dormer, maximally centralized on the roof
- Three modules with rightmost edges 0.47 m left of dormer; lowermost bottom space 0.43 m
- Three modules with leftmost edges 0.57 m right of dormer; lowermost bottom space 0.43 m

Module dimensions are taken from a SketchUp model used in previous similar work (Sinapis, et al., in press): a length of 1.66m and a height of 0.99 m. Individual cells within these modules are plotted as 0.16 m x 0.16 m squares.

[11] In terms of shading, only the dormer's height and the panel-to-dormer distance affect the shade pattern casted on the panels by the dormer. The dormer width only influences the remaining roof space for solar panels.

## 3.2 – Shadow model

Edge point coordinates of all shading objects located on each house roof in the modeled row of terraced houses (§ 3.1) are translated to cell shade percentages by means of the shadow model presented here. This requires knowledge of the solar position at a given time (§ 2.2). The importance of calculating the cell shade percentages is stressed in section 2.3.2.

Five shading scenarios are used to unravel the effect of individual shading object types on TMY energy yield figures: 1) all shading objects present; 2) only dormers present; 3) only exhaust pipes present; 4) only chimneys present; and 5) an unshaded scenario without any shading objects on the house row roofs.

The cell shade percentages for all 540 (= 60 cells times 9 panels) cells in the field are stored in lookup tables for all solar positions in the sky with a resolution of 0.5° for both azimuth ($\gamma_{azi}$) and altitude ($\gamma_{alt}$). This means that a representation for the shading conditions in the test field is determined for roughly every two minutes (= 1440/ (360°/0.5°)).

The geometrical representation of shading objects, panels and the determination of individual cell locations are discussed in the first sections of this paragraph. Subsequently the derivation of shade projection locations and cell shade percentages are presented each.

### 3.2.1 – Shading objects representation

The chimneys and dormers are represented as cuboids in the shading model. The eight edge points are numbered in a fixed order. Left-bottom, right-bottom, right-top and left-top (LB, RB, RT and LT) points on the bottom surface are marked as points 1, 2, 3 and 4 respectively. The same sequence holds for the points numbered 5 to 8 on the top surface. See Figure 3.2a.

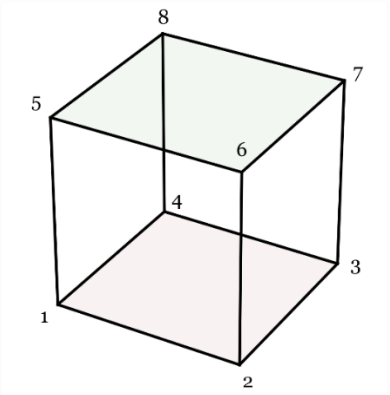


*Figure 3.2a: Example of a cuboid containing the used edge point numbering convention.*

Exhaust pipes are modeled as icosagonal prisms (20 base points) as illustrated in Figure 3.2b. The bottom and top surface center points of the pipes are shot from SketchUp by means of a PointCloud tool. Subsequently the prism edge point coordinates ($x_{p,n}$, $y_{p,n}$) are determined using Equations 3.1 and 3.2:

$$x_{p,n} = x_c + \frac{D}{2}\cos((n-1)\theta_R) \quad (3.1)$$

$$y_{p,n} = y_c + \frac{D}{2}\cos((n-1)\theta_R) \quad (3.2)$$

Note that $\theta_R = \frac{2\pi}{20}$ rad and that $D$ is 0.11 m (from section 3.1.2).

The $z$-coordinates of the bottom and top edge points are considered equal to those of the central points $z_{BC}$ and $z_{TC}$ respectively.

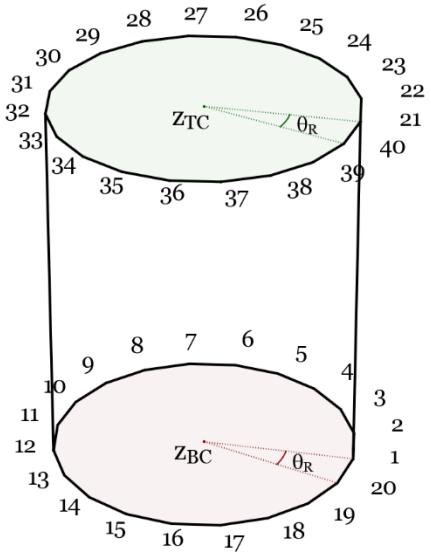


*Figure 3.2b: Icosagonal prism containing the used edge point numbering convention.*

### 3.2.2 – Location of panels and cells

The characteristic (*x*,*y*,*z*)-coordinates of each modeled PV panel are the edge points shot from the SketchUp field in LB, RB, RT and LT order (section 3.1.2). Subsequently the cell edge points are determined by line-segmenting the left-right and bottom-top directions in the panel and then adding up the appropriate line segment pieces to obtain any cell edge coordinate within the panel.

On top of that, cells are allocated cell numbers relating to their position within the panel. Also see Figure 3.2c. The left case shows the cell number distribution given horizontal cell alignment; the right case if the cell alignment is vertical. Cells are connected based on ascending cell numbers.

Refer to Annex B for a detailed mathematical derivation of the cell locations and cell numbering.

| | | | | | | | | | |
|---|---|---|---|---|---|---|---|---|---|
| 60 | 59 | 58 | 57 | 56 | 55 | 54 | 53 | 52 | 51 |
| 41 | 42 | 43 | 44 | 45 | 46 | 47 | 48 | 49 | 50 |
| 40 | 39 | 38 | 37 | 36 | 35 | 34 | 33 | 32 | 31 |
| 21 | 22 | 23 | 24 | 25 | 26 | 27 | 28 | 29 | 30 |
| 20 | 19 | 18 | 17 | 16 | 15 | 14 | 13 | 12 | 11 |
| 1 | 2 | 3 | 4 | 5 | 6 | 7 | 8 | 9 | 10 |

| | | | | | | | | | |
|---|---|---|---|---|---|---|---|---|---|
| 6 | 7 | 18 | 19 | 30 | 31 | 42 | 43 | 54 | 55 |
| 5 | 8 | 17 | 20 | 29 | 32 | 41 | 44 | 53 | 56 |
| 4 | 9 | 16 | 21 | 28 | 33 | 40 | 45 | 52 | 57 |
| 3 | 10 | 15 | 22 | 27 | 34 | 39 | 46 | 51 | 58 |
| 2 | 11 | 14 | 23 | 26 | 35 | 38 | 47 | 50 | 59 |
| 1 | 12 | 13 | 24 | 25 | 36 | 37 | 48 | 49 | 60 |

*Figure 3.2c: Cell numbering for a 60-cell panel in the case of horizontal cell alignment and vertical cell alignment (left and right respectively). On the left, red lines indicate substring separation if 3 substring groups (BPDs) per module are assumed. On the right, red lines indicate substring separation for 5 substring groups of 12 cells each.*

### 3.2.3 – Shade projection

To allow partial shading conditions, the angle between vector $\vec{V}_{sol}$ (§ 2.2) and the normal of the plane described by the equation $ax + by + cz = d$ (§ 2.1) has to be greater than 90 degrees[12]. In these cases the shade projection of a shade object's edge point on a lower-lying plane follows from extending the shade object's edge point coordinate along vector $\vec{V}_{sol}$ until a point on the plane is found. In equation form this can be expressed as a line parameterization (Boas, 2006):

$$(x_A, y_A, z_A) + t\vec{V}_{sol} = (x_A, y_A, z_A) + t(s_X, s_Y, s_Z) \qquad (3.3)$$

In Equation 3.3, $A$ denotes the shade object's edge point coordinate and $A + t\vec{V}_{sol}$ the accompanying shadow projection point on the panel plane. Therefore the general (*x*,*y*,*z*)-coordinates lying on this line can be described as follows:

$$(x, y, z) = (x_A, y_A, z_A) + t(s_X, s_Y, s_Z) = ((x_A + ts_X), (y_A + ts_Y), (z_A + ts_Z)) \qquad (3.4a)$$

For any shadow edge point $n$, the specific equation for the intersection point $\xi_n$ becomes:

$$(x_{\xi_n}, y_{\xi_n}, z_{\xi_n}) = (x_n, y_n, z_n) + t_n(s_X, s_Y, s_Z) = ((x_n + t_n s_X), (y_n + t_n s_Y), (z_n + t_n s_Z)) \qquad (3.4b)$$

[12] An angle between $\vec{V}_{sol}$ and the collecting plane of less than 90° is required to have direct irradiance incoming and the possibility of partial shading conditions. This implies a required angle between $\vec{V}_{sol}$ and the plane normal of more than 90° because the collecting plane is anti-parallel to the panel plane normal vector (Figure 2.3a).

As the intersection point $\xi_n$ lies on the plane $ax + by + cz = d$, the following holds as well:

$$d = a(x_{\xi_n}) + b(y_{\xi_n}) + c(z_{\xi_n}) = a(x_n + t_n s_X) + b(y_n + t_n s_Y) + c(z_n + t_n s_Z) \quad (3.5)$$

Rewriting equation 3.5 gives the resulting expression for line parameterization constant $t_n$:

$$t_n = \frac{d - (ax_n + by_n + cz_n)}{as_X + bs_Y + cs_Z} \quad (3.6)$$

Refer to Figure 3.2d for a visual interpretation of the line parameterization procedure.

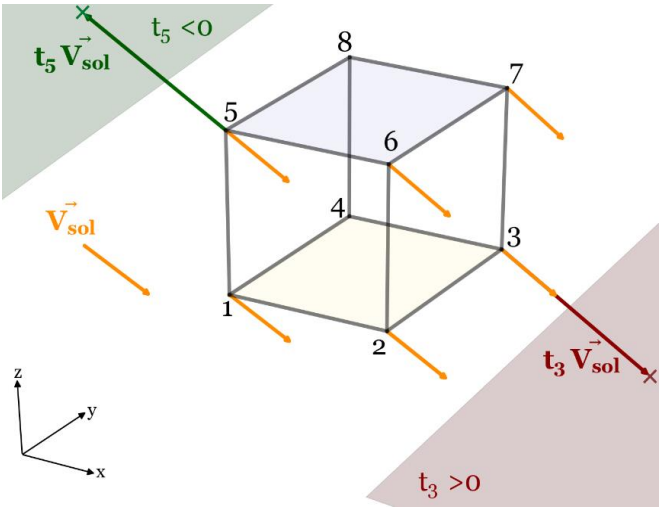


*Figure 3.2d: Two planes and two examples of resulting intersection points $\xi_n$. One plane is located above the top surface (points 5,6,7,8) of the cuboid shading object, the other below the bottom surface (points 1,2,3,4). If a ray coming from the Sun (direction $\vec{V}_{sol}$) is blocked by a shading object's edge point ($t_n > 0$), it leaves a shade projection on the lower-lying plane. Reversely, no shade intersection points exist if the ray hits the plane before reaching the shading object ($t_n < 0$).*

It follows from Figure 3.2d that only a positive value for $t_n$ refers to point $n$ shading the panel plane in point $\xi_n$. This means that $t_n$ can be used to assess whether a shading object's edge point $n$ shades a panel plane, and if so, where on the plane the projection falls (point $\xi_n$).

If a panel plane is located completely below all edge points of a shading object (thus, if $t_n > 0$ for all shading object's edge points), the collection of individual intersection points $\xi_n$ suffices for evaluating the shade polygon casted on the plane. This shadow polygon is then fully described by connecting all outward intersection points linearly. See Annex D or a detailed explanation of this procedure. Inversely, the panel is not shaded by the shading object at all if $t_n < 0$ for all $n$ of a shading object.

However, intersections $\xi_p$ on the ribs of a shade object may exist if some of the shading object's edge points cast a shade projection on a panel plane whereas others do not (some $t_n$ positive, some negative). In this case subsequent line parameterization procedures along the vertical, horizontal counterclockwise and horizontal clockwise rib directions relative to point $n$ are executed to find any existing intersection points $\xi_p$ on the shade object's ribs. Finally the most outward points define the edges of the shade polygon casted on the plane by the shade object (Annex D). Annex C provides a detailed technical explanation related to finding intersection points $\xi_p$.

### 3.2.4 – Cell shade percentages

The two-dimensional shadow projection on a panel plane given a three-dimensional shading object of a particular shape is derived following the methodology outlined in the previous section. The amount of 10 x 10 evenly spaced points within each cell lying within at least one of the casted shade projections reflects the shade percentage of that specific cell. This principle is used to calculate cell shade percentages throughout the field. Refer to Annex E for a general algorithmic example.

In order to match the exact solar position to the 0.5° resolution in terms of solar azimuth ($\gamma_{azi}$) and altitude ($\gamma_{alt}$) used in the cell shade percentage lookup tables, the azimuth at any given time is rounded to the closest 0.5°-resolution value found in the lookup tables. Linear interpolation is used to calculate the cell shade percentage for any solar altitude angle to level out resolution differences between summer (high daily variation in $\gamma_{alt}$) and winter (low daily variation in $\gamma_{alt}$):

$$\sigma_P(\gamma_{alt}) = \sigma_P(\gamma_{alt,lo}) + (\gamma_{alt} - \gamma_{alt,lo})/(\gamma_{alt,hi} - \gamma_{alt,lo}) \cdot (\sigma_P(\gamma_{alt,hi}) - \sigma_P(\gamma_{alt,lo})) \qquad (3.7)$$

### 3.2.5 – Time-saving steps

Two measures are taken to prevent unnecessary calculations in the most time-consuming step in the shade modeling procedure. This step comprises of assessing whether each specific example of the 10 x 10 points in each cell lies within at least one of the shade projection polygons or not. This reduces the required simulation time[13]:

1. The field is always fully shaded if the angle $\theta_{AOI}$ between the solar vector and the receiving plane direction (also see section 2.3.1) is 90° or more. Cell shade percentages of 100% throughout the field are directly returned in these cases.

2. If a shade polygon either fully lies above, below, left or right of a panel, it does not shade any cell within the panel. In these cases, continue to the next shading object's shade polygon.

[13] Mathematically stating time-saving step 2: if $x_{min}$ or $y_{min}$ of the shade polygon is greater than $x_{max}$ or $y_{max}$ of the considered panel respectively; or inversely if $x_{max}$ or $y_{max}$ of the polygon is less than $x_{min}$ or $y_{min}$ of the panel.

## 3.3 – Geographical location parameters

Table 3.3.1 shows the geographical characteristics used for the various simulated TMY locations. HTC Eindhoven is the reference location. Note that these geographical parameters are used as input for both the climatic TMY data (section 3.4.1) and the solar position model (section 2.2).

Table 3.3.1: TMY simulation locations' longitude, latitude and elevation level

| Location | Parameter | Value |
|---|---|---|
| Eindhoven (HTC) | | |
| | $\varphi_{lat}$ | 51.41° N |
| | $\lambda_{lon}$ | 5.45° E |
| | $E_L$ | 30 m |
| Reykjavik | | |
| | $\varphi_{lat}$ | 64.2° N |
| | $\lambda_{lon}$ | 22.0° W |
| | $E_L$ | 0 m |
| Oslo | | |
| | $\varphi_{lat}$ | 59.9° N |
| | $\lambda_{lon}$ | 10.7° E |
| | $E_L$ | 27 m |
| Paris | | |
| | $\varphi_{lat}$ | 48.9° N |
| | $\lambda_{lon}$ | 2.4° E |
| | $E_L$ | 38 m |
| Madrid | | |
| | $\varphi_{lat}$ | 40.4° N |
| | $\lambda_{lon}$ | 3.7° W |
| | $E_L$ | 662 m |

## 3.4 – Effective irradiance & temperature

The in-plane irradiance components required for calculating the effective irradiance $G$ (section 2.3.2) originate from a Meteonorm climate data set. The input settings for generating the used data set are listed in section 3.4.1. Besides the (effective) irradiance introduced in section 2.3.2, (effective) temperature is the second major input for the IV cell and substring model discussed in § 2.4 and § 3.5. The calculation recipe for the substring temperature is presented in section 3.4.2. The parameters required for this procedure also follow from the data set generated in Meteonorm as described in section 3.4.1.

### 3.4.1 – Meteonorm climate data

Meteonorm 7.0 is used to generate climate data (irradiance components, temperature and wind speed) on an hourly basis for the TMY simulations. Table 3.4.1 shows the input parameters used in the referenced software.

For the underlying irradiance separation and in-plane radiation model methodology and equations used in the models picked, refer to the Meteonorm background document (Meteonorm, 2015). This also holds for a general overview of stochastic generation of TMY data.

Table 3.4.1: Meteonorm input settings for TMY data generation

| **Parameter/procedure** | **Meteonorm input** |
|---|---|
| $\varphi_{lat}$ | 51.4° N (HTC example; other locations: §3.3) |
| $\lambda_{lon}$ | 5.5° E (HTC example; other locations: §3.3) |
| Elevation level ($E_L$) | 30 m (HTC example; other locations: §3.3) |
| Albedo factor ($\rho_A$) | 0.15 |
| POA azimuth ($\kappa_{azi}$) | 180° (= 0° in Meteonorm)[14] |
| POA tilt angle ($\kappa_T$) | 40° |
| Irradiance data period | 1991-2010 |
| Ambient temperature data period | 2000-2009 |
| Irradiance separation model | Perez model |
| Tilt (in-plane) radiation model | Perez model |
| TMY data time interval | Hourly |
| Output columns | $G_{GHI,h}$, $G_{G,k}$, $G_{diff,k}$, $G_B$, $T_a$, $W_{FF}$ |

All input parameters not mentioned here match the standard data generation settings in the Meteonorm software package.

In order to match the resolution of the TMY data with the time resolution of the shading look-up tables, all hourly climatic data values are linearly interpolated to 5-minute time steps throughout all TMY simulations.

[14] This parameter is changed to values corresponding to E, SE, SW and W orientations in the orientation sensitivity simulations.

### 3.4.2 – Temperature model

The temperature model used to derive substring temperature in this research is developed by Faiman (Faiman, 2008). It is also used in similar prior work (Sinapis, et al., in press). In general this model is said to be more accurate than the widely used NOCT model (Tzikas, 2015).

The resulting equation for the Faiman temperature model is as follows (Faiman, 2008):

$$T = T_s = T_a + G_{eff}/(U_0 + U_1 W_{FF}) \quad (3.8)$$

The values used for $U_0$ and $U_1$ are 25.0 W/(m²K) and 6.84 W/(m³sK) (Faiman, 2008). The result of Equation 3.8 is used as the temperature input for the PV cell and substring models (§ 2.4 & § 3.5).

Figure 3.4a shows temperature augmentation $\Delta T$ relative to ambient temperature for ranges of irradiance and (average) wind speed encountered in and derived from Meteonorm TMY data.

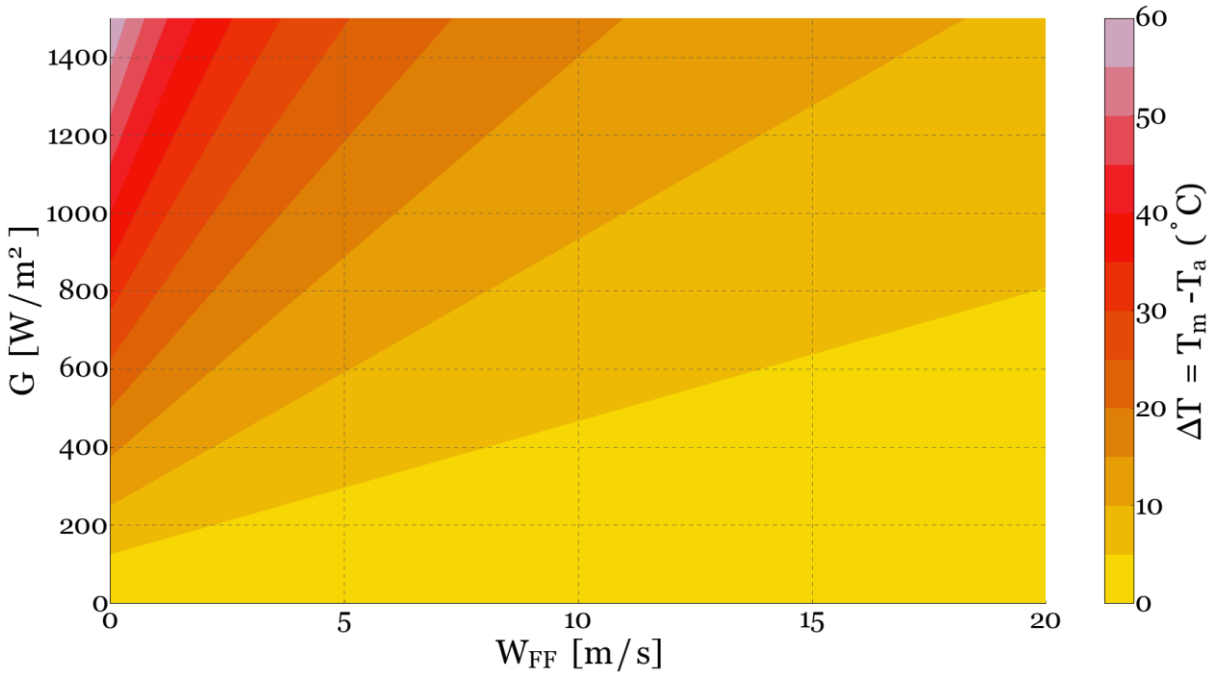


*Figure 3.4a: Module temperature augmentation ΔT relative to ambient temperature for irradiance values in the range G = 0 – 1500 W/m² and average wind speed values in the range $W_{FF}$ = 0 – 20 m/s.*

## 3.5 – PV cell & substring model

The double-diode cell model is used to model the electric response of each substring in the studied PV system architectures due to its relatively high accuracy at lower irradiance compared to the simpler single-diode PV cell model (Lun, Wang, Yang, & Guo, 2015). Various other PV cell modeling approaches are reported in literature (Jena & Ramana, 2015; Cotfas, Cotfas, & Kaplanis, 2013). However, these have a relatively emerging nature and are not widely used currently.

As mentioned in the research framework (§1.5), the amounts of series-connected cells per substring considered in this study are 20, 10, 5 and 2 given horizontal cell alignment inside the substring (Figure 3.2c). This is equivalent to 3, 6, 12 and 30 BPDs inside the module (Figure 1.5a). The considered substring sizes are 12 and 6 respectively for vertical cell alignment (Figure 3.2c, right and Figure 1.5a). The last case is 1 cell per substring, equivalent to 60 BPDs inside the module (Figure 1.5a).

As for the shade modeling procedure, lookup tables are used to save simulation time later on (§2.5). The lookup table creation is conducted by combining all steps described in sections 2.5.1 to 2.5.5 for all pairs of irradiance and substring temperature in the ranges from 1 W/m² to 1500 W/m² and from -20 °C to 100 °C. The resolutions used for irradiance and temperature in the lookup tables are 1 W/m² and 1 °C respectively.

Table 3.5.1: PV cell & substring model input values @ STC in this study

| **Parameter** | **Model input value** |
|---|---|
| Module short-circuit current ($I_{SC}$) | 9.2 A |
| Module open-current voltage ($V_{OC}$) | 38.14 V |
| Module MPP current ($I_{MPP}$) @ STC | 8.8 A |
| Module MPP voltage ($V_{MPP}$) @ STC | 29.88 V |
| Module MPP ($P_{MPP}$)* @ STC | 263.0 W |
| Cells in parallel per module ($N_p$) | 1 |
| Cells in series per module ($N_s$) | 60 |
| Ideality factor diode 1 ($n_1$) | 1 |
| Ideality factor diode 2 ($n_2$) | 2 |
| Panel series resistance ($R_s$) | 0.365 Ω (determined in 3.5.2) |
| Panel shunt resistance ($R_{sh}$) | 623.84 Ω · $G_{STC}/G_{eff}$ (determined in 3.5.2) |

*: Average of Yingli Panda 265$W_p$ flash data module power performance as performed by ECN prior to the MLPM project. This value is chosen to represent the real performance conditions slightly better than the nominal value of 265 $W_p$.

### 3.5.1 – Diode ideality factors

In order to further simplify the computational procedure required for determining the output current of a cell given the double-diode model, the diode ideality factors are assumed to be $n_1 = 1$ and $n_2 = 2$ respectively. These values are chosen such that the two modeled diodes in the cell approximate Shockley-Read-Hall (SRH) recombination in the space charge region of the photodiode (Ishaque & Salam, 2011). Despite its widespread use, this approximation may lead to slight overestimations of depletion-region recombination in some cases (McIntosh, Altermatt, & Heiser, 2000).

The conventions followed in this section are the same as in preceding similar work (Sinapis, et al., in press; Tzikas, 2015). This is similar to the procedure described in the PV cell theory (§ 2.4).

### 3.5.2 – Series and shunt resistances

In this study the series and shunt resistances ($R_s$ and $R_{sh}$) are determined for each panel as a whole instead of cell-wise. This is done by adjusting the thermal voltage to match 60 cells in series in Equation 2.18, and by multiplying the first three of four right-hand side (RHS) terms in Equation 2.17 by the number of cells circuited in parallel, $N_p$. As $N_p = 1$ in this research, this has no net effect on the outcome of the equations. Refer to Annex F for an illustration of the used algorithm.

### 3.5.3 – Substring IV curve algorithm

The substring level in the PV system is of particular interest in this research. This level represents the system building blocks causing differentiation in system (DC) energy yield values when their size is adjusted (see Figure 1.4b). The algorithm used in previous similar work (Sinapis, et al., in press; Tzikas, 2015) is improved by excluding previous substring IV response approximations for voltage values near the open-circuit voltage ($V_{OC}$). In order to so an updated algorithm (Suckow, Pletzer, & Kurz, 2014) is used to calculate the IV response under the assumptions given so far. The equations outlined in § 2.4 are used for this purpose. See Annex G for the full algorithmic procedure and an accompanying flowchart.

## 3.6 – Panel DC output

The DC output is calculated per panel and is derived by adding up the voltages of individual substrings that are able to support a certain current *I* (also see Figure 3.6a). The IV-point yielding the maximum power (the MPP) gives the DC output for the given time step in the TMY simulation.

Modifying Equation 3.8 to express the substring temperature difference as a function of the difference of the other variables gives:

$$\Delta T_s = \Delta T_a + \Delta G_{eff}/(U_0 + U_1 \Delta W_{FF}) \quad (3.9a)$$

Recall from §2.3 that the effective substring irradiance is given by the most heavily shaded cell.

At a fixed point in time, no differences in wind speed and ambient temperature within the modeled field exist. Therefore:

$$\Delta T_s \propto \Delta\, G_{eff}/(U_0 + 0 \cdot U_1) \;\propto \Delta G_{eff} \quad (3.9b)$$

In other words, each substring facing the same effective irradiance at the same point in time will have equal effective temperatures. Therefore a sorting procedure that enforces substring IV curves to be ordered on irradiance in a descending fashion is sufficient to ensure the correct shape of the resulting panel IV curve.

The voltages for all substrings facing the same $G$ (and thus $T$ from Equation 3.9b) are directly multiplied with the number of identical occurrences in order to save the computation time required for substring IV curve addition. This effectuates a much faster procedure compared to computational addition of all substring IV curves when no preprocessing is done because the majority of substrings are effectively either fully shaded or fully unshaded at any point in time.

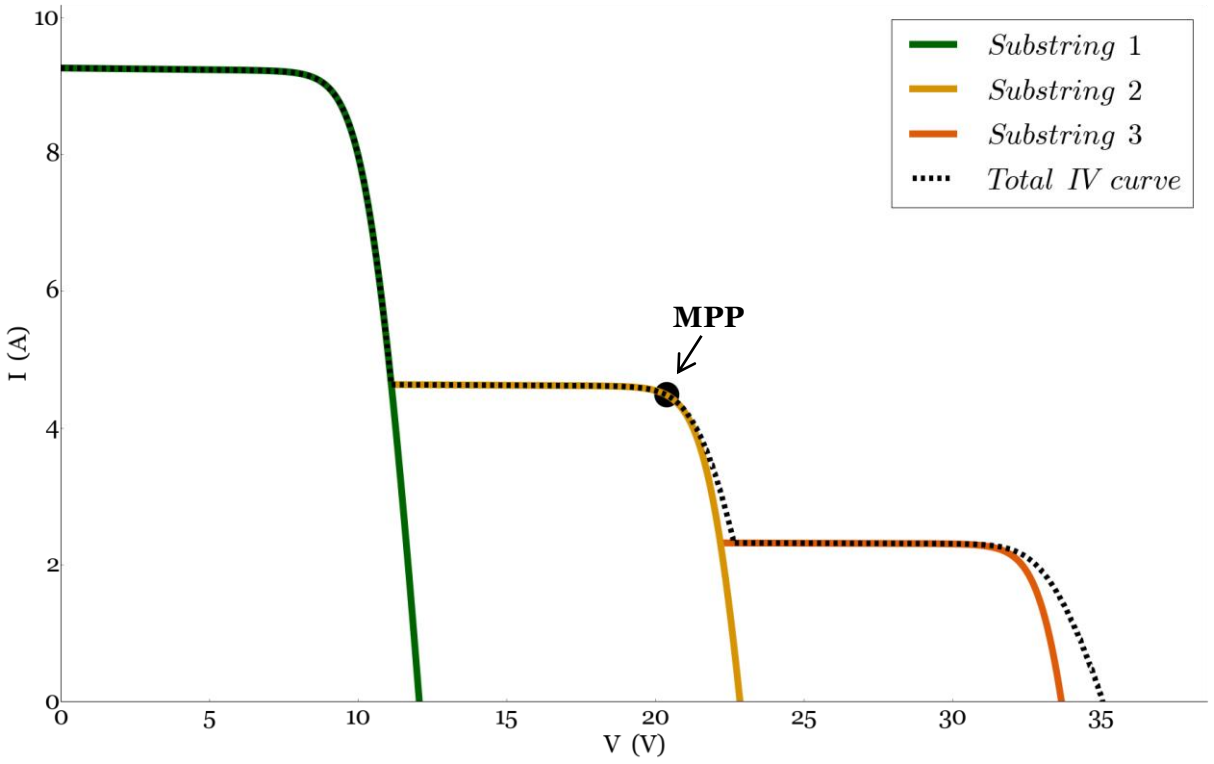


*Figure 3.6a: Example of three substrings ($G_{s1}$ = 1000 W/m²; $G_{s2}$ = 500 W/m2; $G_{s3}$ = 250 W/m2) connected in series and the resulting total IV response. This IV response is determined by addition of all substring voltages that can support a current (I) value anywhere on the individual substring IV curves.*

## 3.7 – System AC output

An overall MPPT tracking efficiency of 99.7% representing the fluctuations of MPPT algorithms around the true optimum is taken into account for all three system architectures mentioned here (Sinapis, et al., in press; Tzikas, 2015). The architecture-characteristic features are outlined below.

TMY AC system output values are determined by multiplying the AC output of a system with the representative time step (which is 5-minutely in the described model) and subsequently summing all per-time step energy contributions to obtain annual energy yield values.

### 3.7.1 – String inverter system

The Sunny Boy SB 2500TLST-21 is taken as central string inverter system because it falls within the same efficiency category as the devices taken for the PO and MI system architectures. Besides, it firmly matches the rated capacity of the modeled residential PV system.

In this system architecture the MPP is set for the entire system. This means that DC collection takes place at the system level instead of at the panel level. Consequently the IV response is modeled similar to the procedure in § 3.6, only now by adding up all substrings in the system simultaneously instead of per panel. The MPP is constrained to a voltage range of 180 V to 500 V by the central string inverter (PVSyst, 2014). The maximum AC output is 10.9A.

String inverter efficiency data was available for selected DC input power values (PVSyst, 2014) at system operating voltages of 180, 400 and 500 V. A double linear interpolation procedure is used to convert the discrete points ($P_i$,$V_i$) to continuous conversion efficiencies for any pair of ($P$,$V$) values of interest: first over power, subsequently over voltage. For the tabulated efficiencies taken from PV Syst, refer to Annex H.

A self-consumption criterion (PVSyst Help Files, n.d.) is used in order to smoothen out the losses at power values between the minimum power threshold (32W, also from PV Syst) and 160 W:

$$\eta_{SI} = (P_{MPP} - 160.0 \cdot (1 - \eta_{SI\,@\,160\,W}))/P_{MPP} \qquad (\text{if } 32\text{ W} \leq \text{P}_{\text{MPP}} < 160\text{ W}) \qquad (3.10)$$

In the equation above, $\eta_{SI}$ represents the string inverter efficiency.

### 3.7.2 – Power optimizer system

The maximum power point for each panel is set between an allowed operating voltage range of 8 V to 42 V (PVSyst, 2014). This matches the Femtogrid PV300 power optimizer requirements.

Linear interpolation over voltage is done over the two closest-neighboring forms of Equation 2.29 in order to determine the DC-DC conversion power losses. If the voltage is at one of the outward edge intervals, the equation corresponding to the closest neighboring voltage value is used directly.

Subsequently, Equation 2.30 is applied to account for the power losses due to conversion in the selected central string inverter of type Femtogrid Kratos Inverter 2400. Note that this procedure requires summing up all panel-wise PO power output values to obtain the total central inverter power, current and voltage input. The input current is constrained to lie within the range of 0.03 A to 6.7 A while the AC output current cannot exceed 10.5 A @ 230 V (PVSyst, 2014).

### 3.7.3 – Micro-inverter system

The maximum power point for each panel (also see § 3.6) is now constrained between a possible operating voltage range of 16 V to 48 V. This matches the characteristics of a Heliox SMI300 micro-inverter (PVSyst, 2014). As mentioned in § 2.6, DC-to-AC conversion takes place at the panel level in a single step.

Linear interpolation over voltage is done over the two closest-neighboring forms of Equation 2.31 in order to obtain the MI conversion power losses. The equation corresponding to the closest neighboring voltage value is used directly if the voltage is at one of the outward edge intervals as is done for the PO-case. The minimum per-panel input and maximum per-panel AC output values are 5.0 $W_{DC}$ and 285.0 $W_{AC}$ respectively (PVSyst, 2014).

Finally the system power output is determined by summing up the AC power output of every individual panel.

### 3.7.4 – MPP tracking

For reasons of simplicity and reproducibility all system architectures are modeled as perfect MPP tracking devices besides the 99.7% MPPT efficiency step. This means that they always find the global maximum power point per panel or per system instantaneously throughout the TMY simulation. In reality this is not the case. Particularly string inverter system architectures can have severe difficulties tracking the MPPT under partial shading (Sinapis, Litjens, Donker, & Folkerts, 2015; Sinapis, et al., in press). To investigate the effects of poor MPPT tracking, the string inverter system architect is simulated for two tracking cases: perfect MPP tracking or shadow mode "on" and poor MPP tracking or shadow mode "off".

"Poor" MPP tracking is incorporated by enforcing the local maximum containing the voltage closest to the open-circuit voltage upon the system at all times. The full IV response is determined first as in the other cases. However, the maximum current cutoff value is subsequently set to the short-circuit value of the heaviest shaded substring. This is done to ensure that the correct rightmost local MPP is found throughout the TMY simulation.

## 3.8 – Validation procedure

A validation procedure is undertaken as part of this work in order to verify the accuracy of the updated energy yield model. For this purpose daily MLPM system yield outcomes are compared for three situations: 1) the model used here; 2) the previous version of the energy yield model (Sinapis, et al., in press); and 3) actual measured system output. The system of interest is the Heliox per-module micro-inverter with 3 BPDs per module. Secondary effects characteristic to the direct environment of the field test, namely cable power losses, cabinet power losses and anisotropic reflection effects caused by a proximate white wall, are excluded in the simulation runs of both models. This is done in order to avoid modifying this work's model to specifically match the exact MLPM field test circumstances. Minutely global horizontal irradiance data from TU Eindhoven, located 5 km from the field test site, is used as input for the Reindl-2 (Reindl, Beckman, & Duffie, 1990) direct-diffuse irradiance separation procedure. Minutely in-plane irradiance data is retrieved directly from pyranometers installed in the test field set-up. Both these steps align with the methodology used for the previous yield model.

## 3.9 – Performance indicators

In the results section of this work, extensive emphasis is laid on three key energy-related indicators. Firstly, the specific energy yield of the studied PV systems (AC) and the individual modules (DC). Secondly, the relative energy yield lost due to shading. Thirdly, the relative potential (energy yield) benefits of applying additional BPDs within the PV systems of interest. The latter indicator is expressed in two ways: as a fraction of the total energy yield in unshaded conditions and as a fraction of the energy lost due to shading in the reference case of 3 BPDs per module. Table 3.9.1 summarizes the chosen definitions.

These indicators have been named variably in similar literature. In terms of the specific energy yield ($E_{spec}$) with unit kWh/kW$_p$, the convention used in this study is a normalization of absolute yield values with respect to the rated capacity ($E_{rated}$) of the PV systems:

$$E_{spec} = E_{total}/E_{rated} \tag{3.11}$$

Deline, Marion, Granata & Gonzalez (2011) labeled the concept of relative shade-induced yield losses as "system loss" and "power lost to shade". Sinapis et al. (in press) referred to "yield losses". Deline, Meydbray, Donovan & Forrest (2012) quantified shading losses with the term "normalized power". In this work the nomenclature of Hanson, Deline, MacAlpine, Stauth & Sullivan (2014) is used. Therefore the relative shade-induced yield losses are referred to as the shading index (SIDX). It is defined as a percentage using both the unshaded and shaded cases:

$$SIDX = 100\,\% \cdot (E_{unshaded} - E_{shaded})/E_{unshaded} \tag{3.12}$$

Relative potential yield benefits of shade-mitigating applications inside PV systems have been reported as "annual power gain potential" (MacAlpine, Brandemühl, & Erickson, 2011) and "performance improvement" (Deline, Meydbray, Donovan, & Forrest, 2012) amongst others. In this study the relative potential yield benefits are referred to as the potential benefits (PB). The potential benefits (PB) are defined relative to the reference case and the unshaded energy yield:

$$PB = 100\,\% \cdot (E_{shaded,added\ BPDs} - E_{shaded,3\ BPDs})/E_{unshaded} \tag{3.13}$$

The yield benefits related to increased BPD insertion can also be expressed as a fraction of mitigated losses relative to the shade-related yield losses in the reference case. As in the work of Hanson, Deline, MacAlpine, Stauth & Sullivan (2014), this concept is referred to as the shade mitigation factor (SMF) here:

$$SMF = 100\,\% \cdot (E_{shaded,added\ BPDs} - E_{shaded,3\ BPDs})/(E_{unshaded} - E_{shaded,3\ BPDs}) \tag{3.14a}$$

Equivalently, dividing Equation 3.13 by Equation 3.12 provides another definition of the SMF:

$$SMF = 100\% \cdot PB/SIDX \tag{3.14b}$$

Table 3.9.1: Overview of used partial shade performance indicators

| Indicator | Explanation |
|---|---|
| *SIDX* | Fraction of energy yield lost due to the presence of shade objects. Expressed relative to the yield calculated for the unshaded case. |
| *PB* | Fraction of energy yield that can be recovered by the use of *X* BPDs per module instead of 3. Expressed relative to the unshaded yield. |
| *SMF* | Fraction of *X* BPD-induced yield recovery benefits relative to the initial 3 BPD-case shade-induced yield losses. Expressed relative to the SIDX. |

# Chapter 4: Results

The results of this study are presented in this fourth chapter. The reported results mainly revolve around the partial shade system yield performance indicators as listed in § 3.9. Figure 4.a shows an additional illustration of the used performance indicators.

This chapter is outlined as follows. The first paragraph lists the typical meteorological year (TMY) results for a 40° tilted southward orientation of the studied PV systems. Both a per-module DC and a per-system AC perspective are considered. The subsequent paragraphs elaborate on the sensitivity results with respect to orientation (§ 4.2) and geographic location (§ 4.3) of the PV systems of interest. Note that the tilt is kept constant at 40° in all these sensitivity cases and that all annual results presented hold for TMY simulations. § 4.4 provides a summarizing illustration of the general and sensitivity simulation runs. Finally, § 4.5 lists the key results related to the undertaken validation procedure.

Additional results are available in accompanying Appendices. Per-panel DC shading index values for each BPD case are listed in Annex I. South-east and south-west orientation roof sensitivity results are shown in Annex J. The geographic sensitivity results for Oslo and Paris are presented in Annex K. Validation procedure graphs and tables are provided in Annex L.

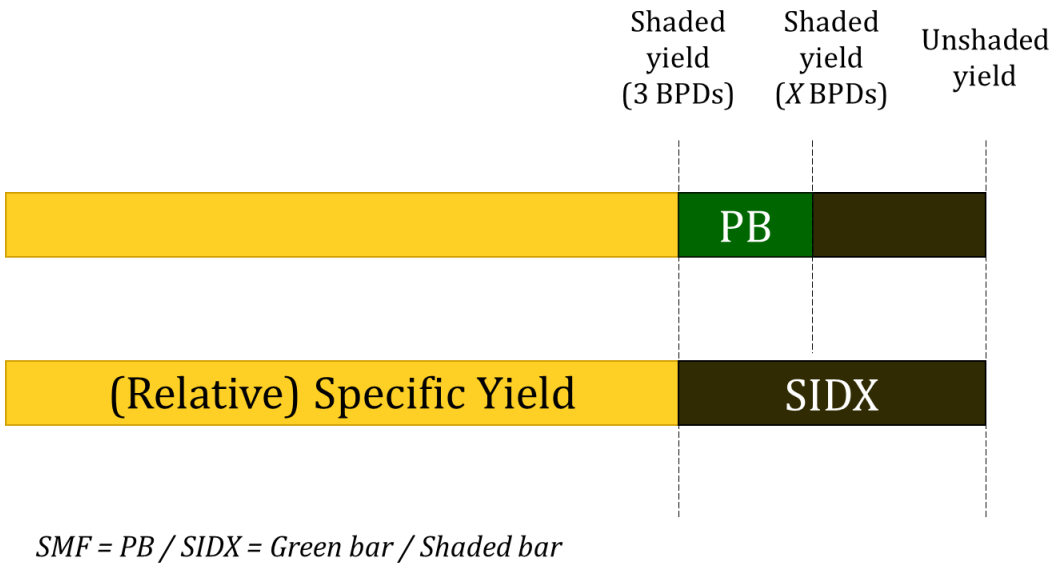


*Figure 4.a: Illustration of the performance indicators used in this work. Note that the relative specific yield + SIDX equal the unshaded yield (which is fixed at 100%). The potential benefits (PB) related to applying X BPDs per module instead of three are indicated by dark-green bars. The shade mitigation factor (SMF) is defined as the area of the green bar divided by the area of the shaded bar. This indicator shows the fraction of recoverable yield relative to the "reference" shade-induced losses. A SMF of 50% would mean that 50% of the shade-induced losses in the reference case can be recovered by applying X BPDs per module.*

## 4.1 – Typical-year results

### 4.1.1 – Per-module DC results

The effect of shading on the DC energy production of each individual panel in the simulated environment is shown in Figure 4.1b. Refer to Figure 3.1b for an overview of the used panel numbering convention. Note that the DC results exclude the effects of system architectures. These are incorporated in the AC results. The reference case, as depicted by the dark-yellow bars, includes 3 BPDs per module. The accompanying percentage score shown in black illustrates the relative specific panel yield compared to the unshaded case. Unshaded situations would lead to a relative yield percentage score of 100%. Black bars indicate the shading index as a result of the aggregate shading scenario applied. Green bars and the percentage scores placed directly above show the potential benefits attained by increasing the amount of per-module BPDs from 3 to 60. This can be interpreted as the maximum recovery potential that can be attributed to applying more BPDs in each module. Individual effects of dormers, poles and chimneys are shown by the use of thin orange, dark-red and light-blue bars placed below each panel's performance indication bars. The dashed grey lines indicate specific yield performance values in kWh/kW$_p$. Refer to Figure 4.1a for an overview of the discussed graphical conventions. These apply to all DC result figures throughout this work.

Figure 4.1c shows the potential benefits associated with each subsequent per-module BPD-amount case considered in this study. Table 4.1.1 shows the shade mitigation factors for each panel given each BPD-granularity case considered here.

The per-module DC results illustrate that the shading index values related to chimneys are relatively modest (< 1%) for the south-oriented roof. The exhaust pipes only significantly affect top-right panel 3. Dormers have a thorough influence on panels 4 through 9. The left- and right-middle panels numbered 5 and 8 experience the most intense yield losses with shading index values of 13.2% and 11.4% respectively.

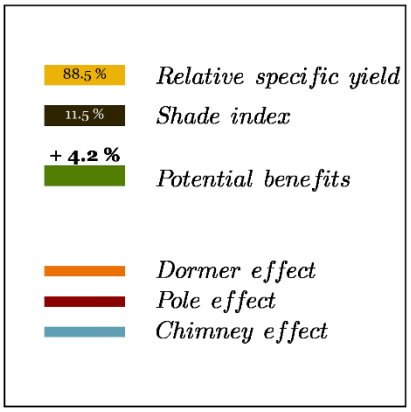


*Figure 4.1a: Legend accompanying the DC yield figures in this report.*

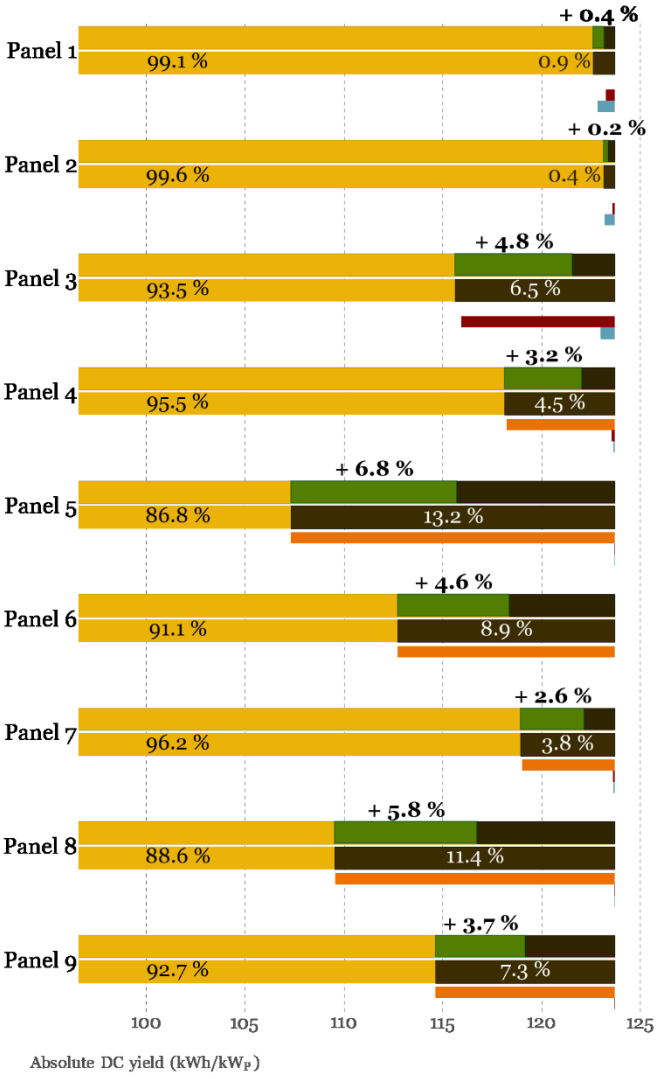


*Figure 4.1b: TMY per-panel specific yield, shading index values and potential (yield recovery) benefits when the amount of BPDs per module is increased from three to 60. The accompanying legend is shown in Figure 4.1a.*

The per-panel shading index values shown here are highly dependent on the casted shade shapes and the area of the module these shapes tend to cover. For this reason the losses related to module proximity to dormers are more intense than those associated with chimney and exhaust pipe proximity of panels for a southward roof orientation.

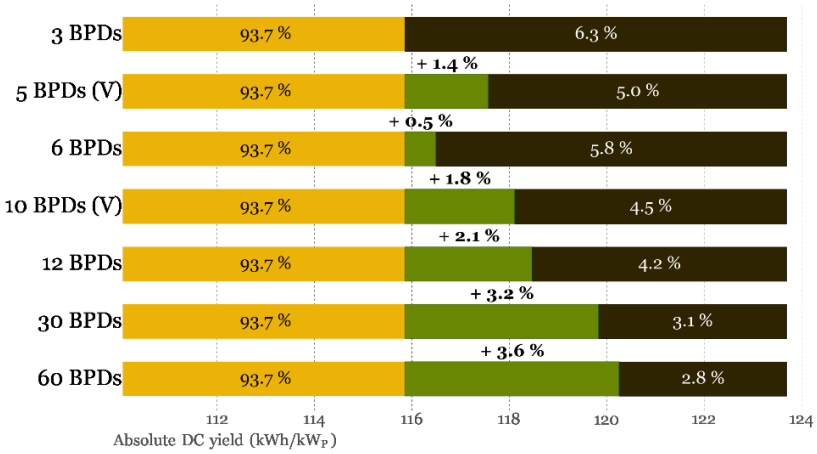


*Figure 4.1c: TMY DC yield results averaged over the nine panels. Shading index values and recovery benefits when increasing the amount of BPDs per module in a stepwise fashion from 3 to 60 are illustrated. The accompanying legend is shown in Figure 4.1a.*

Figure 4.1c shows that the potential benefits tend to increase as the amount of BPDs per panel is raised. This can be explained by a higher degree of bypassing flexibility with respect to specific module surface parts when the BPD-amount is increased. This in turn reflects a higher degree of flexibility with regard to tailoring the module response to the specific shadow shapes casted on individual module surfaces. Refer to § 1.4 for an illustrated example. One exception to this trend is seen when switching from 5 to 6 BPDs per panel. The reason for this behavior lies in the effects of dormer shading. Dormer shading is the dominant factor contributing to shade-related yield losses in most of the panels and will therefore be strongly reflected in the average results depicted in Figure 4.1c. As the casted dormer shade shape is triangular and stretches along the panels horizontally, vertically aligned substrings tend to lead to lower DC output losses compared to horizontally aligned substrings even if their amount is slightly lower.

Table 4.1.1 illustrates that the per-panel shade-loss mitigation factors (SMFs) have a decreasing dependency on the shade shapes casted on the panel by proximate objects if the amount of BPDs per module is increased. This can be explained by the fact that the substring shapes tend to become less elongated and more square-shaped if the amount of BPDs is strongly increased. The effect hereof is that panel sensitivity to shades of specific shapes is reduced. Certainly for the 12, 30 and 60 per-panel BPD cases, the shade mitigation factors are relatively constant across all panels despite the strong heterogeneity in shading index values.

Note that for panel 1 the case of 5 BPDs results in DC output losses higher than the reference case.

Table 4.1.1 – Per-panel shade-loss mitigation factors for each BPD scenario

| Panel # | Ref. of 3 BPDs | 5 BPDs (V) | 6 BPDs | 10 BPDs (V) | 12 BPDs | 30 BPDs | 60 BPDs |
|---|---|---|---|---|---|---|---|
| Panel 1 | - | -3 % | 21 % | 2 % | 36 % | 47 % | 50 % |
| Panel 2 | - | 5 % | 11 % | 10 % | 27 % | 40 % | 44 % |
| Panel 3 | - | 25 % | 19 % | 35 % | 47 % | 67 % | 73 % |
| Panel 4 | - | 17 % | 14 % | 27 % | 46 % | 65 % | 70 % |
| Panel 5 | - | 31 % | 2 % | 36 % | 26 % | 45 % | 51 % |
| Panel 6 | - | 15 % | 8 % | 21 % | 32 % | 47 % | 51 % |
| Panel 7 | - | 14 % | 14 % | 23 % | 45 % | 63 % | 68 % |
| Panel 8 | - | 29 % | 3 % | 34 % | 26 % | 45 % | 51 % |
| Panel 9 | - | 12 % | 8 % | 19 % | 32 % | 46 % | 50 % |

### 4.1.2 – System AC results

Figure 4.1e shows the per-system-architecture AC results of the undertaken TMY simulation. The four PV system architectures of interest are string inverters without (SI-) and with (SI+) activated shadow function, power optimizers (PO) and micro-inverters (MI). Relative specific yield percentages, shade indices and relative BPD-related yield recovery potential benefits (PBs) are shown in a fashion strongly similar to the DC figures. Individual effects of dormers, exhaust pipes and chimneys are indicated by thin orange, dark-red and light-blue bars. A complete legend for the AC result figures used in this report is given in Figure 4.1d. Figure 4.1f illustrates the potential yield recovery benefits associated with each per-panel BPD amount case considered in this report.

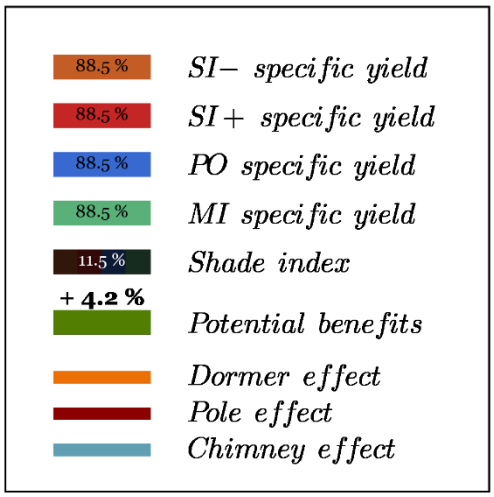


*Figure 4.1d: Legend accompanying the AC yield figures in this report.*

Figure 4.1e illustrates that the dormer effect is the dominating cause of shade-induced yield losses on the system level. This aligns with the observations of the panel-averaged DC results (Figure 4.1c).

In general the simulated partial shading conditions affect the SI yield figures most intensively. The shading index values and potential benefits are almost equal for the PO and MI-type systems. These observations are explained by the fact that central-inverter (SI) MPP tracking systems are more thoroughly affected by partial shading compared to (PO and MI) per-panel MPP tracking in the first place. The latter fact makes the PO and MI-type systems and their relative yield results strongly similar.

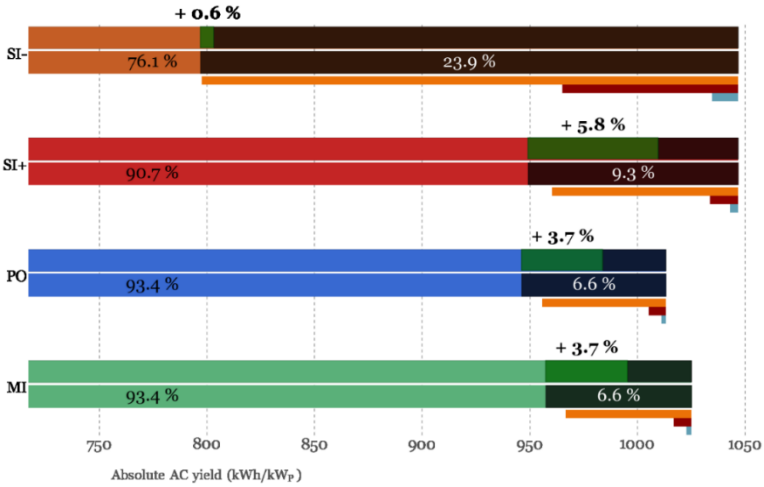


*Figure 4.1e: TMY specific AC yield, shading index values and potential benefits when increasing the amount of BPDs per module from 3 to 60 for string inverter with inactive (SI-) and active shadow function (SI+), power optimizer (PO) and micro-inverter (MI) system architectures. The accompanying legend is shown in Figure 4.1d.*

The MI-type system provides the highest absolute system output if the amount of BPDs per panel is 3 or 6 (Figure 4.1f). However, the SI system with active shadow function (SI+) surpasses the specific yield performance of the MI-type system for other per-panel BPD amounts. The fact that either the MI or the SI+ system types come out on top can be rationalized. The reason is that SI and MI only require single-step conversion whereas the PO system requires two conversion steps: DC-to-DC followed by DC-to-AC. This two-step conversion leads to lower overall conversion efficiencies and therefore lower specific yield figures for the PO-type system. The MI performance advantage at low BPD amounts can be attributed to MPP optimization per panel instead of system-wise for the SI-type system. This leads to a flexibility advantage of MI-type systems over SI-type

systems at low amounts of BPDs per module. The beneficial efficiency of the SI system combined with increased bypass flexibility of shaded module parts within the system makes it the best-performing system if the system bypassing flexibility is increased. These efficiency benefits are also indicated by higher specific yield figures under unshaded conditions (Fig. 4.2b and Fig 4.2c).

Another key insight is that effective MPP tracking is crucial for obtaining significant benefits from increasing the BPD granularity. The SI system that does not incorporate sophisticated MPP tracking barely benefits from increasing the amount of BPDs per module from three to 60 (~0.6%). On top of that, the overall shading losses are already significantly higher compared to the other system architecture configurations in the first place. Due to the negligible effect of adding more BPDs to this system type, the results of the other BPD cases are not shown for the SI- system in Figure 4.1f. As for the panel-averaged DC results, increasing the BPD granularity leads to higher potential benefits except for the 6 BPD vs. 5 BPD cases. The reason is the same as the one outlined in section 4.1.1. Table 4.1.2 shows the shade-loss mitigation factors (SMFs) per system. These are up to a range of 50% to 60% for the 30 BPDs and 60 BPDs cases for SI+, PO and MI systems. Also this is very similar to the results obtained in the DC part as described in section 4.1.1.

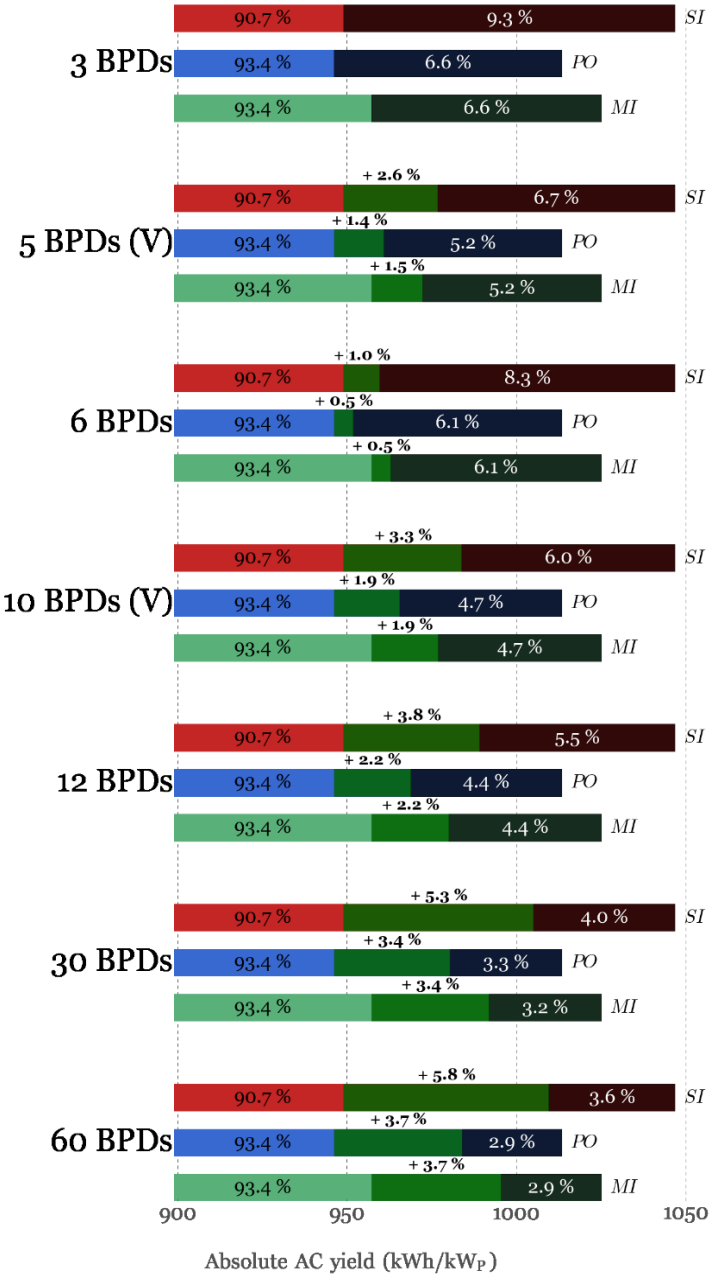


*Figure 4.1f: TMY AC yield results for SI(+), PO and MI systems. Shading index values and potential benefits when increasing the amount of BPDs per module in a stepwise fashion from 3 to 60 are illustrated. The legend is shown in Figure 4.1d.*

Table 4.1.2 – Per-system shade mitigation factor values for each BPD scenario

| System | Ref. of 3 BPDs | 5 BPDs (V) | 6 BPDs | 10 BPDs (V) | 12 BPDs | 30 BPDs | 60 BPDs |
|---|---|---|---|---|---|---|---|
| SI - | - | 1 % | 1 % | 1 % | 2 % | 2 % | 3 % |
| SI + | - | 28 % | 11 % | 36 % | 41 % | 57 % | 62 % |
| PO | - | 22 % | 8 % | 29 % | 34 % | 51 % | 56 % |
| MI | - | 22 % | 8 % | 29 % | 34 % | 51 % | 56 % |

## 4.2 – Roof orientation sensitivity

The first part of the sensitivity analysis involves changing the roof orientation. This is done in order to assess whether the results reported in § 4.1 hold similarly in other conditions. This section presents the main results for east (E) and west (W) roof orientations and provides comparisons to the south (S) orientation case when suitable. The south-east (SE) and south-west (SW) roof orientation results are shown in Appendix J in order to avoid a high degree of repetition.

### 4.2.1 – East

The specific DC energy production of each numbered panel in the simulated environment (see Figure 3.1b) for an eastward roof orientation is shown in Figure 4.2a.

Contrary to the southward case, the chimney now significantly affects the yield of panel 1 while the exhaust pipe does no longer influence the yield of panel 3 thoroughly. Furthermore the dormer now particularly affects the rightmost roof panel triplet. Note that the specific yield values are about 80% here compared to those for a southern roof orientation. These results fall in line with European PV orientation matrices and can be expected provided the dimensions of the roof.

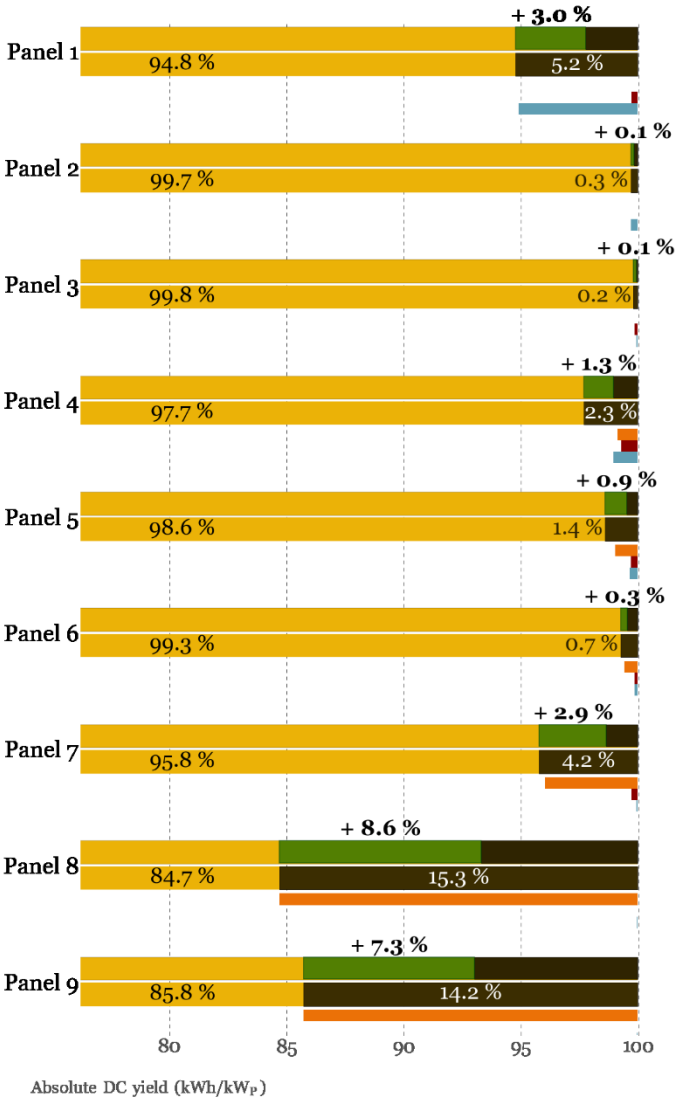


*Figure 4.2a: East-oriented roof TMY DC yield per panel, shading index values and potential benefits when the amount of BPDs per module is increased from 3 to 60. Figure 4.1a shows the legend.*

Figure 4.2b illustrates the panel-averaged effect of intensified BPD insertion. Still the dormers are the dominant reason for the yield losses. This explains that the switch from 5 vertically aligned BPDs to 6 horizontally aligned BPDs results in lower DC output despite an increase of the amount of BPDs. This is just as in the southward roof case. Generally the shading index values are lower than for the south-oriented roof. This is caused by a reduction in effective dormer shading, as only the rightmost roof triplet (panels 7, 8 and 9) are profoundly affected whereas panels 4, 5, 6, 7, 8 and 9 suffer substantial output losses due to dormer shading for the southward-oriented roof (Figure 4.1b). Nevertheless, the average DC shade mitigation factor values are very comparable to the southward case (Table 4.2.1).

The strong similarity in results is also reflected in the system AC values. Overall the relative yield losses and benefits are slightly lower than for the south-oriented row house roof. The chimney effect on system output is also

more apparent now. This is at the cost of the exhaust pipe effect compared to the southward case. Overall the dormer remains the dominant contributing factor with regard to system yield losses. Also refer to Figure 4.2c.

The micro-inverter (MI) system again has the highest yield figures if the amount of BPDs is 3 or 6. In the other cases the string inverter (SI) system with active shadow mode comes out on top (Figure 4.2d). This is the same as for the south-oriented roof scenario.

Table 4.2.1 lists the shade-loss mitigation factor (SMF) values for the per-module DC average and for all PV system architectures studied in this work. Besides small relative changes, the general picture is highly similar to the results presented for the southern roof simulation. Again the SMF values are up to a range of 50 % to 60 % for the 30 BPDs and 60 BPDs cases for SI+, PO and MI systems. The same observation holds for the DC-average.

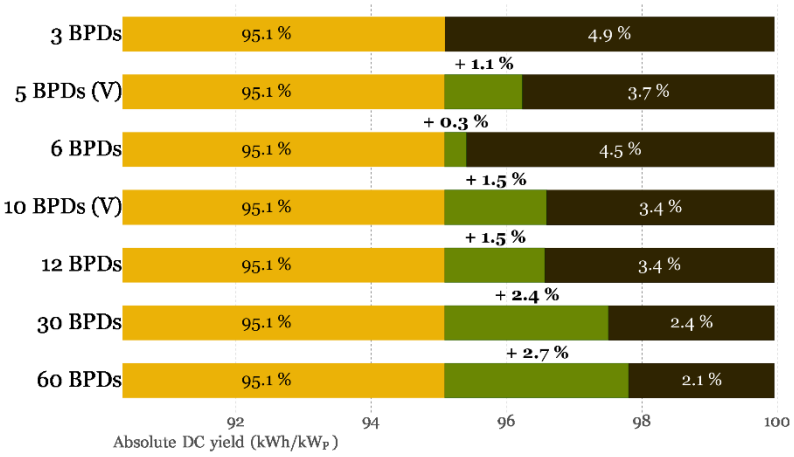


*Figure 4.2b: East-oriented roof TMY DC yield results averaged over the nine panels. Shading index values and potential benefits when increasing the amount of BPDs per module are illustrated. Figure 4.1a shows the accompanying legend.*

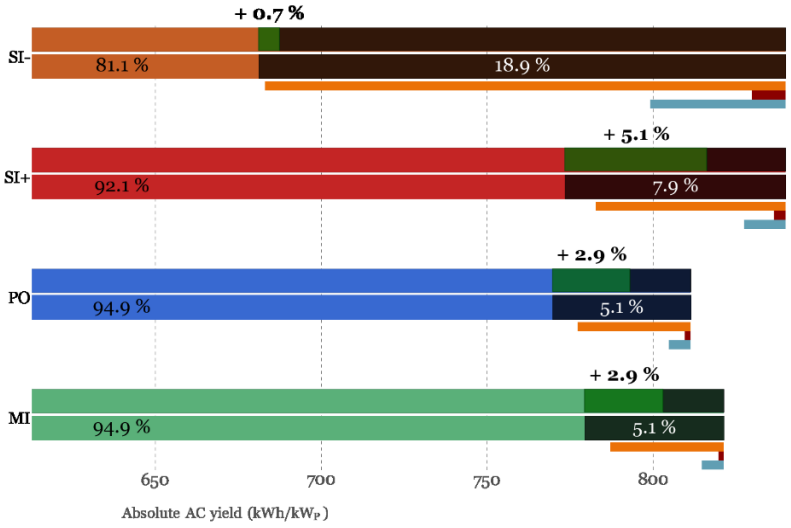


*Figure 4.2c: East roof TMY AC yield, shading index values and potential benefits when increasing the amount of BPDs per module from 3 to 60 for string inverter with inactive (SI-) and active shadow function (SI+), power optimizer (PO) and micro-inverter (MI) system architectures. The accompanying legend is shown in Figure 4.1d.*

Table 4.2.1 – East DC-averaged and per-system shade loss mitigation factors for each BPD case

| System | Ref. of 3 BPDs | 5 BPDs (V) | 6 BPDs | 10 BPDs (V) | 12 BPDs | 30 BPDs | 60 BPDs |
|---|---|---|---|---|---|---|---|
| DC-avg. | - | 22 % | 6 % | 31 % | 31 % | 49 % | 55 % |
| SI - | - | 2 % | 1 % | 2 % | 2 % | 4 % | 4 % |
| SI + | - | 34 % | 9 % | 41 % | 41 % | 59 % | 64 % |
| PO | - | 24 % | 7 % | 31 % | 30 % | 50 % | 56 % |
| MI | - | 24 % | 7 % | 31 % | 31 % | 50 % | 56 % |

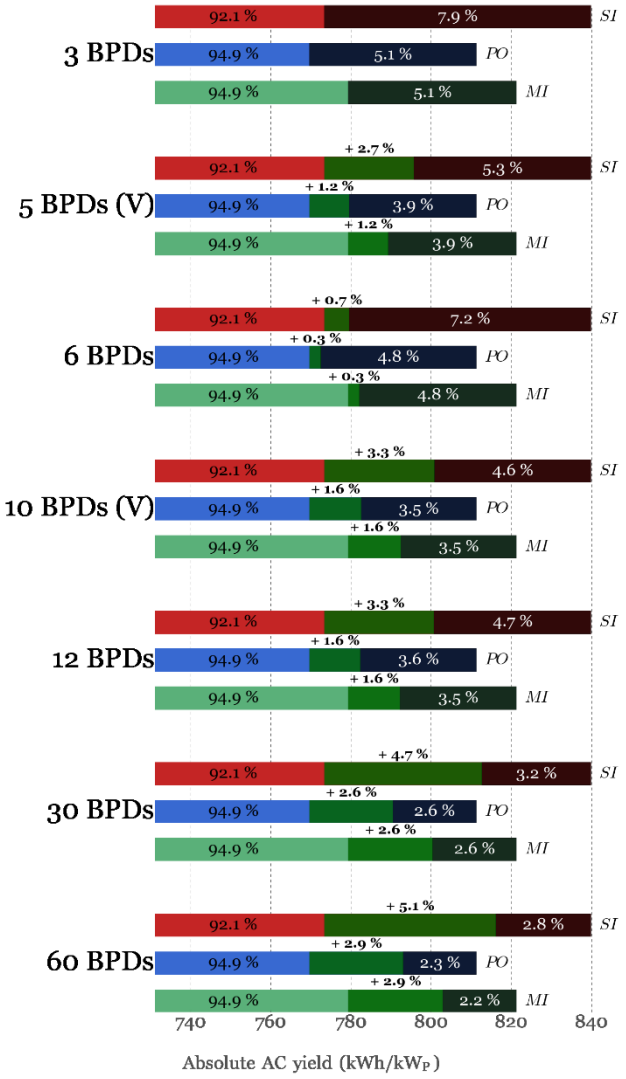


*Figure 4.2d: East-roof TMY AC yield results for SI(+), PO and MI systems. Shading index values and potential benefits when increasing the amount of BPDs per module in a stepwise fashion from 3 to 60 are illustrated. The legend is shown in Figure 4.1d.*

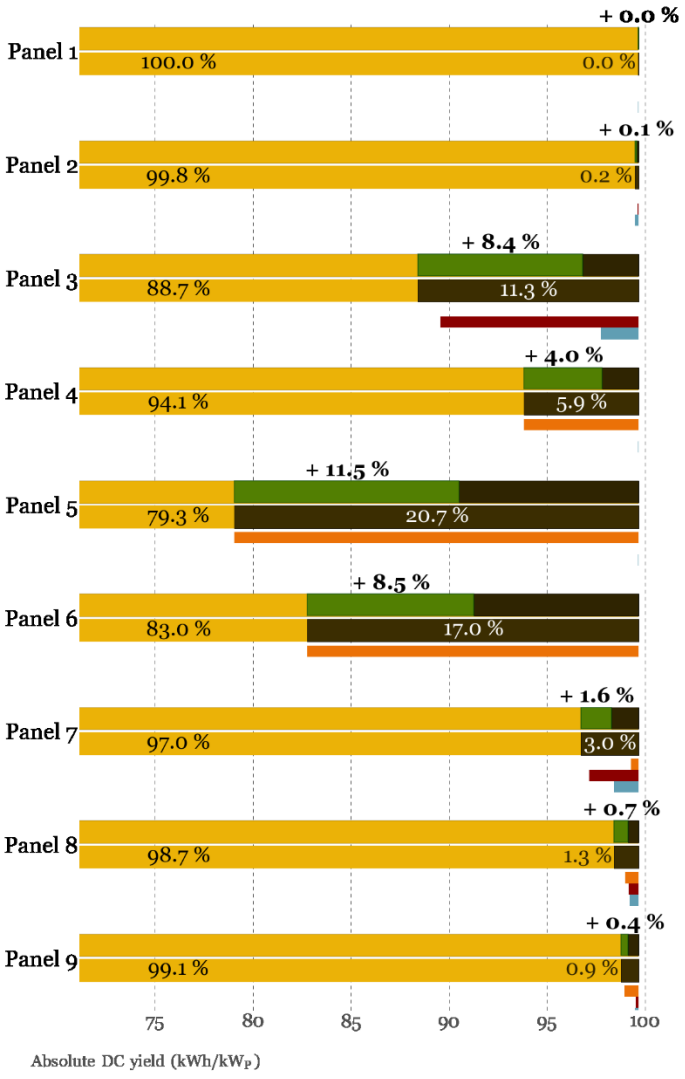


*Figure 4.2e: West-oriented roof TMY DC yield per panel, shading index values and potential benefits when the amount of BPDs per module is increased from 3 to 60. Figure 4.1a shows the legend.*

### 4.2.2 – West

The specific DC output of each panel in the simulated environment for a westward roof orientation is shown in Figure 4.2e. Refer to Figure 3.1b for the panel numbering convention used. In this case panels 1 and 2 are virtually unshaded. At the same time modules 3 and 7 are most heavily affected by the exhaust pipes. The dormers particularly affect the specific energy yield of the most leftward module triplet. Note that all absolute yield values are about 80% here compared to those for a southern roof orientation, just as in the eastward case. Again these trends are as expected.

Figure 4.2f illustrates the panel-averaged effect of applying more BPDs throughout the PV system. The switch from 5 vertically aligned BPDs to 6 horizontally aligned BPDs is again the only situation in which more BPDs leads to lower potential yield benefits (Figure 4.2f) for the same reason as for the east- and south-oriented roofs. Average DC shade mitigation factor values (Table 4.2.2) are also highly comparable to the other roof orientation cases.

Again the AC results are strongly similar to the other orientation cases. The dormers are the dominant contributing factor, although the contributions of exhaust pipes and chimneys are significantly present as well in this case. Overall the shade-related aggregate system output losses due to shading are most severe in this westward roof case. Consequently the potential benefits are slightly higher compared to the two roof orientation cases treated earlier. Also see Figure 4.2g.

As in the other two orientation situations, the MI provides the highest AC system output when the amount of BPDs is 3 or 6. However, the SI system comes out on top at higher BPD amounts (Figure 4.2h). Note that the PO also outperforms the SI system for the reference amount of BPDs.

Table 4.2.2 shows the shade-loss mitigation factors (SMF) for the DC average and all PV system architectures investigated in this study. Besides small relative changes, the general picture is again very similar to the other roof orientation cases. As reported earlier for the other orientation directions, the SMF values reach up to a range of 50 % to 60 % for the 30 BPDs and 60 BPDs cases for SI+, PO and MI systems. The same trends are presented for the DC-average.

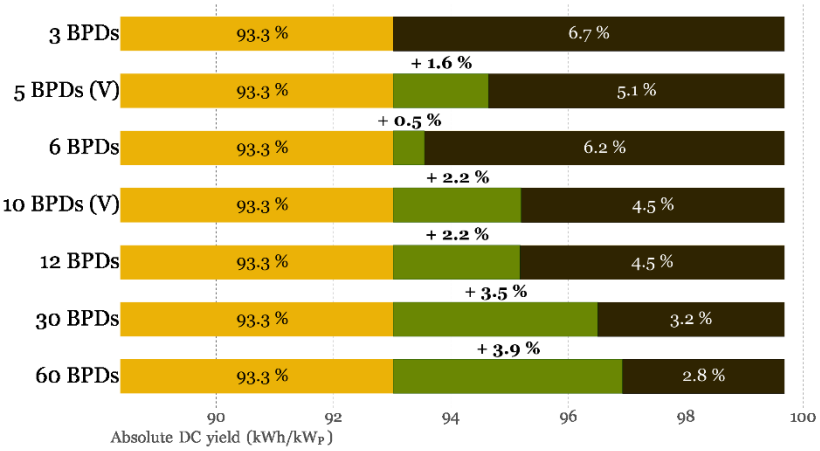


*Figure 4.2f: West-oriented roof TMY DC yield results averaged over the nine panels. Shading index values and potential benefits when increasing the amount of BPDs per module are illustrated. Figure 4.1a shows the accompanying legend.*

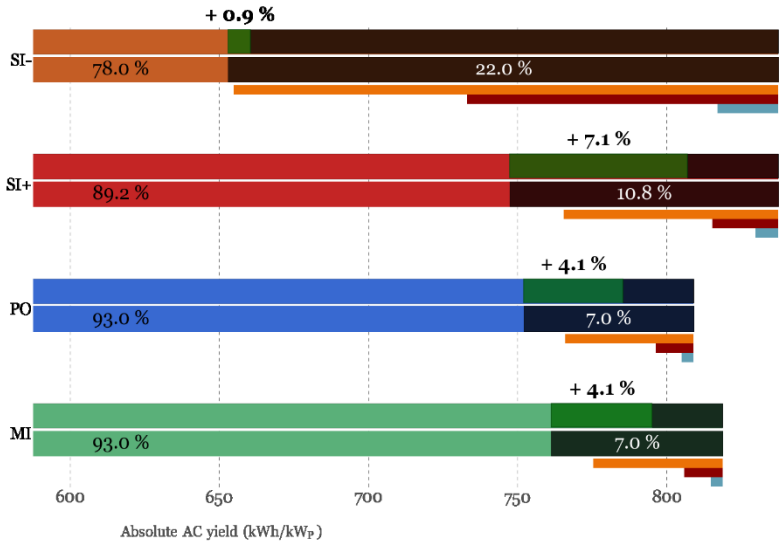


*Figure 4.2g: West roof TMY AC yield, shading index values and potential benefits when increasing the amount of BPDs per module from 3 to 60 for string inverter with inactive (SI-) and active shadow function (SI+), power optimizer (PO) and micro-inverter (MI) system architectures. The legend is shown in Figure 4.1d.*

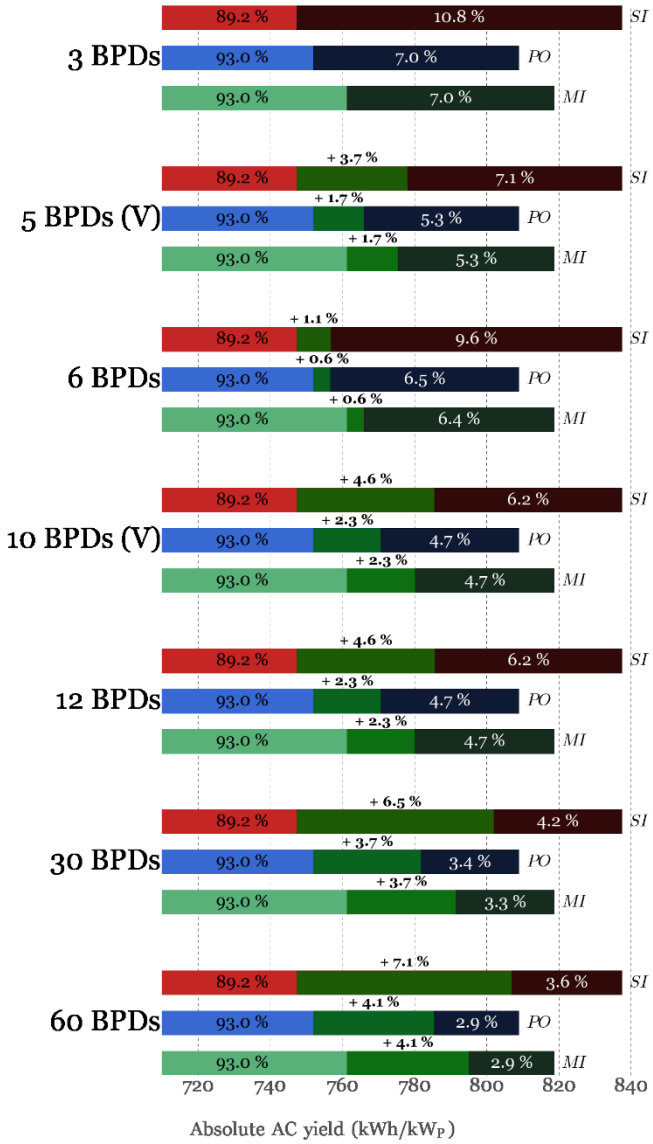


*Figure 4.2h: West-roof TMY AC yield results for SI(+), PO and MI systems. Shading index values and potential benefits when increasing the amount of BPDs per module in a stepwise fashion from 3 to 60 are illustrated. The accompanying legend is shown in Figure 4.1d.*

Table 4.2.2 – West DC-averaged and per-system shade loss mitigation factors for each BPD case

| System | Ref. of 3 BPDs | 5 BPDs (V) | 6 BPDs | 10 BPDs (V) | 12 BPDs | 30 BPDs | 60 BPDs |
|---|---|---|---|---|---|---|---|
| DC-avg. | - | 24 % | 7 % | 33 % | 33 % | 52 % | 58 % |
| SI - | - | 2 % | 1 % | 3 % | 3 % | 4 % | 4 % |
| SI + | - | 34 % | 10 % | 42 % | 43 % | 61 % | 66 % |
| PO | - | 24 % | 8 % | 33 % | 33 % | 52 % | 59 % |
| MI | - | 24 % | 8 % | 33 % | 33 % | 52 % | 59 % |

## 4.3 – Geographic location sensitivity

Another crucial sensitivity component is the geographic location. This is because incident solar angles and direct-diffuse radiation ratios vary among different places on Earth. As mentioned in the research framework (§ 1.5), Reykjavik and Oslo are chosen to represent low-irradiance comparison cases. On the contrary, Paris and Madrid are chosen because of their relatively high irradiance levels and sunnier conditions than Eindhoven. See § 3.3 for the input values used.

To avoid a high degree of repetition throughout the presentation of the results in this section, only the results of Reykjavik and Madrid are treated elaborately. Besides, only the AC output of the studied system architectures are evaluated in this sensitivity part. Refer to Annex K for the results regarding Oslo and Paris.

### 4.3.1 – Reykjavik

The specific yield values are significantly lower compared to Eindhoven if the location is set to the capital city of Iceland. However, the shading index values and potential benefits associated with applying more BPDs are remarkably similar to the Eindhoven case when comparing the outcomes shown in Figures 4.1e and 4.3a.

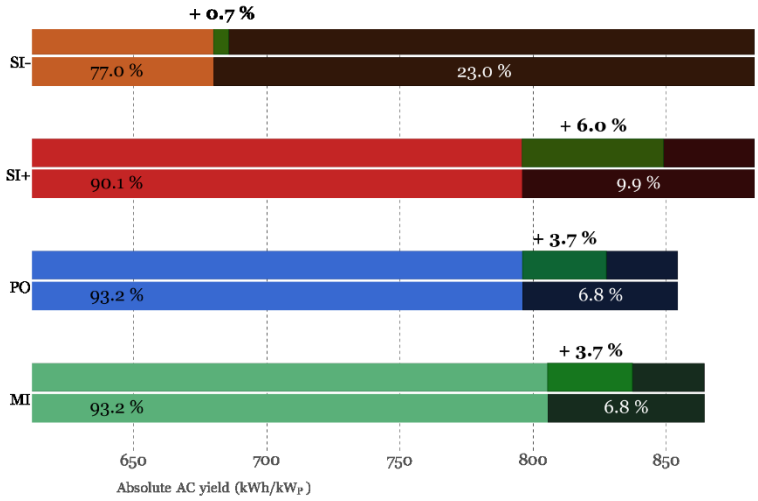


*Figure 4.3a: TMY AC yield, shading index values and potential benefits when increasing the amount of BPDs per module from 3 to 60 for string inverter with inactive (SI-) and active shadow function (SI+), power optimizer (PO) and micro-inverter (MI) system architectures in Reykjavik. Figure 4.1d shows the legend.*

In terms of system output, the MI comes out on top if the amount of BPDs is 3 or 6. This is similar to the observations for the other considered cases. However, the performance of the PO system also surpasses the SI system in the reference case of 3 BPDs here. In the case of 5 BPDs per module or more, the SI system with active shadow function harbors the highest system output figures again. See Figure 4.3b for an accompanying illustration.

Also strongly similar to the other cases considered so far are the figures for the shade-loss mitigation factor values. These again reach up to 50 – 60 % for the conditions representing 30 and 60 BPDs per module.

Table 4.3.1 – Reykjavik per-system shade loss mitigation factor values for each BPD case

| System | Ref. of 3 BPDs | 5 BPDs (V) | 6 BPDs | 10 BPDs (V) | 12 BPDs | 30 BPDs | 60 BPDs |
|---|---|---|---|---|---|---|---|
| SI - | - | 1 % | 1 % | 1 % | 2 % | 3 % | 3 % |
| SI + | - | 28 % | 10 % | 35 % | 40 % | 56 % | 61 % |
| PO | - | 20 % | 8 % | 27 % | 31 % | 48 % | 54 % |
| MI | - | 20 % | 8 % | 27 % | 31 % | 49 % | 54 % |

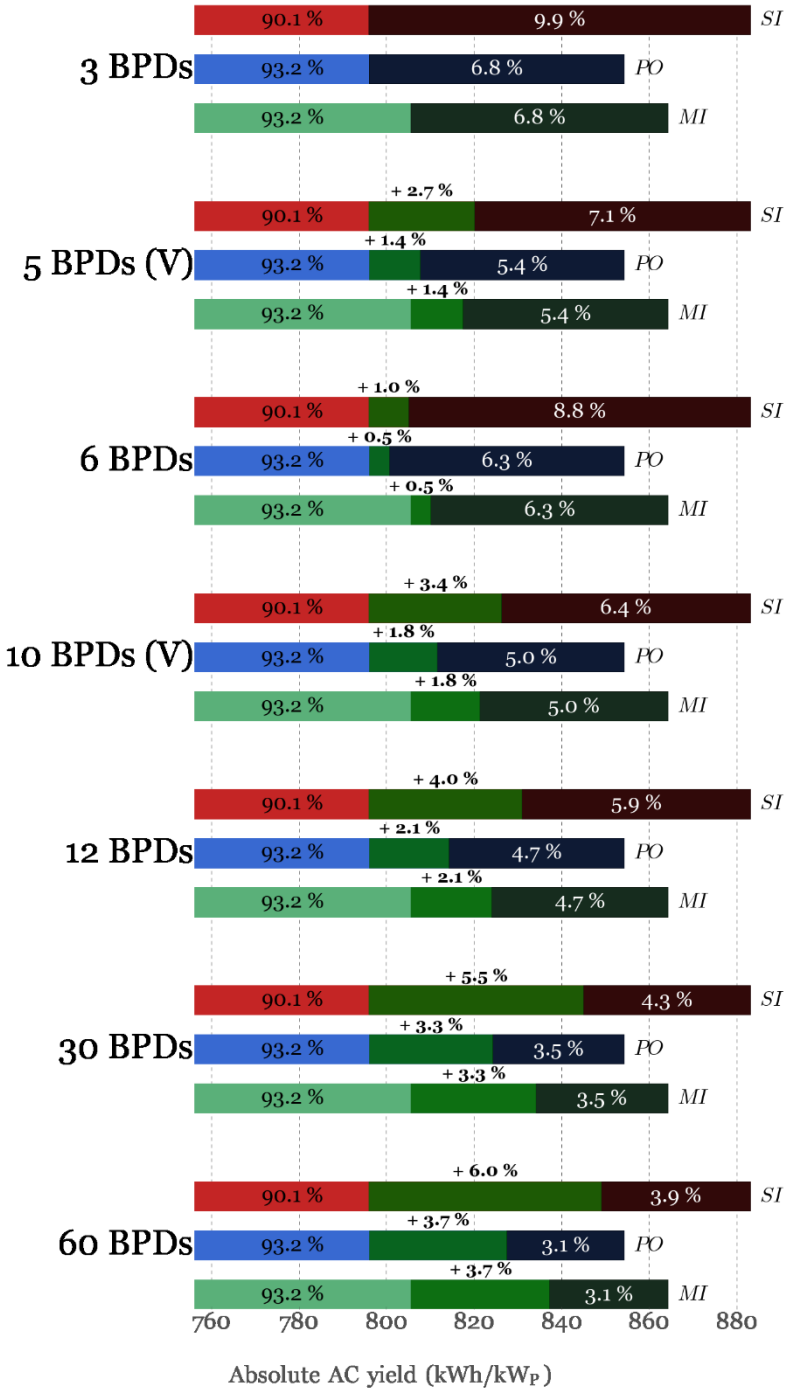


*Figure 4.3b: TMY AC yield results for SI(+), PO and MI systems placed in Reykjavik. Relative yield losses and relative yield recovery potential when incrementally increasing the amount of BPDs per module from 3 to 60 are illustrated. The accompanying legend is shown in Figure 4.1d.*

## 4.3.2 – Madrid

Specific yield values for the case of Madrid are significantly higher than those reported for Eindhoven and Reykjavik. Besides, the shading index values and the potential benefits associated with intensified BPD insertion substantially exceed those presented for to the other cases studied. Also compare Figure 4.3c with Figures 4.1e and 4.3a.

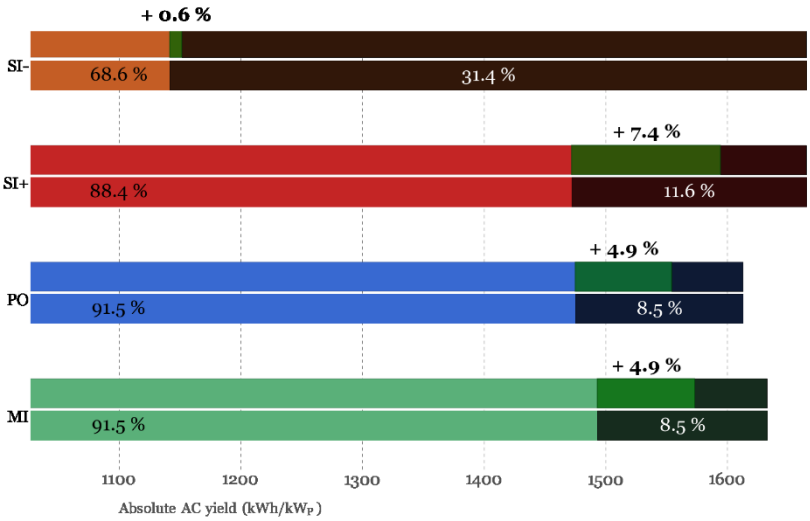


*Figure 4.3c: TMY AC yield, shading index values and potential benefits when increasing the amount of BPDs per module from 3 to 60 for string inverter with inactive (SI-) and active shadow function (SI+), power optimizer (PO) and micro-inverter (MI) system architectures in Madrid. Figure 4.1d shows the legend.*

The trends just mentioned can be explained by the fact that Madrid has a relatively dry and sunny climate compared to the other locations assumed in this research. Consequently, the simulated PV systems will experience partial shading conditions on a more frequent basis. This contrasts with clouded conditions in which the entire system faces diffuse irradiance instead of partial shading.

Strongly similar to the Reykjavik case and the Eindhoven simulation runs, the MI system output exceeds those of the other system architectures when the amount of BPDs is 3 or 6. The PO system outperforms the SI system in the reference 3 BPD case here. This is also seen for the results of the Reykjavik simulation. In the cases of 5 or more BPDs per module, the SI system with active shadow function shows the highest system yield figures again. Also see Figure 4.3d.

The shade-loss mitigation factor values are comparable to all other main and sensitivity cases taken into account. However, the numbers presented for Madrid are slightly higher than reported in the aforementioned cases because of the relatively dry and sunny climate. The SMF values now reach up to a range of 55 % to 65 % if respectively 30 or 60 BPDs per module are applied.

Table 4.3.2 – Madrid per-system shade loss mitigation factor values for each BPD case

| System | Ref. of 3 BPDs | 5 BPDs (V) | 6 BPDs | 10 BPDs (V) | 12 BPDs | 30 BPDs | 60 BPDs |
|---|---|---|---|---|---|---|---|
| SI - | - | 1 % | 0 % | 1 % | 1 % | 2 % | 2 % |
| SI + | - | 31 % | 12 % | 38 % | 43 % | 59 % | 63 % |
| PO | - | 24 % | 8 % | 30 % | 34 % | 52 % | 57 % |
| MI | - | 24 % | 8 % | 31 % | 35 % | 52 % | 57 % |

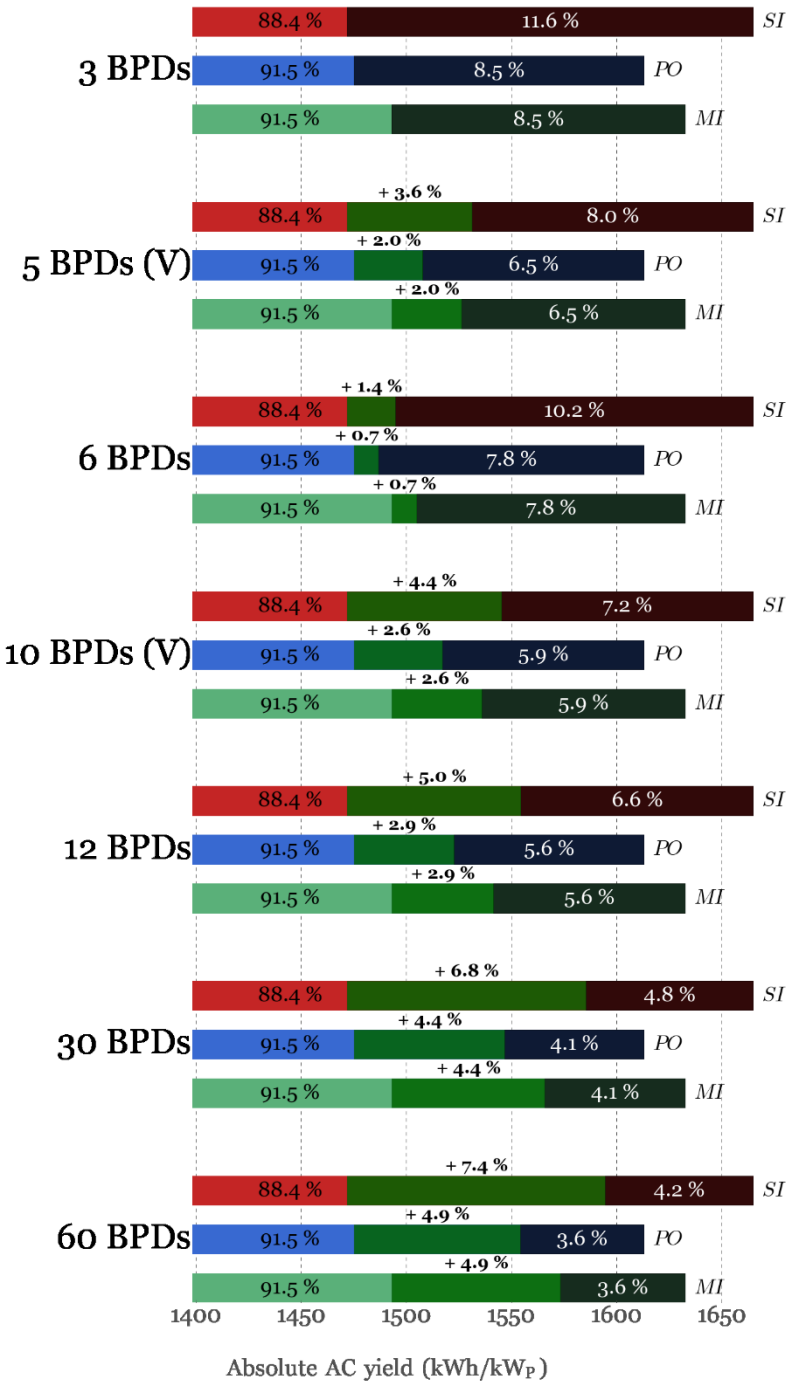


*Figure 4.3d: TMY AC yield results for SI(+), PO and MI systems placed in Madrid. Shading index values and potential benefits when increasing the amount of BPDs per module in a stepwise fashion from 3 to 60 are illustrated. The accompanying legend is shown in Figure 4.1d.*

## 4.4 – Specific yield results overview

In this paragraph a summary of the yield results of the general and sensitivity simulation runs is provided. This holds both for the orientation (Figure 4.4a) and geographic location (Figure 4.4b) sensitivity cases. The figures presented here express the specific yield and the potential benefits in kWh/$kW_p$ instead of percentages. This is done in the light of eventual future studies focusing on economic cost- and benefit-related aspects. This is because the economic value of additional energy production is determined by the absolute yield benefits in kWh. Normalization with respect to $kW_p$-values ensures insensitivity of these results with regard to PV system size.

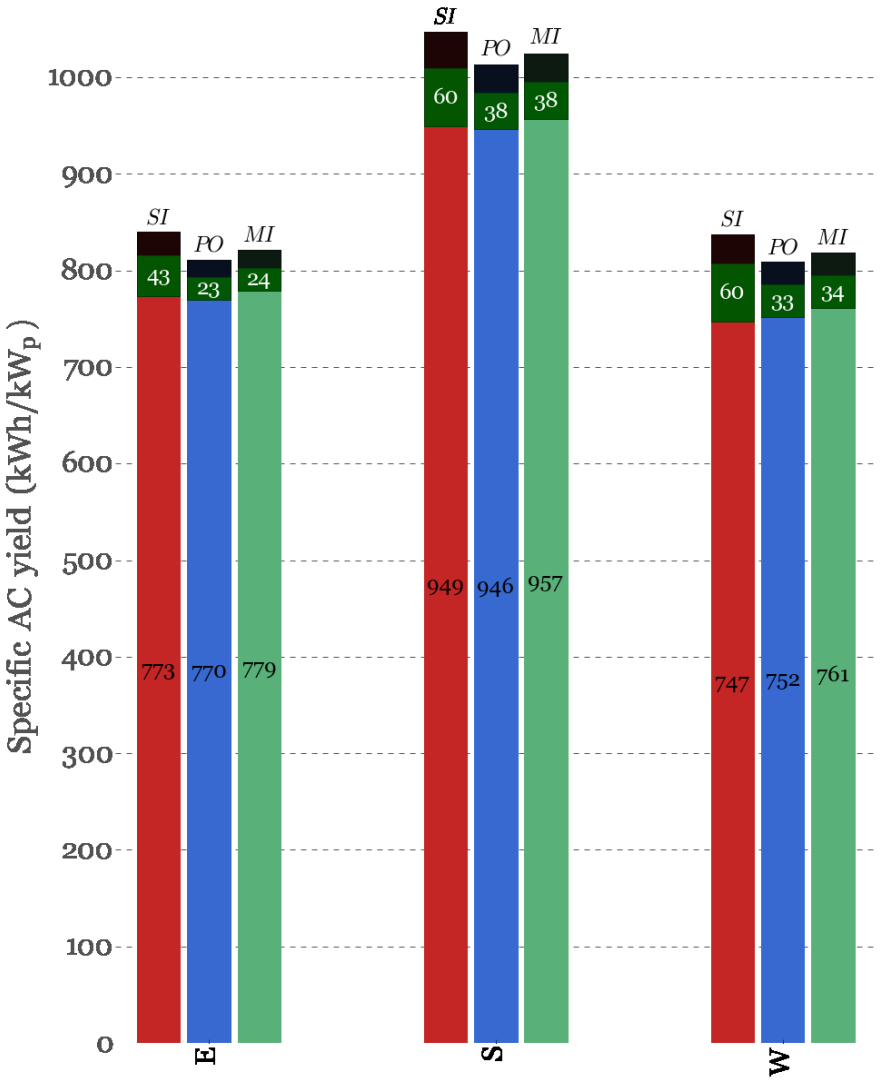


*Figure 4.4a: Specific AC yield results for SI(+), PO and MI systems placed on east (E), south (S) and west (W) oriented roofs in Eindhoven. The red, blue and light-green bars and the corresponding black text indicate the 3-BPD reference specific AC yield in kWh/$kW_p$. The dark green bars and the corresponding white text indicate the potential benefits in kWh/$kW_p$ if 60 BPDs per module are used instead of three.*

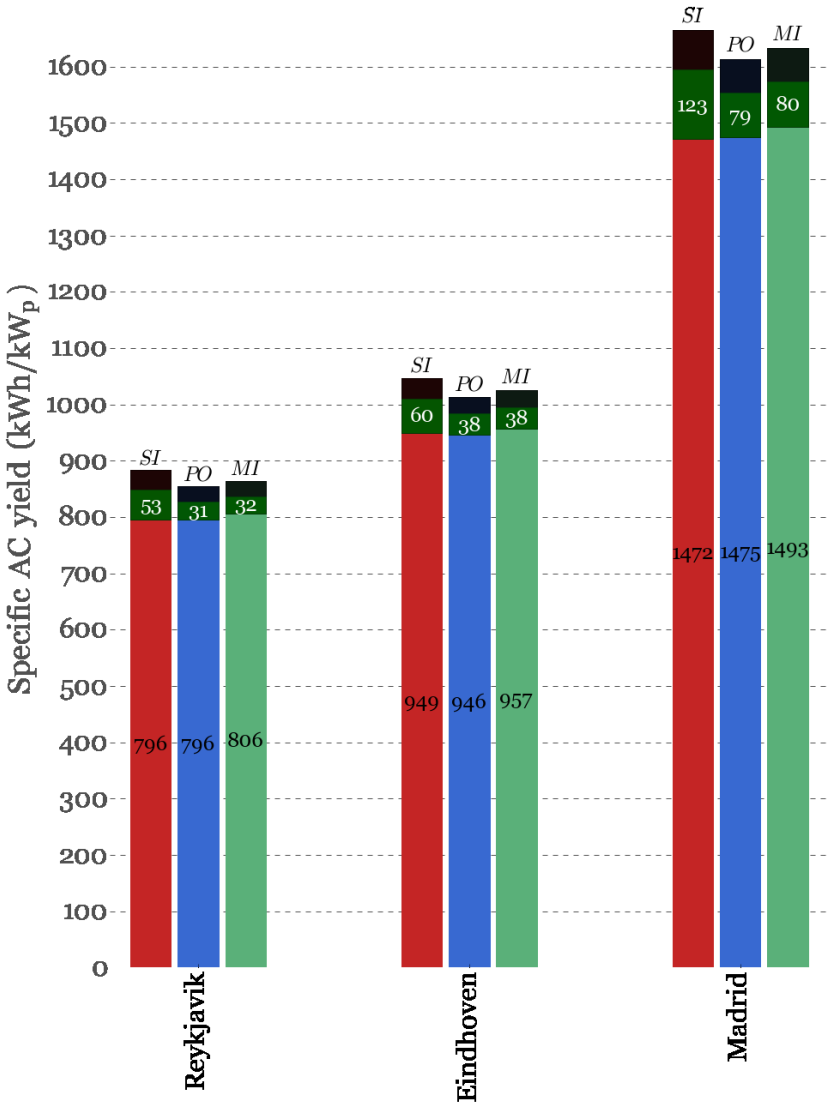


*Figure 4.4b: Specific AC yield results for SI(+), PO and MI systems placed in Reykjavik, Eindhoven and Madrid. The red, blue and light-green bars and the corresponding black text indicate the 3-BPD reference specific AC yield in kWh/kW$_p$. The dark green bars and the corresponding white text indicate the potential benefits in kWh/kW$_p$ if 60 BPDs per module are used instead of three.*

## 4.5 – Model validation results

The updated yield model presented here shows satisfactory matches with the simulation results of the former version (Sinapis, et al., in press). Deviations of 0.22% to 0.57% relative to the former yield model are found. These modest error margins can partially be explained by the use of a different IAM model. However, due to mid-day deviations, the micro-inverter DC-to-AC power loss interpolation approach (section 3.7.3) is thought to be the main reason. This causes the updated model to approximate the measured values slightly more accurately under the same assumptions.

Deviations relative to the measured data are substantially more pronounced: 5.2% to 9.4%. This is partly caused by cable and cabinet losses, anisotropic reflection effects caused by the proximate white wall and by irregularity in the position of the poles. However, MPP mismatch effects are suspected to be the major cause. In reality the MPP is scanned for on a five-minute basis, whereas both models assume perfect MPP tracking of the micro-inverter systems. This could explain that the highest upward error margins are seen for a partly clouded day. On these days MPP shifts are most frequent and most pronounced. Refer to Annex L for accompanying graphs and tables.

# Chapter 5: Discussion

This chapter is set up to provide an assessment of the methodological (§ 5.1) and results-related (§ 5.2) robustness of this research. Wherever possible, links are made to the specific parts where simplifications and weak spots apply to. § 5.3 briefly touches upon the implications of this work.

## 5.1 – Methodological approach

*Model transparency*
The use of explicit equations throughout the physical-principle-based energy model used in Python allows for a very transparent analysis of the robustness of individual model parts. Besides, the methodology regarding the imported TMY data from Meteonorm is very clearly documented as well (Meteonorm, 2015).

*BPD ideality assumption*
One of the most crucial simplifications within this research is the absence of losses associated with the implementation and operation of BPDs inside the PV systems. In reality the insertion of each additional BPD will cause current leakages in the order of micro-amps. Similarly, the activation of each BPD will lead to a voltage drop of around 40 mV (Pannebakker, 2014). These effects are generally negligible from the PV system level. However, these will definitely cause slight overestimations of the potential benefits that can actually be obtained using BPDs. This is particularly so for the 30 and 60 per-module BPD cases, since more BPDs implies more losses. This is why the yield benefit figures reported in this study are always referred to as *potential* benefits. The reported potential benefits of applying 60 BPDs per module compared to inserting 30 BPDs per module are relatively modest. Therefore it may in reality be the case that the application of 30 BPDs is energetically more favorable than applying 60 BPDs per module. The underlying reason is the loss effect of the currently available smart bypass diode technologies.

Another issue is the stability and degeneration rate of the BPDs. In reality most of the BPDs will experience significant amounts of on-off cycles during partial shading. How this affects the life expectancy of the PV system is an advised topic of consideration for future studies.

*Inter-module mismatch losses*
As initially mentioned in §1.2, PV module manufacturers bin modules within a nominal capacity range of $5W_p$ tor $10W_p$. This means that PV modules classified within the same rated power category will in reality have slight offsets in power generation under the same conditions. In this study each module's output is set fixed at 263.0 W (Table 3.5.1). Therefore no inter-module mismatches due to varying nominal power capacities occur in the PV systems studied here. Consequently, the yield figures of the string inverter-based system architectures in this study are slightly overestimated. This means that the PO and MI systems will in reality perform slightly better compared to the SI systems. This is because the former system architectures track the MPP per module. Therefore they are insensitive to inter-module mismatch losses, contrary to the SI.

*SketchUp model + sensitivity analysis*
Overall the considered shade scenarios and roof specifications have a very specific nature despite being chosen as relatively representative averages. However, the conclusions derived in this work can be applied to conditions outside the strict scope of this research. The underlying reason is the overall insensitivity of the general trends of the obtained results with respect to roof orientation

and geographical location. The high-end-estimate dormer dimensions chosen in this research also seem justifiable for this reason.

The use of east and west (and south-east and south-west) roof orientations as a complete and representative framework for the roof orientation sensitivity analysis is justifiable as well. This is due to the similarity of trends for system-level shading index values, potential BPD yield benefits and shade mitigation factors throughout all orientation sensitivity simulation results.

Note that no sensitivity analysis with respect to the roof tilt is conducted in this study. However, a straightforward relation between roof tilt and partial shading effects can be drawn based on the model understanding gained so far. A lower tilt angle represents flatter roofs while the shading objects remain fixed in size and position. This leads to the expectation of more intense partial shading effects than those reported in this work. Inversely the effects of partial shading are expected to be less pronounced than reported here if the roof is tilted more heavily.

*Irradiance reflection effects*

Another point of discussion is that the incident angle modifier fraction equations and the IV model do not include spectral loss effects. All irradiance values used in this study assume a spectral distribution matching STC conditions with an air mass ratio of 1.5. This does not hold on hazy days and at low solar elevation angles around sunrise and sunset. However, these type of conditions only marginally contribute to the total annual incident solar energy. Therefore they are not expected to lead to significant errors in the presented annual TMY yield figures. This is underlined by c-Si annual spectral loss figures that were found to lie in the range of 0.27% to 0.57% depending on local conditions (Litjens, 2013).

An albedo reflection factor ($\rho_A$) of 0.15 is chosen within this research. This matches the lower range of albedo estimates related to grass and the urban environment (PVPMC/Sandia, 2014c). Conventionally albedo reflection values of 0.20 are used in PV modeling studies. These align with the average range of albedo estimations related to the urban environment (PVPMC/Sandia, 2014c). The reason that the albedo reflection factor is limited to 0.15 here is to reduce the chance of obtaining overrepresentations of PV yield performances. This is in line with the convention used in preceding work (Sinapis, et al., in press).

Moreover, the albedo reflection effect is assumed homogeneous throughout the field. In reality this effect is expected to be heterogeneous to some degree. Particularly the parts of the system located near the central dormer are likely to face additional irradiation caused by reflection on sunny days. This is expected to intensify mismatch effects within substrings, modules and the PV systems as a whole. This phenomenon was observed in the MLPM PV test field in preceding work (Sinapis, et al., in press). Due to the proximity of a white wall to some of the modules in the PV systems studied there, reflection on sunny days caused up to 4% higher yield in the wall-neighboring modules compared to those located far away from the wall. Inversely, up to 4% lower system output was found due to obstruction of diffuse light by the wall on cloudy days. Unfortunately such effects are extremely difficult to model and can only be assessed in detail by benchmarking with respect to real-life conditions. As this study's roof does not have a real-life equivalent to compare with, these advanced reflection effects are not considered here. For those particularly interested in modeling PV system components on tilted planes including reflection effects, modeling procedures on this topic are listed by Gulin, Vašak & Baotić (2013).

Besides MPP mismatch effects, possible overestimation of the albedo reflection effect could also be a cause for the yield overrepresentations reported in the validation procedure (§ 4.5).

*Temperature effects*
The heat transfer component values $U_0$ and $U_1$ used in the Faiman temperature model (Faiman, 2008) were originally determined for ground-mounted PV systems rather than for roof-attached PV systems. It is expected that these values vary between the two situations due to different heat flow dynamics. Air is able to access the bottom part of modules in ground-mounted systems. However, air access to the module bottom parts is restricted in the roof-attached case. This makes it very likely that the substring temperatures calculated in the energy yield model are underestimated. As a result the temperature-related PV cell losses within the utilized energy yield model have a likelihood of being underestimated.

Another used approximation is that the substring temperature is assumed to be homogeneous over the cells in the substring. Furthermore it is set independent of the other substring temperatures within the module. In reality this does not hold entirely. Component temperature differences up to 10 °C were encountered in a PV system sized similarly to the one studied here (Benda, Machachek, & Stanek, n.d.). For improvement purposes, Olukan & Emziane (2014) proposed a more detailed temperature model based on a finite-element method, although an explicit methodology was not yet provided. Likewise, Ciulla, Lo Brano, Franzitta & Trapanese (2014) extended the Faiman temperature model with an MPP-proximity term. The underlying aim was to improve the procedure of fitting the temperature values to real measured data. However, this extension requires full knowledge of the system MPP voltage and operating voltage within each component of the PV system. This necessitates obtaining real-life measured data of the PV systems of interest. This has not been possible in this research due to the absence of a real-life test field set-up for the PV systems studied in this work.

*Soiling effects*
The effect of grind, dust and other materials gradually being deposited on PV modules, thereby reducing their performance, is referred to as soiling. This effect decreases rapidly when module surface tilt angles are increased. Even in the relatively dry climate of Arizona, US, the energy yield losses related to soiling at a 40° tilt angle were found to be only 0.69% (Cano, 2011). As rain will wash away accumulated grind and dust particles on a frequent basis in climates characterized by higher levels of precipitation, this effect is even less significant for the geographic locations assumed in this study. This justifies leaving soiling effects outside the scope of consideration here.

*IV curve simplifications*
The constant diode ideality factors assumed in the IV modeling procedure vary in reality due to a wide range of variables and occurring mechanisms within a specific solar module (Honsberg & Bowden, n.d. - a). Also the two diode saturation current values used here are assumed to be equal, while these typically differ several orders of magnitude (Honsberg & Bowden, n.d. - b). Despite being simplifications, the exclusions mentioned here only reflect on secondary effects taking place within a module. Therefore the resulting degree of uncertainty in the IV curves will be modest.

Another important assumption is that the panel-level series resistance is considered to be constant over different values for temperature and irradiance. The shunt resistance is scaled linearly inversely with respect to the effective irradiance (Table 3.5.1). Both these assumptions are simplifications and lead to a maximum power error ($\varepsilon_P$) of 0.35% at STC[15]. Furthermore, resistance sensitivity model test runs[16] indicate an error uncertainty up to a range of 2% to 3% at

[15] This percentage value is determined by comparing the model MPP at STC to the maximum rated power value reported on the module manufacturer's datasheet.
[16] These test runs encompass a straightforward comparison of the difference in modeled power output for the chosen pair of resistance values (Table 3.5.1) and a pair of resistance values yielding an STC MPP error of 0.2%.

irradiance and temperature levels significantly above STC values. However, the resistance-related power error margin falls significantly below 0.35% for model runs at low irradiance values. Overall the magnitude of the aggregate uncertainty error margins caused by the IV panel resistance simplifications seem to align with those caused by the other simplifications mentioned in this section.

In a recent paper on IV curve modeling, the following temperature-dependent relations for the diode ideality factors $n_i$, the series resistance $R_s$ and the shunt resistance $R_{sh}$ were proposed (Barth, Jovanovic, Ahzi, & Khaleel, 2015):

$$n_i(T) = n_{i,STC} \cdot (T/T_{STC})^{a_i} \quad (5.1)$$

$$R_s(T) = R_{s,STC} \cdot exp(B_s \cdot (T - T_{STC})) \quad (5.2)$$

$$R_{sh}(T) = R_{sh,STC} \cdot exp(B_{sh}/(T - T_{STC})) \quad (5.3)$$

In Equations 5.1 to 5.3, $a_i$ represents the power exponent accompanying diode ideality factor $n_i$, with $B_s$ and $B_{sh}$ as semiconductor material coefficients. These material coefficients are characterized by positive (> 0) values.

*Inter-module circuitry*
Throughout this study all modules in the considered PV systems are connected in series. This makes the PV system particularly vulnerable to partial shading losses. Belhachat & Larbes (2015) investigated the effect of partial shading conditions on various electronic system circuitries. They found that applying other circuitries can offer significant yield benefits in situations of partial shading, although the extent and optimal circuitry configuration highly depends on the applied shading scenario. It may well be that these potential advantages are similar in magnitude compared to the BPD-insertion-related benefits reported in this study. An eventual future economic assessment related to applying more BPDs inside PV systems should always take this in mind. The underlying reason is that adjusting the circuitry may turn out to be more cost-effective than applying more BPDs inside each module.

*MPP tracking*
Depending on the system architecture, either perfect global MPP tracking or "poor" local MPP tracking is assumed in this work. In reality, the IV curve of a PV system is checked every five minutes. This means that large operating voltage shifts do not occur within each five minute interval. Particularly on partly clouded days, on which the irradiance conditions and therefore the system IV curves change frequently and rapidly, this will lead to yield overestimations. This is underlined by the results related to the validation procedure (§ 4.5 and Annex L). As expected, the highest yield overestimation of the model with respect to measured yield data is reported for the partly clouded day.

*System comparison result parts*
As explained in this section, deviations mainly arise due to the reflection effects, temperature effects and the IV model simplifications. However, it is worth mentioning that all model runs are conducted under the same methodological regime except for the AC power electronics' efficiency parts. This means that the majority of the described uncertainties and errors do not affect the *relative* outcomes of the system comparison parts for the same assumed amount of BPDs.

These are found using a slightly adapted resistance-finding algorithm. The reported comparisons are made using both a high-irradiance (1500 W/m², 100 °C) and a low-irradiance (1 W/m², 0 °C) condition.

## 5.2 – Obtained results

*PV system size*
The studied PV systems consist of nine panels and have a total rated capacity of about 2.4 $kW_p$. Yield results for the south-oriented roof in Eindhoven are close to 950 $kWh/kW_p$ (Figure 4.4a). This gives an annual total of around 2275 kWh. This reflects about 75% of Dutch annual electricity consumption (CBS Statline, 2014), which seems very reasonable for a residential PV system.

*Reference BPD-case shading index values (system losses)*
Exhaust pipes cause shading index values of up to about 10% with regard to panel-wise DC output in the simulation runs undertaken here. However, significant effects are only observed for the module located most closely to the exhaust pipes of the central house roof. The effect due to the presence of chimneys is generally associated with low (< 2%) per-panel DC shading index values. However, an outlier with a SIDX of 5% is seen for the top-left module in the eastward roof case. Dormer-dominated DC panel yield losses cause relatively high per-panel DC shade indices. A range of 3.8% to 15.2% is observed in the southward roof orientation case. This range is 4.2% to 15.3% for the modules affected most significantly in the eastward roof case. For the modules that are highly affected in the westward roof orientation this is 5.9% to 20.7%. Aggregate DC losses averaged over the nine studied modules result in shading index values of 6.3%, 4.9% and 6.7% for the south, east and west roof cases respectively.

From a system perspective, the shading index effect related to dormers dominates all roof orientation simulation runs. For the southward case exhaust pipes cause only a secondary effect, with chimneys causing even less system losses. In the eastward situation the effect due to chimneys is more outspoken compared to the effect caused by exhaust pipes. The reverse is true for the westward roof orientation case.

As explained in the results chapter of this report, the system-aggregated shading index values vary on the power electronics used for the studied PV system. The studied SI system architecture with poor MPP tracking faces shading index values of 18.9% to 23.9% in the Eindhoven cases. These are 23.0% and 31.4% respectively for Reykjavik and Madrid. Comparatively, the proper MPP tracking SI system shows SIDX values in the range of 7.9% to 10.8% in Eindhoven, with 9.9% and 11.6% in Reykjavik and in Madrid. The large difference in shading index values between the two tracking types shows that poor MPP tracking can inhibit MPP mismatch losses alone being far more severe than the aggregate effect due to partial shading itself.

The PO and MI systems show virtually equal shading index values throughout all simulations due to their similarity in optimizing the power output per panel. A range of 5.1% to 7.0% is found for the Eindhoven cases, while SIDX values are 6.8% for Reykjavik and 8.5% for Madrid. Also note the similarity of the PO and MI outcomes for Eindhoven and the DC-average shading index values.

Despite observed variations of the system-level shading index values depending on roof orientation and geographic location, the SIDX values seem to be relatively steady in general. This is a consequence of the fixed distance of all PV system components to the modeled shade-casting objects. In effect this means that the dimensions of the shade objects and the distance of these objects to PV system components are more important here in explaining the overall partial shading-related system losses than the roof orientation or geographic and climatologic conditions.

Deline, Meydbray, Donovan & Forrest (2012) measured SI system losses of 6.7% to 23.5% depending on the intensity of the assumed partial shading scenario. Deline, Marion, Granata & Gonzalez (2011) found direct partial shading-induced SI system losses of 14%. An assessment of 542 monitored PV systems by Hanson, Deline, MacAlpine, Stauth & Sullivan (2014) resulted in calculated shade-induced system losses of 13% for SI systems. At the same time losses of 8.3% were measured for per-panel-optimizing MPP systems. Sinapis et al. (in press) found pole-shade-related system losses of 6.6%, 4% and 4% for the studied SI, PO and MI systems respectively. These figures all align with the shading index values for the system architectures reported in this research to a satisfactory degree. Yield benefits of 3.7% to 12.3% by switching from a SI to a MI system architecture were shown as well while the reference amount of 3 BPDs per module was kept constant (Deline, Meydbray, Donovan, & Forrest, 2012). Particularly the reported upper benefit range significantly exceeds the MI benefits relative to SI(+) systems calculated in this study. This is due to the use of real measured data causing the SI to face MPP mismatch losses in real conditions. As explained earlier, the work presented here only analyzes the two most extreme MPP tracking cases for the SI systems.

*Potential benefits of additional BPD insertion*
In this research the average DC-average potential benefits for the Eindhoven simulations found are 1.1% to 1.6% for the 5 BPDs case, 0.3% to 0.5% for the 6 BPDs case, 1.5% to 2.2% for the 10 BPDs case, 1.5% to 2.2% for the 12 BPDs case, 2.4% to 3.5% for the 30 BPDs case and 2.7% to 3.9% for the case of 60 BPDs per module.

The SI system architecture with poor MPP tracking barely benefits from inserting additional BPDs in the module. The maximum reported benefits are well below 1% for the 60 BPDs case while the shade-induced losses are much higher than for the effective MPP tracking systems to start with. This implies that effective MPP tracking in PV systems must be ensured before considering the application of increased amounts of BPDs inside each module.

The AC system potential benefit ranges for the efficient MPP tracking systems reported in this research are as follows. For the SI system, 2.6% to 3.6% in the 5 BPDs case, 0.7% to 1.4% in the 6 BPDs case, 3.3% to 4.4% in the 10 BPDs case, 3.3% to 5.0% in the 12 BPDs case, 4.7% to 6.8% in the 30 BPDs case and 5.1% to 7.4% in the case of 60 BPDs per module. Potential benefit ranges are equal for the PO and MI systems: 1.2% to 2.0% in the 5 BPDs case, 0.3% to 0.7% in the 6 BPDs case, 1.6% to 2.6% in the 10 BPDs case, 1.6% to 2.9% in the 12 BPDs case, 2.6% to 4.4% in the 30 BPDs case and 2.9% to 4.9% in the case of 60 BPDs per module.

It is clearly observable that increasing the amount of BPDs effectuates higher potential benefits except for the 6 BPDs case versus the 5 BPDs case. As explained in the results chapter, this has to do with the nature of the orientation of the dormer-casted shade shapes relative to the cell alignment within the modules. Another trend is that the potential benefits tend to level off at high BPD amounts per module. This is because casted shade shapes always cover fixed fractions of module surfaces in partial shading conditions. While increasing the amount of BPDs greatly increases the surface fraction that can be used effectively at the first insertion steps, this effect levels off at higher amounts of inserted BPDs. The reason for this is because the optimal effective module surface area is rapidly approximated at moderate amounts of BPDs.

The potential benefits associated with applying per-cell BPDs the effective MPP tracking SI system of 5.1% to 7.4% reported here are slightly higher than the range of 3.3% to 5.9% calculated in a similar scientific study (MacAlpine, Brandemühl, & Erickson, 2011). Besides the use of different tilt angles, climatologic conditions and shading scenarios, the difference is most likely caused by

the assumption of a shade-sensitive full series connection between modules here. In contrast, the referenced work studied a system composed of two strings of modules connected in parallel.

Note that throughout this study high potential benefits strongly correlate with high SIDX values. This is underlined by the constant nature of the SMF values as outlined below. Also see Figure 4.a.

*Shade Mitigation Factors*
Note that the shade mitigation factors (SMFs) are another way of expressing the potential benefits (PB). The main difference is that the PB is normalized relative to the total specific yield while SMFs are normalized with respect to the shade-related yield losses (also see Equations 3.13 and 3.14 and Figure 4.a). As the SMF values for the poor MPP tracking SI system architecture are very small for the same reason as for the potential benefits, the scope of interest here only includes the effective MPP tracking condition of the SI system.

The range of values found for the SMF throughout this study are 28% to 31% for the 5 BPDs case, 9% to 12% for the 6 BPDs case, 35% to 42% for the 10 BPDs case, 40% to 43% for the 12 BPDs case, 57% to 61% for the 30 BPDs case and 61% to 66% for the case including 60 BPDs per module. Again the results for the PO and MI systems are virtually equal. Their SMFs fall in the range of 20% to 24% for the 5 BPDs case, 7% to 8% for the 6 BPDs case, 27% to 33% for the 10 BPDs case, 30% to 35% for the 12 BPDs case, 48% to 52% for the 30 BPDs case and 54% to 59% in the case assuming 60 BPDs in each module. These mentioned ranges include all sensitivity simulation runs for roof orientation and geographic location.

In other words, the SMF values per BPD case are remarkably consistent throughout all sensitivity cases. Much more so than the results for the shading index and the potential benefits. This is seen as remarkable because the surface-wise extent of the shading shapes varies throughout all sensitivity cases. Therefore this cannot explain the observed SMF similarities. A possible explanation for the SMF consistency is the fixed nature of the geometric shapes of the shades casted in the TMY simulations. The modeled dormers always cast shades that are approximately triangular while the chimneys produce parallelogram-shaped projections. Similarly the exhaust pipes cause icosagonal projections on shaded module surfaces. Regardless of the scale of partial shading, the fixed substring shape and orientation in each considered BPD cases can be expected to lead to bypassing behavior. This, in turn, causes additional surface proportions of a module surface to be bypassed in relatively fixed amounts in these situations.

The SMF trends related to stepwise BPD insertion and the causes of these trends are analogous to the trends reported for the potential benefits.

*Validation procedure*
In general the validation procedure corresponds to the results obtained for the previous energy yield model to a high degree. Note that the updates mainly encompass enhanced flexibility on the amount of BPDs, a more general shade modelling procedure and a more general IV curve algorithm. Therefore it is expected that the deviations with respect to the previous yield model are small for the validation cases considered. However, both models significantly overestimate the measured system yield. For reasons outlined before, the suspicion is that this is caused by secondary effects (§ 4.5) and MPP tracking imperfections. Simulating these imperfections requires knowledge of the MPP tracking algorithms used in the system architecture devices. Unfortunately these have not been available. As stated before in this chapter, a potential overestimation of the albedo reflection effects could be another contributing factor.

## 5.3 – Implications

Besides for justification reasons, the discussion of the methodology outlined in § 5.1 is aimed to stimulate additional future improvements of the energy yield model. This particularly holds for the IV curve modeling procedure part. As is also mentioned in § 5.1, another key future improvement encompasses the introduction of BPD-insertion-related voltage drops and current leakage values in the substring IV curves.

The sensibility of the results obtained in this work are underlined by similar results obtained by other contributions within the field of partial shading of PV systems. At the same time the results deviating from the trends observed in this research can be logically explained in all instances.

Overall the updated energy yield model used for the simulations within this work can be used to model the behavior of PV systems with non-reference amounts of BPDs per module. Also the shading model presented here is made flexible in order to allow this model part to be used in future solar energy monitoring projects with only minor adaptations required. Other such an assessment includes the option of tracking how many BPDs within the system are activated at certain times. Another possibility is to model the behavior and the yield potential of PV systems utilizing per-substring to per-cell micro-inverters or power optimizers as shade-mitigating applications.

The potential yield benefits presented in this research provide a solid starting point for an economic follow-up study. Based on energy yield figures alone one cannot be able to assess the optimal amount of BPDs to be implemented in PV systems in any specific circumstances. This is because any additional economic costs that arise from applying shade-mitigating technologies must be counterbalanced by proportional amounts of added economic value. This added value is associated with the achieved gains in energy yield.

One of the most important results emerging from this work is the constant nature of the SMF values throughout all sensitivity simulation runs. Around 60% of the energy initially lost due to shading in the reference case is found to be retrievable when switching to 60 BPDs per module. This consistency is a strong indication for scale-independent behavior of the SMF under partial shading conditions. Therefore it is strongly suspected that fixed relative fractions of the shade-related losses can be recovered for any level of relative partial shading losses encountered. This could imply that the absolute potential yield benefits of increased BPD insertion increase linearly with the yield lost due to partial shading. Consequently, promising absolute yield benefits could be accomplished in PV systems with high initial levels of partial shade-induced yield losses.

In general, the encountered SMF consistency also means that increasing the amount of by-pass diodes could give way to PV system efficiency improvements in a wide range of partial shading conditions. This means that a potentially widespread sales market for PV systems containing high amounts of by-pass diodes could develop in the future. However, more research is required prior to such developments. Firstly, long-term stability and low degeneration rates of smart BPDs applied in PV systems have to be demonstrated. The number of on-off cycles of BPDs during partial shading is expected to increase at each incremental by-passing flexibility improvement. This is thought to affect the lifetime of the BPDs and the overall stability of each PV module of interest. Secondly, the economic benefits of increased PV system energy output related to by-pass diode insertion must be proven to outweigh the associated implementation costs.

# Chapter 6: Conclusions

The research presented in this report is set up to assess the effect of increasing the amount of (smart) by-pass diodes (BPDs) on the annual energy yield in (c-Si) residential-scale PV systems facing conditions of partial shading. A physical-principle-based energy yield model is used, extended and updated as a part of this work. This model derives the shaded fraction of each cell within the PV system under partial shading conditions, calculates the electric response and aggregates these electric responses over time to determine the yield of a PV system of interest.

An average Dutch roof with representative dimensions, shade-casting objects and fixed tilt angle is determined. Initially a south-facing roof is chosen for yield optimality purposes. The roof is tilted 40°. Furthermore, a single chimney, two exhaust pipes and a large dormer have been placed on each rooftop in the row of houses. These objects create partial shading conditions on the PV system located on the most central house roof. This system consists of nine c-Si Yingli Panda 265 $W_p$ modules connected in a string (series) configuration.

TMY energy yield simulations are performed for string-inverter- (SI), power optimizer- (PO) and micro-inverter-based (MI) PV systems in Eindhoven, The Netherlands. Shade-induced yield losses are respectively 9.3%, 6.6% and 6.6% for effective MPP-tracking SI, PO and MI architectures in the reference case of 3 BPDs per module. Up to 62% (SI) and 56% (PO & MI) of the total yield lost due to shading can be recovered by switching the amount of BPDs to 60 per module. The MI is the optimal configuration at the reference case whereas the SI configuration is optimal at non-reference BPD amounts. This is caused by beneficial SI conversion efficiencies. Very high shade-related yield losses of 24% are reported for the poor MPP-tracking SI configuration. Of these losses only a fraction of 3% can be recovered in the 60 BPDs case. This stresses the necessity of implementing effective MPP tracking before considering application of more BPDs in PV modules.

Overall the roof orientation sensitivity simulation runs give results strikingly similar to those obtained for the south-facing roof. The system-level effects of the dormers consistently dominate the contribution to shade-related energy yield losses. Only the contribution of individual shade-generating objects on individual panels changes significantly if the rooftop orientation is changed. Nevertheless, this effect levels out for the system as a whole. The same similarities are found for the geographic location sensitivity simulations for south-faced roofs in Reykjavik and Madrid. Overall the partial shading effects are slightly more pronounced in Madrid due to the significantly sunnier climate. As expected, the specific system yield figures ($kWh/kW_p$) vary considerably among the performed simulation runs. However, the recoverable fraction of shade-induced energy losses shows remarkable consistency for all BPD-amount cases in all sensitivity runs. This latter fact may lead to promising absolute yield benefits in PV systems with high initial levels of partial shade-induced yield losses. Another promising implication could be the development of a widespread sales market for PV systems incorporating high numbers of BPDs. However, more research on the stability, safety and degradation issues is required on one hand. On the other hand, the economic benefits of BPD insertion must be proven to outweigh the implementation costs.

Strong points of the used modeling approach include a high degree of transparency and the flexibility of changing the shading regimes, roof orientation and geographic location while keeping all other factors constant. This allows for a high-detail discussion of the methodological assumptions and a clearly defined sensitivity analysis. Furthermore, successful validation of the model with respect to the yield model used in previous work underlines the used approach. Weak model points encompass the assumption of extreme MPP mismatch conditions for the SI system, the absence of inter-module mismatch effects and the ideality assumptions made for the BPDs. However, most of these points can be overcome with modest future yield model adaptations.

# Chapter 7: Recommendations

Based on the work done related to this research, several recommendations for future studies and future energy yield model developments are presented here.

As becomes clear in the discussion and conclusion chapters, a recommendatory next step related to the energy yield model used for this study is to move away from the ideal BPD assumption. This may significantly affect the potential benefit outcomes for the various BPD-amount-cases taken into account here, most of all those incorporating high amounts of by-pass diodes per module (the 30- and 60-cases). For this purpose, BPD insertion and operation losses are to be included in future updates of the energy yield model referred to.

Another proposed energy yield model update entails the reduction of the amount of assumptions and simplifications in the IV curve modeling procedure. This refers in particular to the simplifications and assumptions related to the series and shunt resistances, the diode ideality factors and the diode saturation currents as discussed in §5.1 of this report. The literature outlined there could provide a useful starting point for such a procedure.

The shade mitigation factors reported in this work are surprisingly insensitive to variations in roof orientation and geographic location. However, the question whether this relation also actually holds for systems facing very high levels of partial shading[17] remains unanswered. Specified case studies are recommended in other to prove or disprove the hypothesis related to promising linear power recovery potential figures associated with additional BPD insertion in situations of intense partial shading.

It may prove to be worthwhile to implement an experimental set-up that shows the benefits of applying high amounts of BPDs inside PV systems in real operating conditions, since simulations can only address the MPP and inter-module mismatch effects occurring in PV system architectures to a limited degree. Experimental measurements could be combined with a comprehensive and detailed modeling approach in order to combine the flexibility advantages of a modeling procedure with the advantages of encountering real-life conditions and effects in the field. A simulation assessment related to the amount of activated BPDs and their times of operation throughout a typical year could also encompass an insight-generating future research topic.

Another logical follow-up path would encompass a detailed economic assessment related to BPD insertion in string-inverter, power optimizer and micro-inverter PV system architectures. As it makes most sense to also include the opportunity cost of applying more BPDs in PV modules with respect to other shade-mitigating application options, such a study is advised to also consider the economic costs and benefits related to applying per-substring or per-cell power optimizers or micro-inverters. On top of that, the referred future study should also take the economics related to adaptations of wire circuitries within PV systems of interest into account. As mentioned in the Discussion and Conclusion chapters, the described economic study could provide an initial indication for the potential development of a wide-spread sales market for PV systems containing high BPD insertion degrees. However, another type of future study is required as well. That type of research should be set out to address the issues of BPD stability, safety and degradation rates in PV systems with high degrees of BPD insertion.

[17] For instance, partial shade conditions resulting in 30% PV system yield losses over a year.

# Bibliography


Adamo, F., Attivissimo, F., Di Nisio, A., & Spadavecchia, M. (2011). Characterization and Testing of a Tool for Photovoltaic Panel Modeling. *IEEE Transactions on Instrumentation and Measurement, 60*(5), 1613-1622.

Agentschap NL. (2013). *Referentiewoningen nieuwbouw 2013.* Sittard, The Netherlands: Agentschap NL.

Al-Hajri, M. F., El-Naggar, K. M., Al-Rashidi, M. R., & Al-Othman, A. K. (2012). Optimal extraction of solar cell parameters using pattern search. *Renewable Energy, 44*, 238-245.

Angus, R., & Muneer, T. (1993). Sun position for daylight models: Precise algoritms for determination. *Lighting Research and Technology, 25*(2), 81-83.

Barth, N., Jovanovic, R., Ahzi, S., & Khaleel, M. (2015). PV panel single and double diode models: Optimization of the parameters and temperature dependence. *Solar Energy Materials & Solar Cells*, in press. doi:10.1016/j.solmat.2015.09.003i

Batzelis, E. I., Georgilakis, P. S., & Papathanassiou, S. A. (2015). Energy models for photovoltaic systems under partial shading conditions: a comprehensive review. *IET Renewable Power Generation, 9*(4), 340-349.

Belhachat, F., & Larbes, C. (2015). Modeling, analysis and comparison of solar photovoltaic array configurations under partial shading conditions. *Solar Energy, 120*, 399-418. doi:10.1016/j.solener.2015.07.039

Benda, V., Machachek, Z., & Stanek, K. (n.d.). *Non-Uniform Temperature Distribution on a Photovoltaic Field under Real Operating Conditions.* Prague: Czech Technical University.

Bendib, B., Belmili, H., & Krim, F. (2015). A survey of the most used MPPT methods: Conventional and advanced algorithms applied for photovoltaic systems. *Renewable and Sustainable Energy Reviews, 45*, 637-648. doi:10.1016/j.rser.2015.02.009

Boas, M. (2006). *Mathematical Methods in the Physical Sciences* (3rd ed.). Wiley.

Cano, J. (2011). *Effect of tilt angle on soiling (Doctoral dissertation).* Mesa: Arizona State University.

Carrero, C., Rodriguez, J., Ramirez, D., & Platero, C. (2010). Simple estimation of PV modules loss resistances for low error modelling. *Renewable Energy, 35*, 1103-1108.

CBS Statline. (2014). *Energieverbruik particuliere woningen; woningtype en regio's*. Retrieved April 17, 2016, from CBS Statline: http://statline.cbs.nl/StatWeb/publication/?DM=SLNL&PA=81528NED

Ciulla, G., Lo Brano, V., Franzitta, V., & Trapanese, M. (2014). Assessment of the Operating Temperature of Crystalline PV Modules Based on Real Use Conditions. *International Journal of Photoenergy, Article ID 718315*, 11 pages. doi:10.1155/2014/718315

Cotfas, D. T., Cotfas, P. A., & Kaplanis, S. (2013). Methods to determine the dc parameters of solar cells: A critical review. *Renewable and Sustainable Energy Reviews, 28*, 588-596.

De Soto, W., Klein, A., & Beckman, W. A. (2006). Improvement and validation of a model for photovoltaic array performance. *Solar Energy, 80*(1), 78-88.

Deline, C. (2010). *Characterizing Shading Losses on Partially Shaded PV Systems - PV Performance Modeling Workshop.* Albuquerque, New Mexico, US: National Renewable Energy Laboratory.

Deline, C., Dobos, A., Janzou, S., Meydbrey, J., & Donovan, M. (2013). *A simplified model of uniform shading in large photovoltaic arrays.* United States: National Renewable Energy Laboratory.

Deline, C., Marion, B., Granata, J., & Gonzalez, S. (2011). *A Performance and Economic Analysis of Distributed Power Electronics in Photovoltaic Systems.* Golden, Colorado (US): NREL.

Deline, C., Meydbray, J., Donovan, M., & Forrest, J. (2012). *Photovoltaic Shading Testbed for Module-Level Power Electronics.* Golden, Colorado: National Renewable Energy Laboratory.

Dutch Ministry of Home Affairs. (2015). *Dakkappellen - Wanneer vergunningsvrij, wanneer omgevingsvergunning nodig?* The Hague: Dutch Ministry of Home Affairs.

EEA. (2008). *Air pollution from electricity-generating large combustion plants.* Copenhagen: European Environment Agency.

EnecSys. (2015a). *EnecSys - WP Content - Uploads*. Retrieved November 23, 2015, from EnecSys Web site: www.enecsys.com/wp-content/uploads/Figure2.jpg

EnecSys. (2015b). *EnecSys - WP Content - Uploads*. Retrieved November 23, 2015, from EnecSys Web site: www.enecsys.com/wp-content/uploads/Figure3.gif

EPIA. (2014). *Global Market Outlook for Photovoltaics 2014-2018.* Brussels: European Photovoltaic Industry Association.

Faiman. (2008). Assessing the outdoor operating temperature of photovoltaic modules. *Progress in Photovoltaics, 16*(4), 307-315.

Graham, R. L. (1972). An Efficient Algorithm for Determining the Convex Hull of a Finite Planar Set. *Information Processing Letters, 1*, 132-133.

Gulin, M., Vašak, M., & Baotic, M. (2013). Estimation of the global solar irradiance on tilted surfaces. *7th International Conference on Electrical Drives and Power Electronics (EDPE 2013)* (pp. 334-339). University of Zagreb.

Hanson, A., Deline, C., MacAlpine, S., Stauth, J., & Sullivan, C. (2014). Partial-Shading Assessment of Photovoltaic Installations via Module-Level Monitoring. *IEEE Journal of Photovoltaics, 4*(6), 1618-1624. doi:10.1109/JPHOTOV.2014.2351623

Hasyim, E. S., Wenham, S. R., & Green, M. A. (1986). Shadow tolerance of modules incorporating integral bypass diode solar cells. *Solar Cells, 19*, 109-122.

Honsberg, C., & Bowden, S. (n.d. - a). *Solar Cell Operation - Ideality Factor*. Retrieved March 31, 2016, from PV Education Web site: http://www.pveducation.org/pvcdrom/solar-cell-operation/ideality-factor

Honsberg, C., & Bowden, S. (n.d. - b). *Measuring Ideality Factor*. Retrieved March 31, 2016, from PV Education Web site: http://www.pveducation.org/pvcdrom/characterisation/measurement-of-ideality-factor

IEA, NEA & OECD. (2015). *Projected Costs of Generating Electricity.* Paris/Issy-les-Moulineaux: International Energy Agency & Nuclear Energy Agency.

Ishaque, K., & Salam, Z. (2011). A comprehensive MATLAB Simulink PV system simulator with partial shading capability based on two-diode model. *Solar Energy, 85*(9), 2217-2227.

Jena, D., & Ramana, V. (2015). Modeling of photovoltaic system for uniform and non-uniform irradiance: A critical review. *Renewable and Sustainable Energy Reviews*(52), 400-417. doi:dx.doi.org/10.1016/j.rser.2015.07.079

Jinhui, X., Zhongdong, Y., Bingbing, W., & Jun, P. (2009). Design of PV array model based on EMTDC/PSCAD. Asia-Pasific.

Kampa, K., & Castanas, E. (2008). Human health effects of air pollution. *Environmental Pollution, 151*(2), 362-367.

Koirala, B., & Henze, N. (2009). Study on MPP mismatch losses in photovoltaic applicationa. *EU PVSEC Conference.* Research Gate. doi:10.4229/24thEUPVSEC2009-4BV.1.43

Kotti, R., & Shireen, W. (2015). Efficient MPPT control for PV systems adaptive to fast changing irradiation and partial shading conditions. *Solar Energy, 114*, 397-407. doi:10.1016/j.solener.2015.02.005

Litjens, G. B. (2013). *Investigation of Spectral Effects on Photovoltaic Technologies by Modelling the Solar Spectral Distribution - Master Thesis.* Utrecht University, Utrecht.

Lun, S., Wang, S., Yang, G., & Guo, T. (2015). A new explicit double-diode modeling method based on Lambert W-function for photovoltaic arrays. *Solar Energy, 114*, 69-82. doi:10.1016/j.solener.2015.03.043

MacAlpine, S., Brandemühl, M., & Erickson, R. (2011). Potential for Recoverable Power: Simulated use of distributed power converters at various levels in partially shaded photovoltaic arrays. *26th European Photovoltaic Solar Energy Conference and Exhibition* (pp. 3716-3720). EU PVSEC.

McIntosh, K. R., Altermatt, P. P., & Heiser, G. (2000). Depletion-region recombination in silicon solar cells: when does mDR=2. *Proceedings of the 16th European photovoltaic solar energy conference* (pp. 251-254). Glasgow, UK: EU PVSEC.

McKay, K. G. (1954). Avalanche breakdown in silicon. *Physical Review, 94*(4), 877.

Mejia, F. A., & Kleissl, J. (2013). Soiling losses for solar photovoltaic systems in California. *Solar Energy, 95*, 357-363.

Meteonorm. (2015). Handbook part II: Theory. In *Meteonorm 7 - Global Meteorological Database* (Vol. 7.1). Bern, Switzerland: Meteonorm. Retrieved from aiguasol.coop/docs/mn7_theory.pdf

Molenbroek, E., Waddington, D. W., & Emery, K. A. (1991). Hot spot susceptibility and testing of PV modules. *Photovoltaic Specialists Conference, Conference Record of the 22nd IEEE* (pp. 547-552). Golden, Colorado: IEEE Xplore. doi:10.1109/PVSC.1991.169273

Muelink & Grol and Burgerhout. (2007). *Prefab Schoorstenen - 2007 & 2008.* Netherlands: Muelink & Grol; Burgerhout. Retrieved February 2016, 29, from www.burgerhout.nl/Uploads/Docs/schoorsteencatalogus.pdf

Olukan, T. A., & Emziane, M. (2014). A Comparative Analysis of PV Temperature Models. *Energy Procedia, 62*, 694-703.

Pannebakker, B. B. (2014). *PV in the Shade - Designing methods to improve the shading-tolerance of solar modules - Master Thesis.* Utrecht, The Netherlands: Utrecht University.

Poshtkouhi, S., Palaniappan, V., Fard, M., & Trescases, O. (2012). A General Approach for Quantifying the Benefit of Distributed Power Electronics for Fine Grained MPPT in Photovoltaic Applications Using 3-D Modeling. *IEEE Transactions on Power Electronics, 27*, 4656-4666. doi:10.1109/TPEL.2011.2173353

PVPMC/Sandia. (2014a). *Plane of Array (POA) Irradiance*. Retrieved March 7, 2016, from Sandia PV Performance Modeling Collaborative: https://pvpmc.sandia.gov/modeling-steps/1-weather-design-inputs/plane-of-array-poa-irradiance/

PVPMC/Sandia. (2014b). *Physical IAM Model*. Retrieved 26 February, 2016, from Sandia PV Performance Modeling Collaborative: https://pvpmc.sandia.gov/modeling-steps/1-weather-design-inputs/shading-soiling-and-reflection-losses/incident-angle-reflection-losses/physical-model-of-iam/

PVPMC/Sandia. (2014c). *Albedo*. Retrieved March 31, 2016, from PV Performance Modeling Collaborative: https://pvpmc.sandia.gov/modeling-steps/1-weather-design-inputs/plane-of-array-poa-irradiance/calculating-poa-irradiance/poa-ground-reflected/albedo/

PVSyst. (2014). *PV Syst V6.26 - Software for the Study of Photovoltaic Systems.* Satigny, Switzerland: PvSyst SA.

PVSyst Help Files. (n.d.). *Grid Inverters, Main Parameters*. Retrieved March 14, 2016, from PV Syst Component Database: http://files.pvsyst.com/help/inverters_general.htm

Reindl, D. T., Beckman, W. A., & Duffie, J. A. (1990). Diffuse fraction correlations. *Solar Energy, 45*, 1-7.

Renewable Green Energy Power. (2015, November 23). *WP content - Uploads*. Retrieved from Renewable Green Energy Power Web site: www.renewablegreenenergypower.com/wp-content/uploads/2013/03/solar-string-inverter-connection-diagram.gif

Rizzo, S. A., & Scelba, G. (2015). ANN based MPPT method for rapidly variable shading conditions. *Applied Energy, 145*, 124-132.

Santos, R., & Gaspar, P. D. (2011). Computational tool for simulating the performance of photovoltaic panels. *International Conference on Engineering UBI2011.* Covilhã, Portugal: University of Beira Interior.

Senter Novem & VROM. (2007). *Voorbeeldwoningen bestaande bouw 2007.* Sittard: Senter Novem.

Shimrat, M. (1962). Algorithm 112: Position of point relative to polygon. *Communications of the ACM, 5*(8).

Silvestre, S., Boronat, A., & Chouder, A. (2009). Study of bypass diodes configuration on PV modules. *Applied Energy, 86*(9), 1632-1640. doi:10.1016/j.apenergy.2009.01.020

Sinapis, K., Litjens, G., & Van den Donker, M. (2014, June 10). MLPM project - Update test field results - Presentation. Petten, The Netherlands: ECN. Retrieved February 29, 2016

Sinapis, K., Litjens, G., Donker, M., & Folkerts, W. (2015). Outdoor characterization of three PV architectures under clear and shaded conditions. *Solar Energy, 2014*.

Sinapis, K., Tzikas, C., Litjens, G., Van den Donker, M., Folkerts, W., Van Sark, W., & Smets, A. (in press). A comprehensive study on partial shading response of c-Si modules and yield modelling of string and module level power electronics.

Souka, A., & Safwat, H. (1966). Determination of the optimum orientations for the double-exposure, flat-plate collector and its reflectors. *Solar Energy, 10*(4), 170-174.

Suckow, S., Pletzer, T. M., & Kurz, H. (2014). Fast and reliable calculation of the two-diode model without simplifications. *Progress in Photovoltaics, 22*, 494-501.

Sundareswaran, K., Vignesh, V., & Palani, S. (2015). Application of a combined particle swarm optimization and perturb and observe method for MPPT in PV systems under partial shading conditions. *Renewable Energy, 75*, 308-317. doi:10.1016/j.renene.2014.09.044

Swaleh, M. S., & Green, M. A. (1982). Effect of shunt resistance and bypass diodes on the shadow tolerance of solar cell modules. *Solar Cells, 5*(2), 183-198.

Twidell, J., & Weir, T. (2006). *Renewable Energy Resources* (2nd ed.). London: Taylor & Francis.

Tyagi, V., Nurul, A., Rahim, N. J., & Selvaray, L. (2013). Progress in solar PV technology: Research and achievement. *Renewable and Sustainable Energy Reviews, 20*, pp. 443-461. doi:10.1016/j.rser.2012.09.028

Tzikas, C. (2015). *MLPM Yield model - Master Thesis.* Eindhoven: SEAC.

Ubbink. (2016). *Ventub Ventilatiepijp - D110 mm - L700mm - met schaal - zwart*. Retrieved February 29, 2016, from Ubbink BV Web Site: http://www.ubbink.nl/Producten/Productgroepen/Dakdoorvoer/Ventub-dakdoorvoer-0169670.aspx

Van Zeghbroek, B. (2011). Principles of Semiconductor Devices. Retrieved February 23, 2016, from http://ecee.colorado.edu/~bart/book/book/chapter2/ch2_3.htm

Verberne, G. (2014). *BIPV as a pitched roofing solution - A feasibility study for the Dutch market - Master Thesis.* Eindhoven: SEAC.

Villalva, M. G., Gazoli, J. R., & Filho, E. R. (2009). Comprehensive Approach to Modeling and Simulation of Photovoltaic Arrays. *IEEE Transactions on Power Electronics, 24*(5), 1198-1208.

Williams, N. J., Jaramillo, P., Taneja, J., & Ustun, T. S. (2015). Enabling private sector investment in microgrid-based rural electrification in developing countries: A review. *Renewable and Sustainable Energy Reviews*, 1268-1281.

Wise, S. (2002). *GIS Basics.* CRC Press.

Woyte, A., Nijs, J., & Belmans, R. (2003). Partial shadowing of photovoltaic arrays with different system configurations: literature review and field test results. *Solar Energy, 74*, 217-233.

Yallop, B. D. (1992). *Private Communication.* London: Royal Greenwich Observatory.

# Appendices

## Annex A – SketchUp object coordinate examples

Note that the left-bottom point of the leftmost terraced house is considered as the point with coordinates (0.0129, 0.0655, 0). The *x*-coordinate is defined positively eastward, the *y*-coordinate positively northward and *z* upwards from the surface. The object coordinate examples presented in the table below are all for the most centrally located house in the row.

Table A.1 shows the coordinates for the rooftop and shading objects; table A.2 for an example module and the nine modeled panel planes.

Table A.1 – Rooftop and shading objects' coordinates

| **Object** | **Edge point** | ***x* [m]** | ***y* [m]** | ***z* [m]** |
|---|---|---|---|---|
| Rooftop | | | | |
| | LB | 13.2129 | 0.0655 | 5.72 |
| | RB | 19.8129 | 0.0655 | 5.72 |
| | RT | 13.2129 | 3.5155 | 8.615 |
| | LT | 19.8129 | 3.5155 | 8.615 |
| Exhaust pipe A (left) | | | | |
| | Bottom central (BC) | 19.26145 | 2.80448 | 7.771365 |
| | Top central (TC) | 19.26145 | 2.80448 | 8.771365 |
| Exhaust pipe B (right) | | | | |
| | Bottom central (BC) | 19.37145 | 2.80448 | 7.771365 |
| | Top central (TC) | 19.37145 | 2.80448 | 8.771365 |
| Chimney | | | | |
| | LB – bottom surface | 13.2129 | 3.2655 | 8.4052 |
| | RB – bottom surface | 13.7129 | 3.2655 | 8.4052 |
| | RT – bottom surface | 13.7129 | 3.7655 | 8.4052 |
| | LT – bottom surface | 13.2129 | 3.7655 | 8.4052 |
| | LB – top surface | 13.2129 | 3.2655 | 9.415 |
| | RB – top surface | 13.7129 | 3.2655 | 9.415 |
| | RT – top surface | 13.7129 | 3.7655 | 9.415 |
| | LT – top surface | 13.2129 | 3.7655 | 9.415 |
| Dormer | | | | |
| | LB – bottom surface | 15.7066 | 0.4466 | 6.0398 |
| | RB – bottom surface | 17.3066 | 0.4466 | 6.0398 |
| | RT – bottom surface | 17.3066 | 2.5321 | 6.0398 |
| | LT – bottom surface | 15.7066 | 2.5321 | 6.0398 |
| | LB – top surface | 15.7066 | 0.4466 | 7.7898 |
| | RB – top surface | 17.3066 | 0.4466 | 7.7898 |
| | RT – top surface | 17.3066 | 2.5321 | 7.7898 |
| | LT – top surface | 15.7066 | 2.5321 | 7.7898 |

Table A.2a – Example module and panel objects' coordinates

| Object | Edge point | *x* [m] | *y* [m] | *z* [m] |
|---|---|---|---|---|
| Module 1 | | | | |
| | LB – bottom surface | 14.0206 | 2.6506 | 7.9315 |
| | RB – bottom surface | 15.6805 | 2.6496 | 7.9185 |
| | RT – bottom surface | 15.6860 | 3.4004 | 8.5638 |
| | LT – bottom surface | 14.0261 | 3.4014 | 8.5769 |
| | LB – top surface | 14.0208 | 2.6246 | 7.9619 |
| | RB – top surface | 15.6807 | 2.6236 | 7.9488 |
| | RT – top surface | 15.6863 | 3.3743 | 8.5942 |
| | LT – top surface | 14.0263 | 3.3753 | 8.6072 |
| Panel 1 | | | | |
| | LB | 14.050907 | 2.639709 | 7.974683 |
| | RB | 15.650857 | 2.638757 | 7.962088 |
| | RT | 15.656216 | 3.366746 | 8.587871 |
| | LT | 14.056266 | 3.367697 | 8.600466 |
| Panel 2 | | | | |
| | LB | 15.710855 | 2.638722 | 7.961616 |
| | RB | 17.310805 | 2.637770 | 7.949021 |
| | RT | 17.316164 | 3.365758 | 8.574804 |
| | LT | 15.716214 | 3.366710 | 8.587399 |
| Panel 3 | | | | |
| | LB | 17.371026 | 2.638722 | 7.949936 |
| | RB | 18.970977 | 2.637770 | 7.937341 |
| | RT | 18.976336 | 3.365758 | 8.563124 |
| | LT | 17.376385 | 3.366710 | 8.575719 |
| Panel 4 | | | | |
| | LB | 13.645380 | 1.888971 | 7.329344 |
| | RB | 15.245330 | 1.888020 | 7.316749 |
| | RT | 15.250689 | 2.616008 | 7.942532 |
| | LT | 13.650739 | 2.616959 | 7.955127 |
| Panel 5 | | | | |
| | LB | 13.639853 | 1.138233 | 6.684006 |
| | RB | 15.239804 | 1.137282 | 6.671411 |
| | RT | 15.245163 | 1.865270 | 7.297194 |
| | LT | 13.645212 | 1.866221 | 7.309789 |
| Panel 6 | | | | |
| | LB | 13.634327 | 0.387495 | 6.038667 |
| | RB | 15.234277 | 0.386544 | 6.026072 |
| | RT | 15.239636 | 1.114532 | 6.651855 |
| | LT | 13.639686 | 1.115484 | 6.664450 |

Table A.2b – Example module and panel objects' coordinates (continued)

| Object | Edge point | *x* [m] | *y* [m] | *z* [m] |
|---|---|---|---|---|
| Panel 7 | | | | |
| | LB | 17.877285 | 1.887679 | 7.300568 |
| | RB | 19.477235 | 1.886728 | 7.287973 |
| | RT | 19.482594 | 2.614716 | 7.913757 |
| | LT | 17.882644 | 2.615668 | 7.926351 |
| Panel 8 | | | | |
| | LB | 17.871758 | 1.136942 | 6.655230 |
| | RB | 19.471708 | 1.135990 | 6.642635 |
| | RT | 19.477067 | 1.863978 | 7.268418 |
| | LT | 17.877117 | 1.864930 | 7.281013 |
| Panel 9 | | | | |
| | LB | 17.866232 | 0.386204 | 6.009891 |
| | RB | 19.466182 | 0.385252 | 5.997296 |
| | RT | 19.471541 | 1.113240 | 6.623079 |
| | LT | 17.871591 | 1.114192 | 6.635674 |

## Annex B – Cell location and numbering derivation

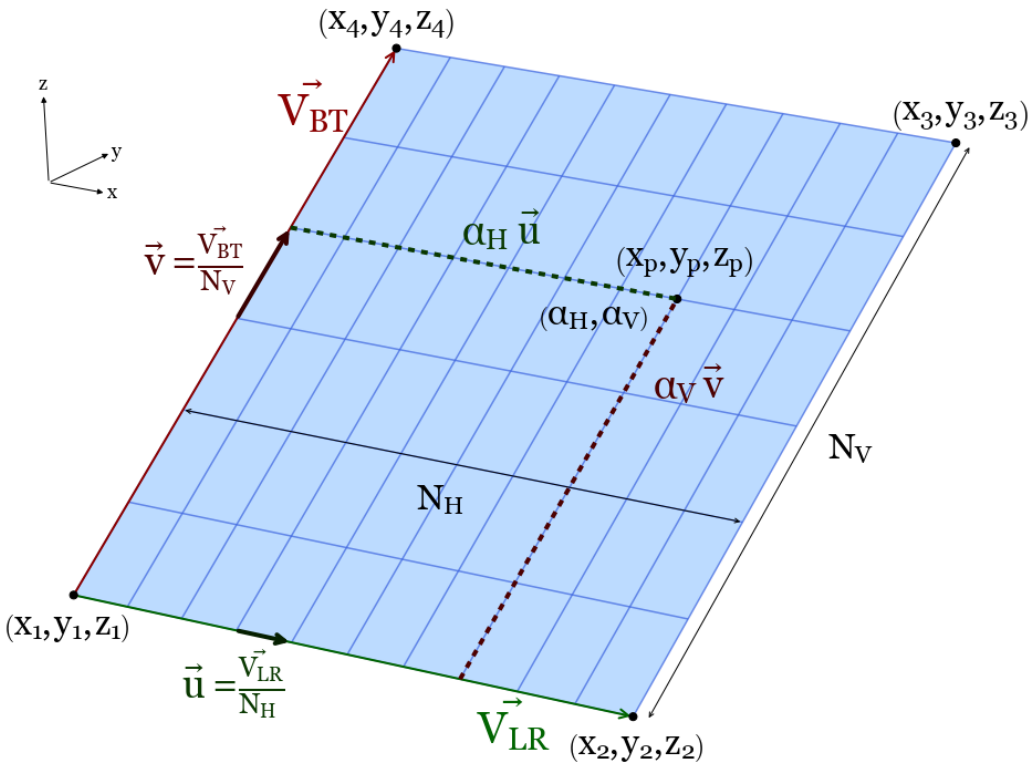


*Figure Ba: Derivation of cell edge coordinates ($x_p$,$y_p$,$z_p$) using the four panel edge points.*

To obtain the precise coordinates of the cell edges of a solar panel, the LB, RB, RT and LT edges of the panel cell grid[18] are shot using a PointCloud tool in SketchUp. Besides, these points are allocated numbers 1 to 4 respectively. Then Equations B.1 and B.2 are used to determine the left-right (horizontal) and bottom-top (vertical) panel direction vectors:

$$\vec{V}_{LR} = (x_1 - x_2,\ y_1 - y_2\ , z_1 - z_2) \quad \text{(B.1)}$$

$$\vec{V}_{BT} = (x_1 - x_4,\ y_1 - y_4\ , z_1 - z_4) \quad \text{(B.2)}$$

Subsequently, dividing by the amount of horizontally and vertically stacked cells in the panel grid gives the horizontal and vertical unit direction vectors:

$$\vec{u} = \vec{V}_{LR}/N_H \quad \text{(B.3)}$$

$$\vec{v} = \vec{V}_{BT}/N_V \quad \text{(B.4)}$$

Now, any cell edge point ($x_p$,$y_p$,$z_p$) on the panel grid plane can be found:

$$(x_p, y_p, z_p) = (x_1, y_1, z_1) + \alpha_H \vec{u} + \alpha_V \vec{v} \quad \text{(B.5)}$$

Figure Ba shows a graphical illustration accompanying the provided explanation.

[18] Please note that these edges are **not** the module edges (as modules generally have a margin enveloping the cell panel grid).

After determination of the cell edge locations, all cells in the panel plane are allocated cell numbers corresponding to their relative position in the solar panel:

$$\zeta(\alpha_H, \alpha_V, N_H) = \begin{cases} N_H\alpha_V + (\alpha_H + 1) & [if\ \alpha_V\ even] \\ (2N_H\alpha_V + 1) - \big(N_H(\alpha_V - 1) + (\alpha_H + 1)\big) & [if\ \alpha_V\ odd] \end{cases} \quad \text{(B.6)}$$

Cell numbers are allocated as follows if the cells are aligned vertically instead of horizontally:

$$\zeta_V(\alpha_H, \alpha_V, N_V) = \begin{cases} N_V\alpha_H + (\alpha_V + 1) & [if\ \alpha_H\ even] \\ (N_V - \alpha_V) + N_V\alpha_H & [if\ \alpha_H\ odd] \end{cases} \quad \text{(B.7)}$$

In these expressions $\alpha_H$ and $\alpha_V$ represent the grid coordinates belonging to the left bottom cell edge point. For example, cell number 1 has panel grid coordinates $(\alpha_H, \alpha_V) = (0, 0)$.

## Annex C – Along-rib intersection points

Internal (along-rib) shade projection-panel plane intersection points $\xi_p$ can be found using subsequent line parameterizations along the vertical, horizontal counterclockwise and clockwise directions as mentioned in section 3.2.3.

First the vertical shade object rib vector $\vec{v}_V$ is defined to check whether an internal intersection point $\xi_p$ exists along this direction (if the related point *n* lies on the bottom surface):

$$\vec{v}_V = ((x_T - x_B), (y_T - y_B), (z_T - z_B)) \qquad \text{(C.1)}$$

In Equation C.1, $B = min(n, n+N_P/2)$ and $T = max(n, n+N_P/2)$ are the bottom-surface and associated top-surface points.

The vertical line parameterization constant $k_V$ can then be calculated in the following way:

$$k_V = \frac{d - (ax_B + by_B + cz_B)}{a(x_T - x_B) + b(y_T - y_B) + c(z_T - z_B)} \qquad \text{(C.2)}$$

If $k_V$ lies between 0 and 1, $\xi_p$ lies on the rib connecting B and T and is then identified as a valid intersection point[19]:

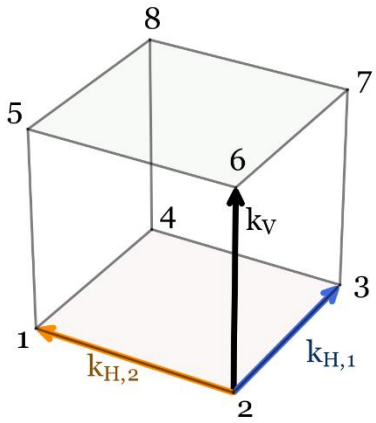


*Figure Ca: Direction of vectors ($\vec{v}_V$, $\vec{v}_{H1}$, $\vec{v}_{H2}$) along ribs in a cuboid shade object, along with the positive directions of constants $k_V$, $k_{H,1}$ and $k_{H,2}$ and edge point numbers relative to edge point n = 2.*

$$\left(x_{\xi_p}, y_{\xi_p}, z_{\xi_p}\right) = ((x_B + k_V(x_T - x_B)), (y_B + k_V(y_T - y_B)), (z_B + k_V(z_T - z_B))) \qquad \text{(C.3)}$$

$\xi_p$ lies outside the shading object and is therefore not a valid intersect for all other values of $k_V$.

Subsequently, if no valid $\xi_p$ is found on the vertical rib of the shading object or if point *n* is part of the top surface, try to find $\xi_p$ on the counterclockwise horizontal shade object rib vector:

$$\vec{v}_{H1} = ((x_D - x_n), (y_D - y_n), (z_D - z_n)) \qquad \text{(C.4)}$$

In Equation C.4, *D* is the point with the number *n+1* unless $n = N_P/2$ or $N_P$. In these cases $D = 1$ or $D = 1+N_P/2$ respectively. Constant $k_{H,1}$ is derived in a similar fashion as $k_V$:

$$k_{H,1} = \frac{d - (ax_n + by_n + cz_n)}{a(x_D - x_n) + b(y_D - y_n) + c(z_D - z_n)} \qquad \text{(C.5)}$$

$\xi_p$ lies on the rib connecting points *n* and *D* and is then identified as a valid intersection point if $k_{H,1}$ lies in the range between 0 and 1:

$$\left(x_{\xi_p}, y_{\xi_p}, z_{\xi_p}\right) = ((x_n + k_{H,1}(x_D - x_n)), (y_n + k_{H,1}(y_D - y_n)), (z_n + k_{H,1}(z_D - z_n))) \qquad \text{(C.6)}$$

For all other values of $k_{H,1}$, $\xi_p$ lies outside the shading object. This then yields an invalid intersect. In that case, ultimately try to find $\xi_p$ using the clockwise horizontal shade object rib vector:

$$\vec{v}_{H2} = ((x_E - x_n), (y_E - y_n), (z_E - z_n)) \qquad \text{(C.7)}$$

Now point *E* has number *n-1* unless $n = 1$ or $n = 1+N_P/2$. In these cases $E = N_P/2$ or $E = N_P$ for the bottom and top surfaces of the shade object respectively.

[19] If $k_V$ lies outside this range it means that the associated intersection point does not lie on the rib, but above it (if $k_V > 1$) or below it (if $k_V < 0$).

Now constant $k_{H,2}$ is derived in a way similar to $k_V$ and $k_{H,1}$:

$$k_{H,2} = \frac{d - (ax_n + by_n + cz_n)}{a(x_E - x_n) + b(y_E - y_n) + c(z_E - z_n)} \tag{C.8}$$

If $k_{H,2}$ is between 0 and 1, $\xi_p$ lies on the rib connecting points *E* and *F* and is ultimately marked as a valid intersection point:

$$\left(x_{\xi_p}, y_{\xi_p}, z_{\xi_p}\right) = ((x_n + k_{H,2}(x_E - x_n)), (y_n + k_{H,2}(y_E - y_n)), (z_n + k_{H,2}(z_E - z_n))) \tag{C.9}$$

In the case that this latter step still does not result in a valid intersection point $\xi_p$, it means that neither point *n* nor the ribs connecting point *n* to its neighboring edge points leave a shade projection on the panel plane of interest.

## Annex D - Outward projection points algorithm

As mentioned in section 3.2.3, the final shadow polygon only consists of the most outward found intersection points. Thus the objective here is to find the outward points from a given set of points. In computer science this type of problem is known as a convex hull problem. In this study an algorithm based on the Graham Scan (Graham, 1972) is used. A stepwise recipe for the algorithm is provided in Table D.1 below. A graphical illustration is shown in Figure Da.

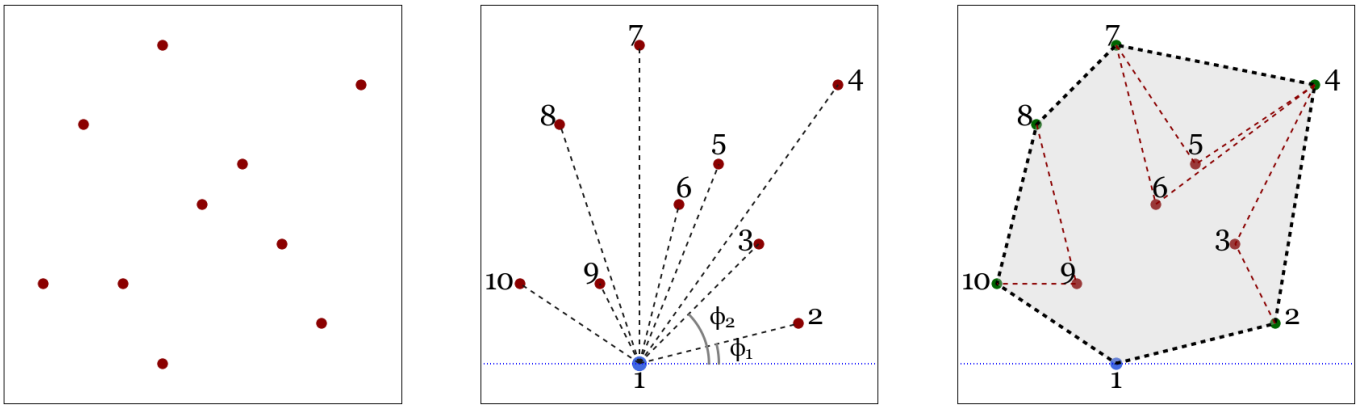


*Figure Da: Convex hull algorithm illustration. Left: a random set of points on the panel plane. Middle: finding the point ξ with minimal $y_\xi$(, $x_\xi$) and sorting the points on polar angle $\varphi_{i-1}$ (and on distance if polar angles are equal for multiple points) is the starting point for the convex hull points searching procedure. Right: any point delivering a non-counterclockwise movement with respect to its two valid convex hull neighbor points does not lie on the convex hull. In this way, any internal point can be filtered out. By this elimination procedure the external points on the convex hull are found. These convex hull points represent the projection edge points of the final shadow projection shape.*

Table D.1: Applied convex hull algorithm

| Step | Action |
|---|---|
| 1 | Retrieve the list of intersection points L($\xi_n$, $\xi_p$) following the method of section 3.2.3 |
| 2 | Obtain point with minimal $y_\xi$ (if multiple, take point with min $x_\xi$ as well) |
| 3[a] | Sort points on ascending polar angle $\varphi_{i-1}$ with respect to point with minimal $y_\xi$(, $x_\xi$) |
| 3[b] | If points have (nearly) equal $\varphi_{i-1}$, sort on ascending distance to point ξ(min $y_\xi$(, $x_\xi$)) |
| 4 | Remove points if for both $\Delta\varphi_i$ and Δdistance $\lvert\varepsilon\rvert < \varepsilon_{threshold}$ (e.g.: $10^{-7}$) (duplicates) |
| 5 | Continue if remaining number of points > 2; otherwise return all points and stop |
| 6 | Number the remaining points *i* based on their order in sorted list L |
| 7 | Add first two points to final list $L_f$ (points 1 & 2 are always part of the convex hull) |
| 8 | Number all unfalsified convex hull points *j* |
| 9 | Start with point in list L with number $i = 3$ |
| 10 | If movement from point *j*-2 to *j-1* to *i* is not counterclockwise, remove *j*-1 from $L_f$ |
| 11 | Repeat step 10 with $i_{new} = i_{old}+1$ until $i_{new} = \max(i)$ |
| 12 | Add point $i = 3$ to $L_f$ as new point *j-1* |
| 13 | Repeat steps 10 – 12 for $i = 4,5,$ … up to and including $i = \max(i)-1$ |
| 14 | Point $i = \max(i)$ of sorted list L always lies on the convex hull; add this point to list $L_f$ |
| 15 | Return the final list $L_f$ containing all valid convex hull points *j* |

## Annex E – Cell shade percentage algorithm

Firstly, the location of $v^2$ points ($v$ horizontal points; $v$ vertical points) within a cell are determined. In this model, $v$ = 10 is used. From Annex B, the horizontal and vertical cell directions are determined as $\vec{u}$ and $\vec{v}$. The location of LB cell edges for each cell follow from Equation B.5. Now the location of each of the $v^2$ points, also noted as $v_{ij}$ – where $i$ and $j$ represent the horizontal and vertical coordinate numbers within the cell ($0 \leq i, j \leq v\text{-}1$) – is derived as follows:

$$\left(x_{v_{ij}}, y_{v_{ij}}, z_{v_{ij}}\right) = \left(x_{LB,c}, y_{LB,c}, z_{LB,c}\right) + (1/2 + i/v)\vec{u} + (1/2 + j/v)\vec{v} \qquad \text{(E.1)}$$

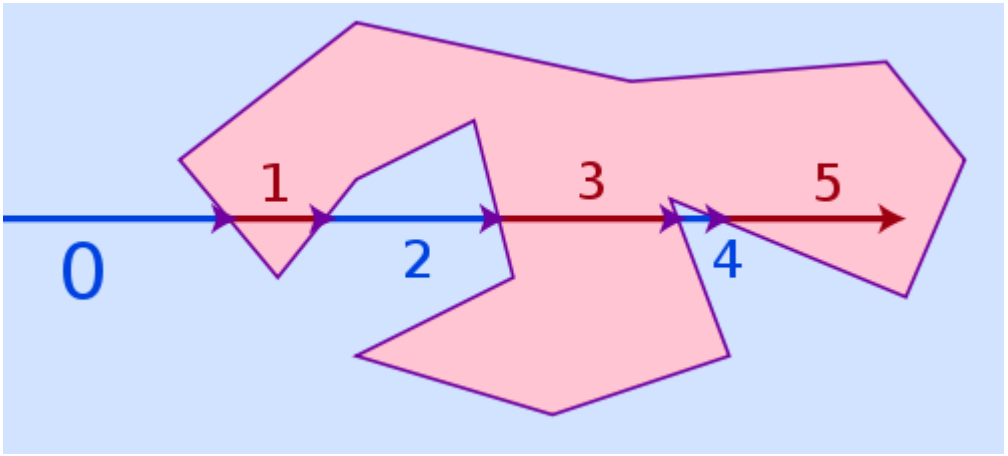


*Figure Ea: Illustration of ray casting algorithm logic (Wise, 2002). If the amount of intersects between a ray from point $v_{ij}$ and a polygon's edge lines is zero or even, point $v_{ij}$ lies outside the (casted shading) polygon; the point lies inside it if the amount of edge line intersects is odd.*

Secondly, the aim is to evaluate for all $v^2$ points whether they lie within one of the casted shade polygons or not. In other words, whether a point lies in shaded or in unshaded area. In order to do this, a ray casting algorithm is used (Shimrat, 1962) – as in previous work similar to this research (Sinapis, et al., in press; Tzikas, 2015). This method is also referred to as the crossing number algorithm or even-odd algorithm. It tests how many times a ray starting from point $v_{ij}$ intersects the edges of a polygon. If this is a zero or even amount of times, the point is said to lie outside the polygon; if odd, it lies inside it. Also see Figure Ea. This eventually yields a total number of points $v_S$ located inside the shading polygon.

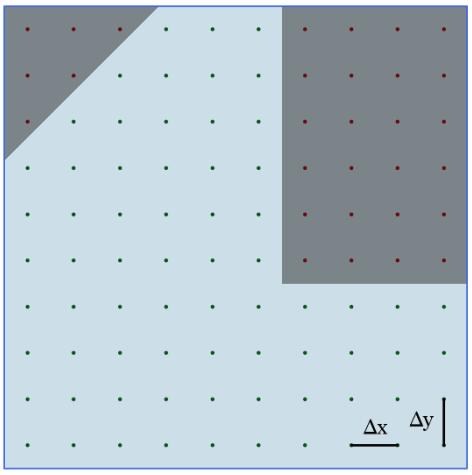


*Figure Eb: Example of cell containing $v^2$ (= 100) evaluation points. Distances $\Delta x$ and $\Delta y$ equal $\vec{u}/v$ and $\vec{v}/v$ respectively. The two shading polygons result in a cell shade percentage $\sigma_P$ of 30% here.*

Finally, the cell shade percentage $\sigma_P$ is calculated:

$$\sigma_P = 100\% \cdot v_S / v^2 \qquad \text{(E.2)}$$

Refer to Figure Eb for an illustrated example.

## Annex F – Series and shunt resistances algorithm

As mentioned in section 2.4.1, the parameters $I_{SC,\,STC}$, $I_{MPP,\,STC}$, $V_{OC,\,STC}$ and $V_{MPP,\,STC}$ are known from the PV module manufacturer's data sheets. The maximum rated power (at STC) then follows from:

$$P_{MPP,STC} = V_{MPP,STC} \cdot I_{MPP,STC} \tag{F.1}$$

The series and shunt resistances at the MPP at STC are approximated by means of the iteration algorithm (Tzikas, 2015) listed in Table 2.5.1. Note: the example values for $\delta_{step}$, $I_{test}$ and $\varepsilon_P$ in Table F.1 are the values used in the actual model run.

Table F.1: Series and shunt resistance determination algorithm

| Step | Action | Equation(s) |
|---|---|---|
| 1 | Start with $R_s$ at a positive near-zero value $\delta_{step}$ [e.g.: 0.001] | |
| 2 | Initial calculation of $R_{sh}$ | F.2 |
| 3 | Calculate $V_{th}$, $I_{ph,\,STC}$, $I_{o,\,STC}$ | 2.18; 2.20; 2.22 |
| 4 | Update $R_{sh}$ | F.3 |
| 5 | Start iteration test value $I_{test}$ at positive near-zero value [e.g.: 0.1] | |
| 6 | Calculate $I_{new}$ by plugging $I_{test}$ into RHS of implicit equation | 2.17 |
| 7 | Replace $I_{test}$ by $I_{new}$ if $\lvert I_{test}-I_{new}\rvert > \varepsilon_I$ | |
| 8 | Repeat steps 6 and 7 until $\lvert I_{test}-I_{new}\rvert \leq \varepsilon_I$ | |
| 9 | $I_x = I_{test}$ | |
| 10 | Determine value of $P_{x,\,max} = \max(V(I_x)\cdot I_x)$ | |
| 11 | $\varepsilon = \lvert P_{MPP,\,STC} - P_{x,\,max}\rvert$ | |
| 12 | Repeat steps 3 - 11 with $R_s = R_s + \delta_{step}$ until $\varepsilon \leq \varepsilon_P$ [e.g.: $\varepsilon_P$=0.35%] | |
| 13 | Return $R_s$, $R_{sh}$ satisfying $\varepsilon \leq \varepsilon_P$ (or error if no convergence) | |

The relevant equations for the shunt resistance in the algorithm are:

$$R_{sh} = \frac{V_{MPP,STC}}{I_{SC,STC} - I_{MPP,STC}} - \frac{V_{OC,STC} - V_{MPP,STC}}{I_{MPP,STC}} \tag{F.2}$$

$$R_{sh} = \frac{V + I \cdot R_s}{I_{ph} - I_o \cdot \left(\exp\left(\frac{V + IR_s}{n_1 V_{th}}\right) + \exp\left(\frac{V + IR_s}{n_2 V_{th}}\right) - 2\right) - \frac{P_{MPP,STC}}{V}} \tag{F.3}$$

Note: throughout Equation 2.42, $V$ and $I$ represent $V_{MPP,\,STC}$ and $I_{MPP,\,STC}$ respectively.

## Annex G – IV curve algorithm

The module resistances are derived from the methodology outlined in section 3.5.2.

$$N_{bpd} = N_s/(N_p \cdot S_c) \quad \text{(G.1)}$$

$$V_{OC,s} = S_c \cdot V_{OC,m}/N_s \quad \text{(G.2)}$$

$$I_{SC,s} = I_{SC,m} \quad \text{(G.3)}$$

$$R_{s,s} = S_c \cdot R_{s,m}/N_s \quad \text{(G.4)}$$

$$R_{sh,s} = (G/G_{STC}) \cdot S_c \cdot R_{sh,m}/N_s \quad \text{(G.5)}$$

$$V_{OC,s} = V_{th} \cdot \ln(I_{ph}/I_o) \quad \text{(G.6)}$$

Important to note is that Equations G.2 to G.5 above are only valid if all cells and substrings in the module are aligned in series: $N_p = 1$. This module circuitry is used throughout this report.

The output current iteration algorithm (Suckow, Pletzer, & Kurz, 2014) used in this study makes use of a root function version of Equation 1.43, where $f(I) = 0$ represents a fitting value for output current $I$:

$$f = f(I) = -I - I_{ph} - I_o\left(e^{\frac{V+IR_s}{n_1 V_{th}}} - 1\right) - I_o\left(e^{\frac{V+IR_s}{n_2 V_{th}}} - 1\right) - \left(\frac{V + IR_s}{R_{sh}}\right) \quad \text{(G.7)}$$

In the custom root finding procedure (steps 18 to 22 in Table G.1), a combined subsequent Newton-Raphson (NR) and bisection search (BS) root finding algorithm is recommended to combine the fast convergence possibilities of NR with the high convergence stability of BS (Suckow, Pletzer, & Kurz, 2014). For the NR part, Equations G.8 and G.9 are used to update the trial values for the output current.

$$df/dI = -1 - \frac{R_s I_o}{n_1 V_{th}}\left(e^{\frac{V+IR_s}{n_1 V_{th}}} - 1\right) - \frac{R_s I_o}{n_2 V_{th}}\left(e^{\frac{V+IR_s}{n_2 V_{th}}} - 1\right) - \frac{R_s}{R_{sh}} \quad \text{(G.8)}$$

$$I_{test,new} = I_{test,old} - \frac{f(I_{test,old})}{df(I_{test,old})/dI} \quad \text{(G.9)}$$

The complete procedure for finding the substring IV curve is outlined in Table G.1. Note that steps 1 to 6 follow from previous similar work (Sinapis, et al., in press; Tzikas, 2015). In terms of content, steps 7 to 17 are directly derived from the work on the output current iteration algorithm noted before (Suckow, Pletzer, & Kurz, 2014). The same article provides the structural outline used for the custom root finding procedure in steps 18 to 22 as mentioned before.

Refer to Figure Ga for a flow chart of the main iterative components of the output current calculation algorithm described in this section.

On top of the methodology outlined in this Annex, some additional stability-improving conditions have been applied in the algorithmic procedure described in this section (although they should generally not be necessary). For more background on the stepwise motivation for the used algorithm, consult the accompanying reference (Suckow, Pletzer, & Kurz, 2014).

Table G.1: Substring IV curve determination algorithm

| Step | Action | Equation(s) |
|---|---|---|
| 1[a] | Pick suitable G, $T=T_s$, $N_s$ and $S_C$ | |
| 1[b] | Set $N_p = 1$; $n_1 = 1$; $n_2 = 2$ | |
| 2 | Calculate $N_{bpd}$, $I_{SC,\,s}$, $V_{OC,\,s}$, $R_{s,\,s}$, $R_{sh,\,s}$ | G.1 – G.5 |
| 3 | Determine $V_{th,\,STC}$, $V_{th}$, $I_{ph}$, $I_o$ | 2.18, 2.19, 2.23 |
| 4 | Update $V_{OC,\,s}$ | G.6 |
| 5 | Create 500 evenly spaced points $V_i$ from V = 0 to $V = V_{OC,\,s}$ | |
| 6 | Put $I_{test,i}(V_i) = 0$, $\varepsilon = 10^{-10}$; determine $f(0)$ | G.7 |
| 7[a] | If $f(0) > \pm \varepsilon$, continue to step 8 | |
| 7[b] | Otherwise, return $I_i(V_i) = 0$ and go to step 23 | |
| 8 | Adjust $\delta_{step} = \pm \varepsilon$ to match the sign of $f(0)$ | |
| 9 | Set $I_{test,i}(V_i)$ at $I_{i-1}(V_{i-1})$ (0 if $i = 0$) | |
| 10 | Calculate $f(I_{test,i}(V_i))$ | G.7 |
| 11[a] | If $f(I_{test,i}(V_i)) > \pm \varepsilon$, continue to step 12 | |
| 11[b] | Otherwise, return $I_i(V_i) = I_{test,i}(V_i)$ and go to step 23 | |
| 12 | Adjust $\delta_{step} = \pm 0.1 \cdot \max(f, 10 \cdot \varepsilon)$ to match the sign of $f$ | |
| 13 | Store $f$; $I_{test,i}(V_i)$ as $f_{old}$; $I_{old}$ | |
| 14 | Set new $I_{test,i}(V_i) = I_{old} + \delta_{step}$ | |
| 15 | Calculate $f(I_{test,i}(V_i))$ | G.7 |
| 16[a] | If $f \cdot f_{old}$ is negative, set $I_{lo}$; $I_{hi} = \min(I_{old}, I_{test,i})$; $\max(I_{old}, I_{test,i})$ | |
| 16[b] | Otherwise, double $\delta_{step}$ | |
| 17 | Repeat steps 13 – 16 until $f \cdot f_{old}$ is negative | |
| 18 | Set $I_{old}(V_i) = I_{new}(V_i)$; use $I_{old}(V_i) = I_{lo}$ instead at first pass | |
| 19 | Take new guess $I_{new}(V_i)$ using NR method | G.9 |
| 20 | Determine $f(I_{new}(V_i))$ | G.7 |
| 21[a] | If $\lvert f(I_{new}(V_i)) \rvert \leq \lvert \varepsilon \rvert$, return $I_i(V_i) = I_{test,i}(V_i)$ and proceed to step 23 | |
| 21[b] | Else, if the number of NR passes < 30, repeat steps 18 – 20 | |
| 21[c] | After the 30th passing of loop 18 – 21, continue to step 22 | |
| 22 | Use standard BS algorithm to find $I_i(V_i)$ in interval $[I_{lo}; I_{hi}]$ | |
| 23 | Repeat steps 6 – 22 until all 500 values of $I_i(V_i)$ are obtained | |

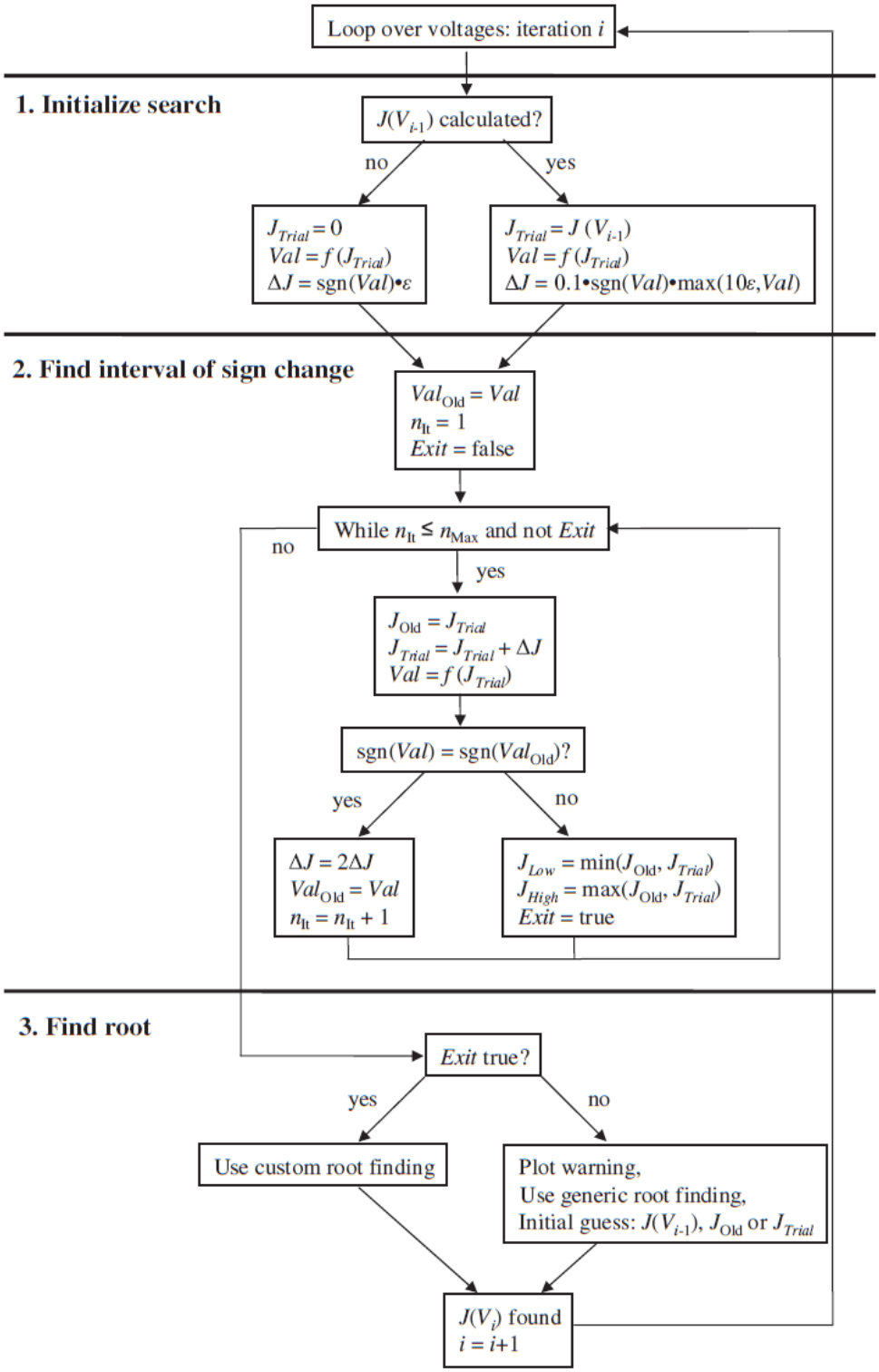


*Figure Ga: IV curve algorithm flowchart. Note that the notation here represents current density J instead of total output current I. As I is simply J multiplied by the area of the substring considered in this research (although not explicitly written out as such in the main report), the stepwise procedure will be the same for current I as for current density J. Source: Suckow et al. (2014).*

## Annex H – String inverter efficiencies

The efficiencies of the Sunny Boy SB 2500TLST-21 central string inverter as reported by PV Syst (PVSyst, 2014) are listed in Table H.1. Note that *P* represents the DC input power here.

Table H.1: Sunny Boy SB 2500TLST-21 string inverter efficiencies (PVSyst, 2014)

| $V_i$ (V) | $P_i$ ($W_{DC}$) | Inverter Efficiency |
|---|---|---|
| 180 | | |
| | 30 | 0.0 % |
| | 160 | 87.2 % |
| | 320 | 91.4 % |
| | 640 | 94.2 % |
| | 960 | 95.3 % |
| | 1600 | 96.0 % |
| | 2400 | 96.2 % |
| | 2500 | 96.2 % |
| 400 | | |
| | 30 | 0.0 % |
| | 160 | 87.8 % |
| | 320 | 92.4 % |
| | 640 | 95.1 % |
| | 960 | 96.0 % |
| | 1600 | 96.7 % |
| | 2400 | 97.0 % |
| | 2500 | 97.0 % |
| 500 | | |
| | 30 | 0.0 % |
| | 160 | 85.2 % |
| | 320 | 90.6 % |
| | 640 | 94.0 % |
| | 960 | 95.3 % |
| | 1600 | 96.2 % |
| | 2400 | 96.6 % |
| | 2500 | 96.7 % |

## Annex I – Per-panel DC shading index tables

The tables shown below illustrate the per-panel DC shading index values. This is done for each per-module BPD case that is embodied within this study.

Tables I.1 through I.5 show the per-panel DC shade losses for south, east, west, south-east and south-west roof orientations respectively.

Table I.1 – Per-panel shading index values for south roof orientation

| Panel # | Ref (3 BPDs per module) | 5 BPDs (V) | 6 BPDs | 10 BPDs (V) | 12 BPDs | 30 BPDs | 60 BPDs |
|---|---|---|---|---|---|---|---|
| No shade | 0.0 % | 0.0 % | 0.0 % | 0.0 % | 0.0 % | 0.0 % | 0.0 % |
| Panel 1 | 0.9 %* | 0.9 % | 0.7 % | 0.9 % | 0.6 % | 0.5 % | 0.4 %* |
| Panel 2 | 0.4 %* | 0.4 % | 0.4 % | 0.4 % | 0.3 % | 0.3 % | 0.2 %* |
| Panel 3 | 6.5 %* | 4.9 % | 5.3 % | 4.2 % | 3.4 % | 2.1 % | 1.7 %* |
| Panel 4 | 4.5 %* | 3.7 % | 3.9 % | 3.3 % | 2.4 % | 1.6 % | 1.3 %* |
| Panel 5 | 13.2 %* | 9.2 % | 12.9 % | 8.5 % | 9.7 % | 7.2 % | 6.5 %* |
| Panel 6 | 8.9 %* | 7.6 % | 8.2 % | 7.0 % | 6.0 % | 4.7 % | 4.3 %* |
| Panel 7 | 3.8 %* | 3.3 % | 3.3 % | 2.9 % | 2.1 % | 1.4 % | 1.2 %* |
| Panel 8 | 11.4 %* | 8.1 % | 11.1 % | 7.5 % | 8.4 % | 6.3 % | 5.6 %* |
| Panel 9 | 7.3 %* | 6.4 % | 6.7 % | 6.0 % | 5.0 % | 4.0 % | 3.7 %* |

*: Result shown or inferred in Figure 4.1b.

Table I.2 – Per-panel shading index values for east roof orientation

| Panel # | Ref (3 BPDs per module) | 5 BPDs (V) | 6 BPDs | 10 BPDs (V) | 12 BPDs | 30 BPDs | 60 BPDs |
|---|---|---|---|---|---|---|---|
| No shade | 0.0 % | 0.0 % | 0.0 % | 0.0 % | 0.0 % | 0.0 % | 0.0 % |
| Panel 1 | 5.2 %* | 4.2 % | 4.6 % | 3.8 % | 3.5 % | 2.5 % | 2.2 %* |
| Panel 2 | 0.3 %* | 0.3 % | 0.3 % | 0.3 % | 0.2 % | 0.2 % | 0.2 %* |
| Panel 3 | 0.2 %* | 0.1 % | 0.1 % | 0.1 % | 0.1 % | 0.1 % | 0.0 %* |
| Panel 4 | 2.3 %* | 1.9 % | 2.1 % | 1.7 % | 1.6 % | 1.2 % | 1.0 %* |
| Panel 5 | 1.4 %* | 1.0 % | 1.3 % | 0.9 % | 0.9 % | 0.6 % | 0.5 %* |
| Panel 6 | 0.7 %* | 0.7 % | 0.7 % | 0.7 % | 0.6 % | 0.5 % | 0.4 %* |
| Panel 7 | 4.2 %* | 3.7 % | 3.6 % | 3.3 % | 2.4 % | 1.6 % | 1.3 %* |
| Panel 8 | 15.3 %* | 10.6 % | 14.7 % | 9.4 % | 10.9 % | 7.7 % | 6.7 %* |
| Panel 9 | 14.2 %* | 10.9 % | 13.5 % | 10.1 % | 10.4 % | 7.8 % | 7.0 %* |

*: Result shown or inferred in Figure 4.2a.

Table I.3 – Per-panel shading index values for west roof orientation

| Panel # | Ref (3 BPDs per module) | 5 BPDs (V) | 6 BPDs | 10 BPDs (V) | 12 BPDs | 30 BPDs | 60 BPDs |
|---|---|---|---|---|---|---|---|
| No shade | 0.0 % | 0.0 % | 0.0 % | 0.0 % | 0.0 % | 0.0 % | 0.0 % |
| Panel 1 | 0.0 %* | 0.0 % | 0.0 % | 0.0 % | 0.0 % | 0.0 % | 0.0 %* |
| Panel 2 | 0.2 %* | 0.2 % | 0.2 % | 0.2 % | 0.1 % | 0.1 % | 0.1 %* |
| Panel 3 | 11.3 %* | 8.3 % | 9.2 % | 7.0 % | 6.1 % | 3.6 % | 2.9 %* |
| Panel 4 | 5.9 %* | 5.0 % | 5.1 % | 4.4 % | 3.3 % | 2.2 % | 1.9 %* |
| Panel 5 | 20.7 %* | 14.1 % | 20.0 % | 12.5 % | 15.2 % | 10.6 % | 9.2 %* |
| Panel 6 | 17.0 %* | 13.2 % | 16.1 % | 12.2 % | 12.2 % | 9.3 % | 8.4 %* |
| Panel 7 | 3.0 %* | 2.7 % | 2.7 % | 2.5 % | 2.2 % | 1.6 % | 1.4 %* |
| Panel 8 | 1.3 %* | 1.1 % | 1.1 % | 1.0 % | 0.8 % | 0.6 % | 0.5 %* |
| Panel 9 | 0.9 %* | 0.8 % | 0.8 % | 0.8 % | 0.7 % | 0.6 % | 0.5 %* |

*: Result shown or inferred in Figure 4.2e.

Table I.4 – Per-panel shading index values for southeast roof orientation

| Panel # | Ref (3 BPDs per module) | 5 BPDs (V) | 6 BPDs | 10 BPDs (V) | 12 BPDs | 30 BPDs | 60 BPDs |
|---|---|---|---|---|---|---|---|
| No shade | 0.0 % | 0.0 % | 0.0 % | 0.0 % | 0.0 % | 0.0 % | 0.0 % |
| Panel 1 | 2.9 %* | 2.9 % | 2.5 % | 2.7 % | 1.9 % | 1.6 % | 1.5 %* |
| Panel 2 | 0.3 %* | 0.2 % | 0.2 % | 0.2 % | 0.2 % | 0.1 % | 0.1 %* |
| Panel 3 | 4.0 %* | 2.5 % | 3.2 % | 2.0 % | 2.0 % | 1.1 % | 0.8 %* |
| Panel 4 | 4.3 %* | 3.7 % | 3.8 % | 3.3 % | 2.5 % | 1.8 % | 1.6 %* |
| Panel 5 | 8.0 %* | 5.4 % | 7.8 % | 5.0 % | 6.1 % | 4.4 % | 3.9 %* |
| Panel 6 | 3.1 %* | 2.4 % | 2.7 % | 2.1 % | 1.7 % | 1.1 % | 0.9 %* |
| Panel 7 | 3.5 %* | 3.0 % | 2.9 % | 2.7 % | 1.9 % | 1.2 % | 1.0 %* |
| Panel 8 | 13.2 %* | 9.3 % | 12.7 % | 8.5 % | 9.7 % | 7.1 % | 6.3 %* |
| Panel 9 | 10.4 %* | 8.6 % | 9.8 % | 8.0 % | 7.6 % | 6.1 % | 5.6 %* |

*: Result shown or inferred in Figure Ja.

Table I.5 – Per-panel shading index values for southwest roof orientation

| Panel # | Ref (3 BPDs per module) | 5 BPDs (V) | 6 BPDs | 10 BPDs (V) | 12 BPDs | 30 BPDs | 60 BPDs |
|---|---|---|---|---|---|---|---|
| No shade | 0.0 % | 0.0 % | 0.0 % | 0.0 % | 0.0 % | 0.0 % | 0.0 % |
| Panel 1 | 0.1 %* | 0.1 % | 0.1 % | 0.1 % | 0.0 % | 0.0 % | 0.0 %* |
| Panel 2 | 0.2 %* | 0.2 % | 0.1 % | 0.1 % | 0.1 % | 0.1 % | 0.1 %* |
| Panel 3 | 8.8 %* | 6.5 % | 7.2 % | 5.6 % | 4.8 % | 3.0 % | 2.5 %* |
| Panel 4 | 4.2 %* | 3.5 % | 3.6 % | 3.0 % | 2.2 % | 1.3 % | 1.1 %* |
| Panel 5 | 15.6 %* | 10.7 % | 15.2 % | 9.7 % | 11.6 % | 8.2 % | 7.2 %* |
| Panel 6 | 11.8 %* | 9.8 % | 11.2 % | 9.1 % | 8.7 % | 7.0 % | 6.5 %* |
| Panel 7 | 3.9 %* | 3.6 % | 3.4 % | 3.3 % | 2.4 % | 1.8 % | 1.5 %* |
| Panel 8 | 6.3 %* | 4.3 % | 6.1 % | 3.9 % | 4.6 % | 3.3 % | 3.0 %* |
| Panel 9 | 2.1 %* | 1.7 % | 1.8 % | 1.5 % | 1.1 % | 0.8 % | 0.6 %* |

*: Result shown or inferred in Figure Jb.

## Annex J – Other orientation sensitivity results

The results for the south-east and south-west roof orientation are outlined below. Note that the south-east results encompass behavior falling in between the east and south roof orientation cases. Similarly the south-west results lie in between the results of the west and south house roof orientation cases.

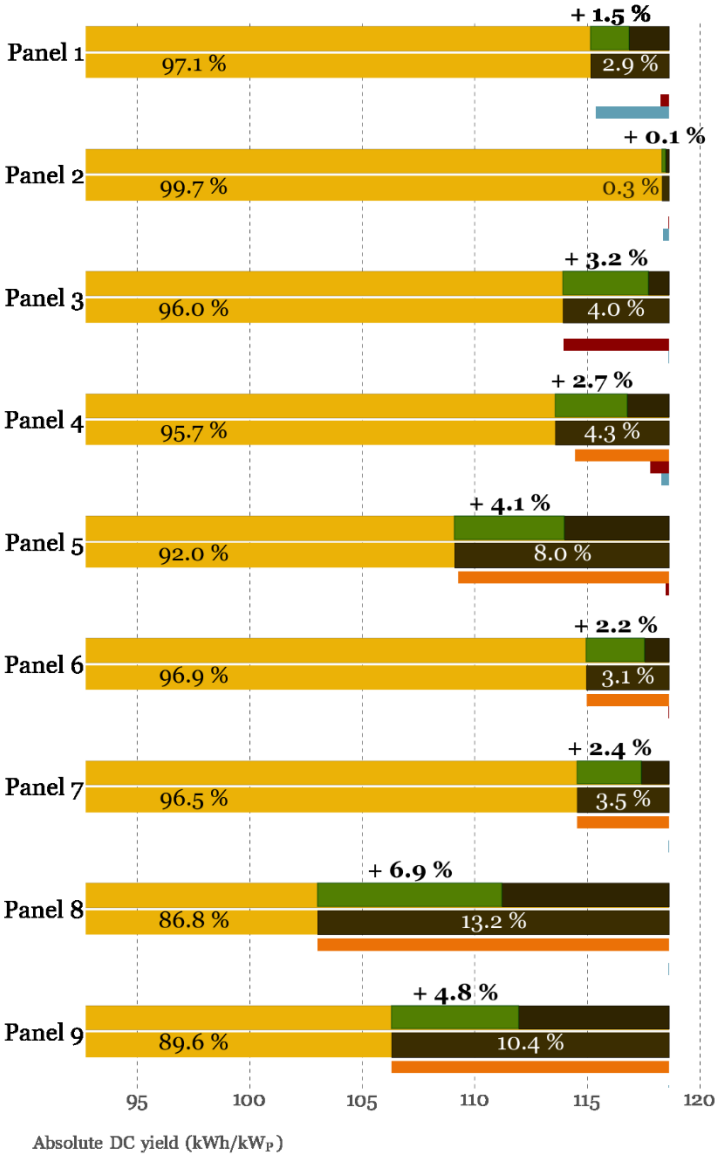


*Figure Ja: Southeast-oriented roof TMY DC yield per panel, shading index values and potential benefits when the amount of BPDs per module is increased from 3 to 60. Figure 4.1a shows the legend.*

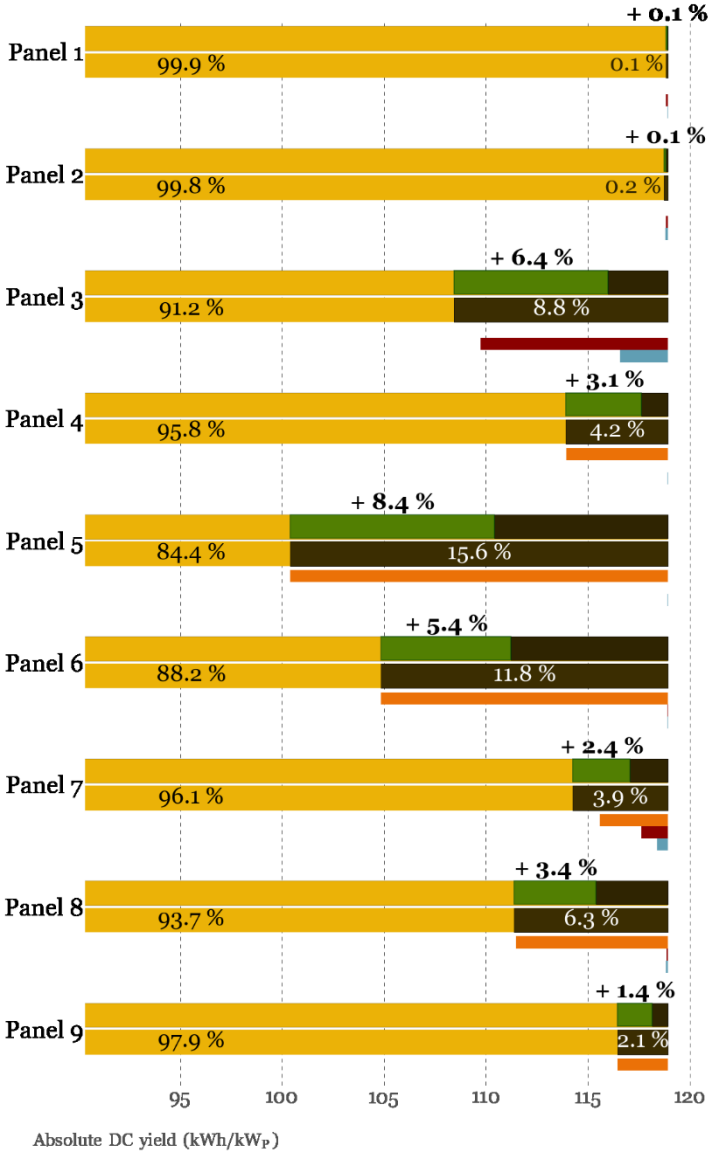


*Figure Jb: Southwest-oriented roof TMY DC yield per panel, shading index values and potential benefits when the amount of BPDs per module is increased from 3 to 60. Figure 4.1a shows the legend.*

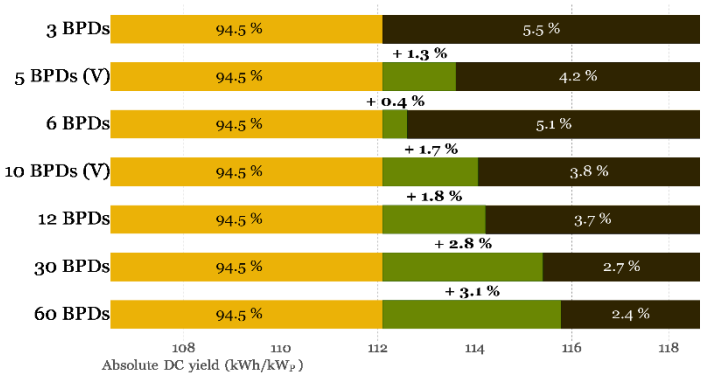


*Figure Jc: Southeast-oriented roof TMY DC yield results averaged over the nine panels. Shading index values and potential benefits when increasing the amount of BPDs per module are illustrated. Figure 4.1a shows the accompanying legend.*

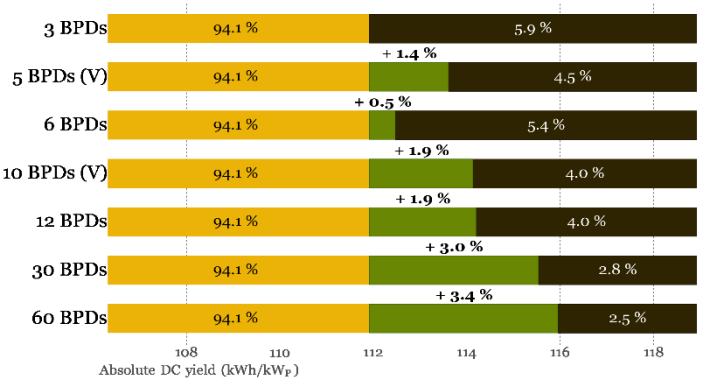


*Figure Jd: Southwest-oriented roof TMY DC yield results averaged over the nine panels. Shading index values and potential benefits when increasing the amount of BPDs per module are illustrated. Figure 4.1a shows the accompanying legend.*

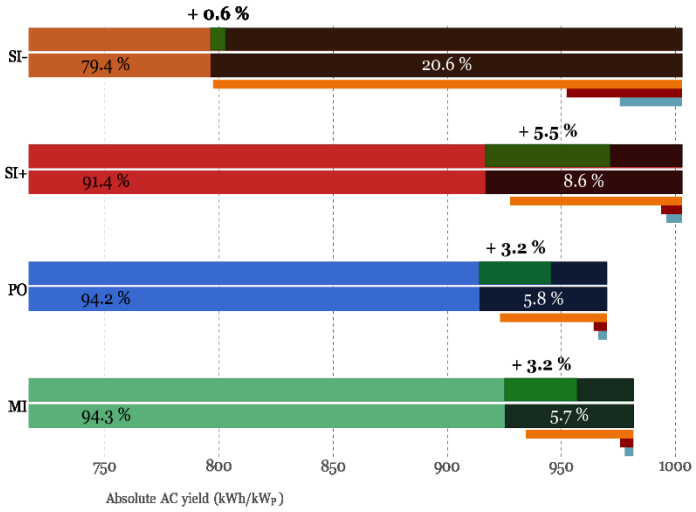


*Figure Je: Southeast roof TMY AC yield, shading index values and potential benefits when increasing the amount of BPDs per module from 3 to 60 for string inverter with inactive (SI-) and active shadow function (SI+), power optimizer (PO) and micro-inverter (MI) system architectures. The legend is shown in Figure 4.1d.*

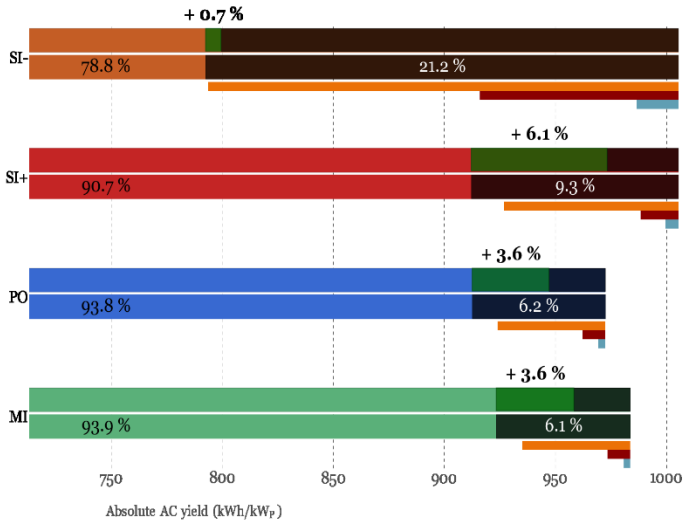


*Figure Jf: Southwest roof TMY AC yield, shading index values and potential benefits when increasing the amount of BPDs per module from 3 to 60 for string inverter with inactive (SI-) and active shadow function (SI+), power optimizer (PO) and micro-inverter (MI) system architectures. The legend is shown in Figure 4.1d.*

Table J.1 – SE DC-averaged + per-system shade mitigation factor values for each BPD case

| System | Ref. of 3 BPDs | 5 BPDs (V) | 6 BPDs | 10 BPDs (V) | 12 BPDs | 30 BPDs | 60 BPDs |
|---|---|---|---|---|---|---|---|
| DC-avg. | - | 19 % | 6 % | 25 % | 27 % | 42 % | 46 % |
| SI - | - | 1 % | 1 % | 2 % | 2 % | 3 % | 3 % |
| SI + | - | 32 % | 10 % | 39 % | 42 % | 59 % | 64 % |
| PO | - | 23 % | 8 % | 30 % | 32 % | 51 % | 56 % |
| MI | - | 23 % | 8 % | 30 % | 33 % | 51 % | 56 % |

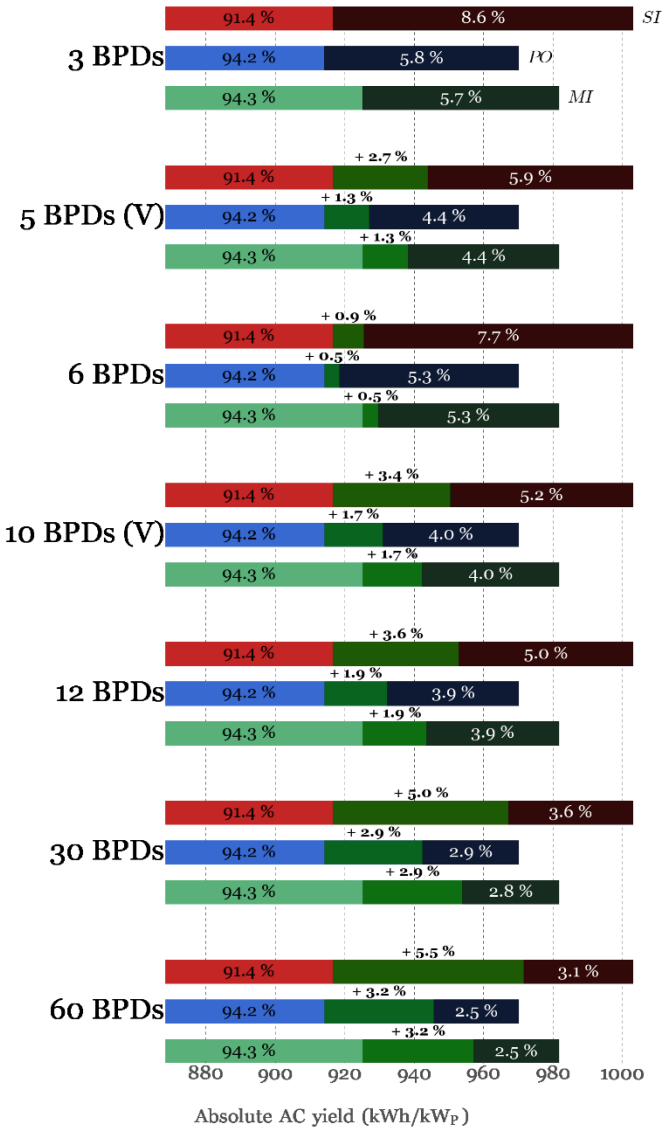


*Figure Jg: Southeast roof TMY AC yield results for SI(+), PO and MI systems. Shading index values and potential benefits when increasing the amount of BPDs per module in a stepwise fashion from 3 to 60 are illustrated. The legend is shown in Figure 4.1d.*

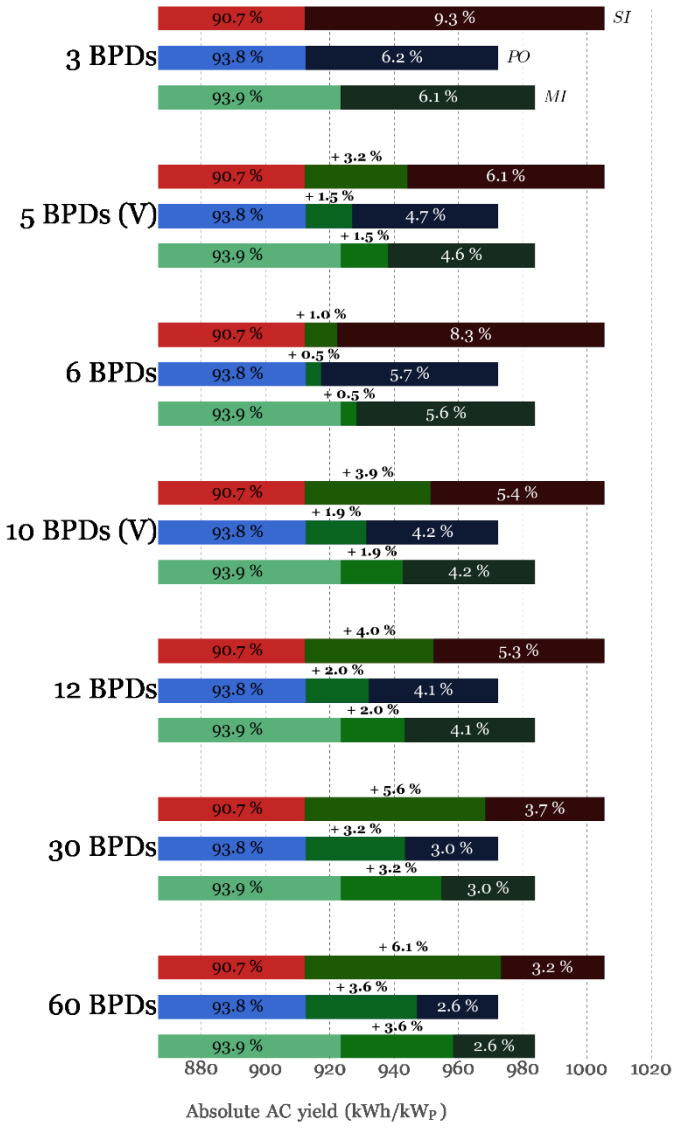


*Figure Jh: Southwest roof TMY AC yield results for SI(+), PO and MI systems. Shading index values and potential benefits when increasing the amount of BPDs per module in a stepwise fashion from 3 to 60 are illustrated. The legend is shown in Figure 4.1d.*

Table J.2 – SW DC-averaged + per-system shade mitigation factor values for all BPD cases

| System | Ref. of 3 BPDs | 5 BPDs (V) | 6 BPDs | 10 BPDs (V) | 12 BPDs | 30 BPDs | 60 BPDs |
|---|---|---|---|---|---|---|---|
| DC-avg. | - | 21 % | 7 % | 28 % | 28 % | 45 % | 51 % |
| SI - | - | 2 % | 1 % | 2 % | 2 % | 3 % | 3 % |
| SI + | - | 34 % | 11 % | 42 % | 43 % | 60 % | 65 % |
| PO | - | 24 % | 8 % | 32 % | 33 % | 52 % | 58 % |
| MI | - | 24 % | 8 % | 32 % | 33 % | 52 % | 58 % |

## Annex K – Other geographic sensitivity results

The geographic sensitivity results for Oslo and Paris are shown here in Figures Ka through Kd. Tables K.1 and K.2 show the shade mitigation factor values for Oslo and Paris respectively. Note that the general trends are strongly similar to those explained in the Results chapter.

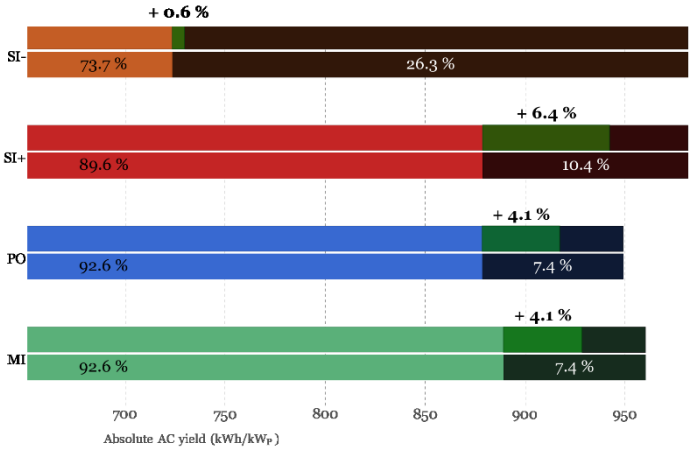


*Figure Ka: Oslo TMY AC yield, shading index values and potential benefits when increasing the amount of BPDs per module from 3 to 60 for string inverter with inactive (SI-) and active shadow function (SI+), power optimizer (PO) and micro-inverter (MI) system architectures. The legend is shown in Figure 4.1d.*

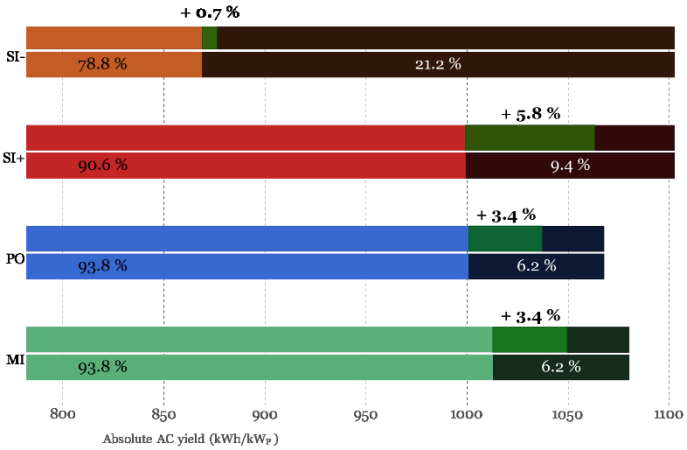


*Figure Kb: Paris TMY AC yield, shading index values and potential benefits when increasing the amount of BPDs per module from 3 to 60 for string inverter with inactive (SI-) and active shadow function (SI+), power optimizer (PO) and micro-inverter (MI) system architectures. The legend is shown in Figure 4.1d.*

Table K.1 – Oslo per-system shade mitigation factor values for all BPD cases

| System | Ref. of 3 BPDs | 5 BPDs (V) | 6 BPDs | 10 BPDs (V) | 12 BPDs | 30 BPDs | 60 BPDs |
|---|---|---|---|---|---|---|---|
| SI - | - | 1 % | 1 % | 1 % | 2 % | 2 % | 2 % |
| SI + | - | 28 % | 11 % | 35 % | 41 % | 57 % | 62 % |
| PO | - | 21 % | 8 % | 27 % | 32 % | 50 % | 55 % |
| MI | - | 21 % | 8 % | 28 % | 33 % | 50 % | 55 % |

Table K.2 – Paris per-system shade mitigation factor values for all BPD cases

| System | Ref. of 3 BPDs | 5 BPDs (V) | 6 BPDs | 10 BPDs (V) | 12 BPDs | 30 BPDs | 60 BPDs |
|---|---|---|---|---|---|---|---|
| SI - | - | 1 % | 1 % | 2 % | 2 % | 3 % | 3 % |
| SI + | - | 29 % | 11 % | 36 % | 41 % | 57 % | 62 % |
| PO | - | 20 % | 8 % | 27 % | 31 % | 49 % | 54 % |
| MI | - | 20 % | 8 % | 27 % | 32 % | 49 % | 55 % |

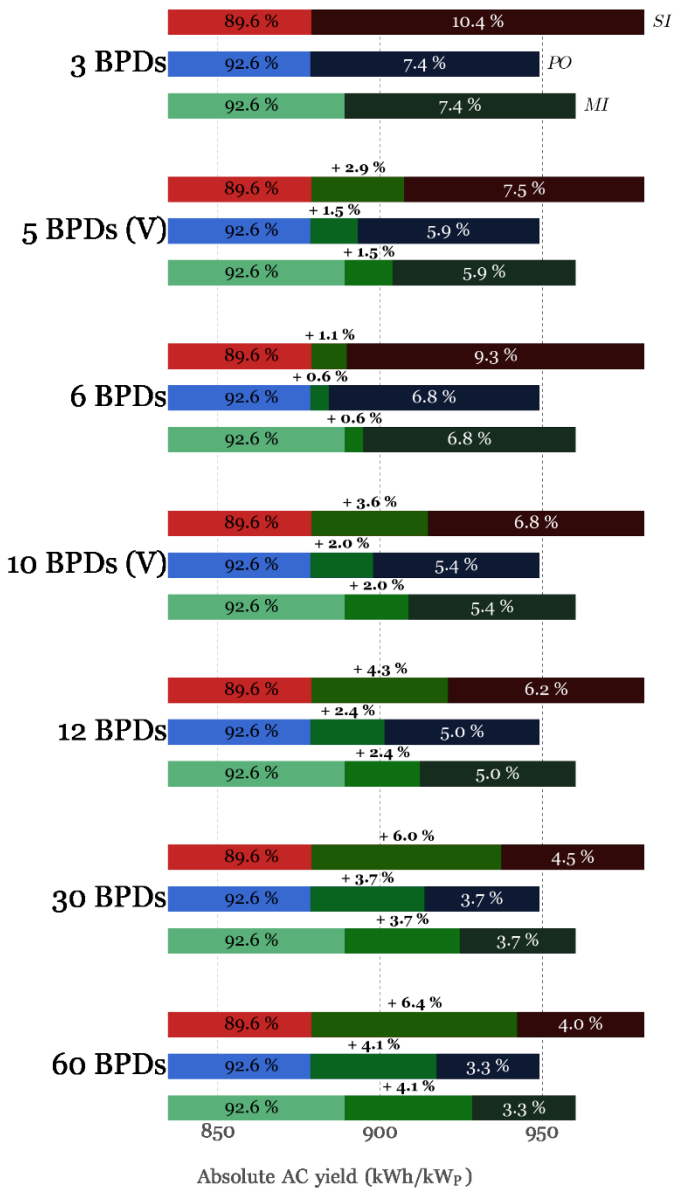


*Figure Kc: Oslo TMY AC yield results for SI(+), PO and MI systems. Shading index values and potential benefits when increasing the amount of BPDs per module in a stepwise fashion from 3 to 60 are illustrated. The legend is shown in Figure 4.1d.*

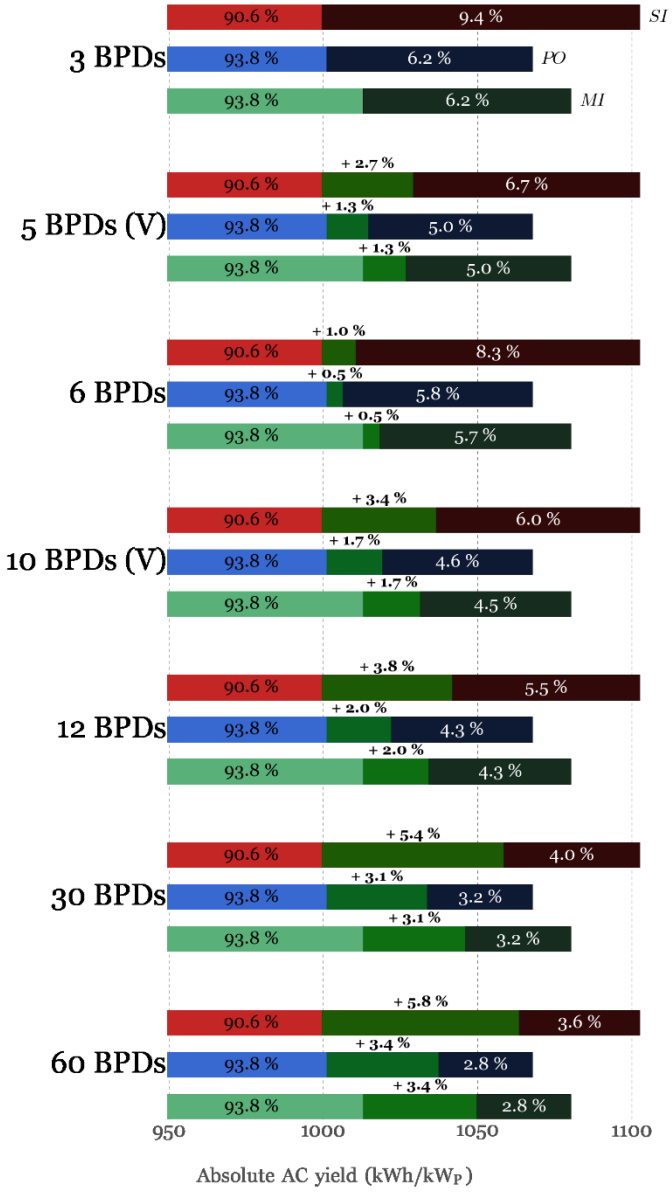


*Figure Kd: Paris TMY AC yield results for SI(+), PO and MI systems. Shading index values and potential benefits when increasing the amount of BPDs per module in a stepwise fashion from 3 to 60 are illustrated. The legend is shown in Figure 4.1d.*

## Annex L – Model validation graphs

Additional information on the model validation results are illustrated here. Figures La, Lb and Lc show minutely validation results for the updated and previous yield models and actual yield data.

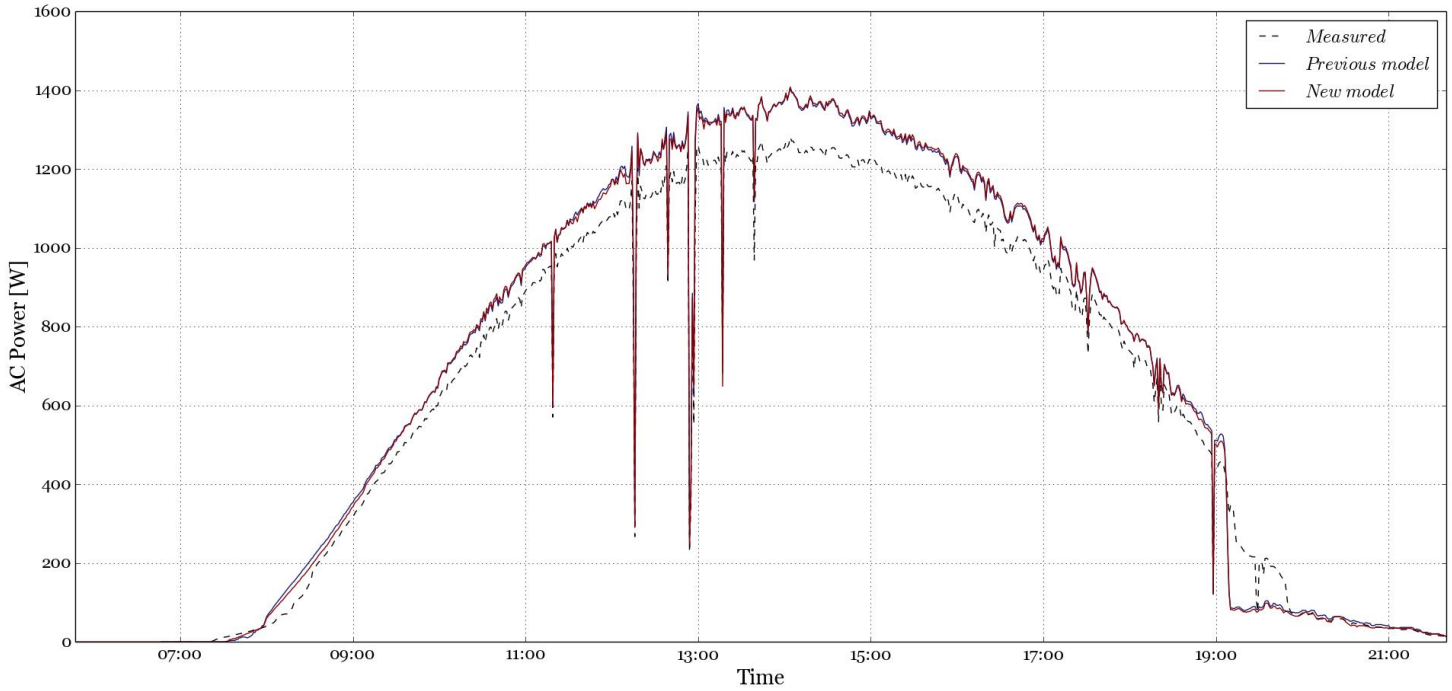


*Figure La: Simulated and measured Heliox system yield for a clear day (July 17th 2015). Red indicates the minutely results for the updated model, blue does so for the previous yield model. Measured minutely data is shown using dashed black lines.*

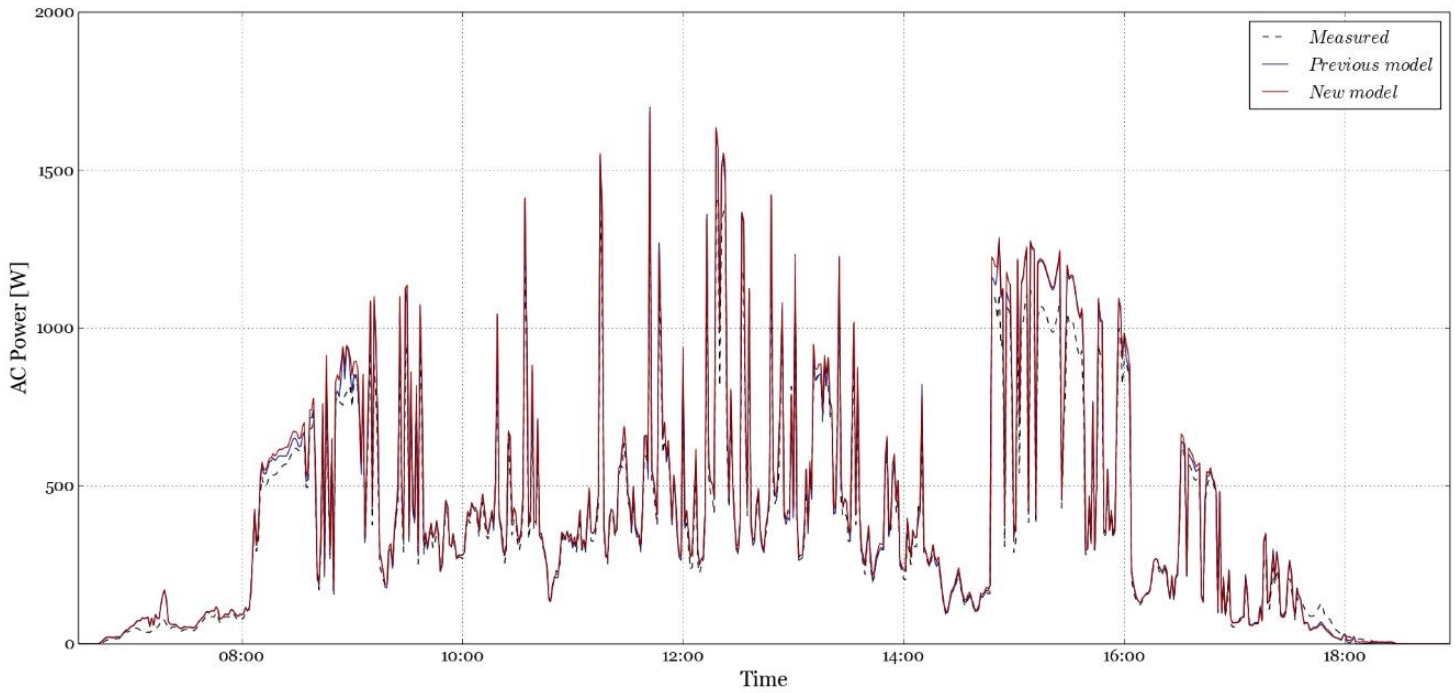


*Figure Lb: Simulated and measured Heliox system yield for a partly clouded day (March 27th 2015). Red indicates the minutely results for the updated model, blue does so for the previous yield model. Measured minutely data is shown using dashed black lines.*

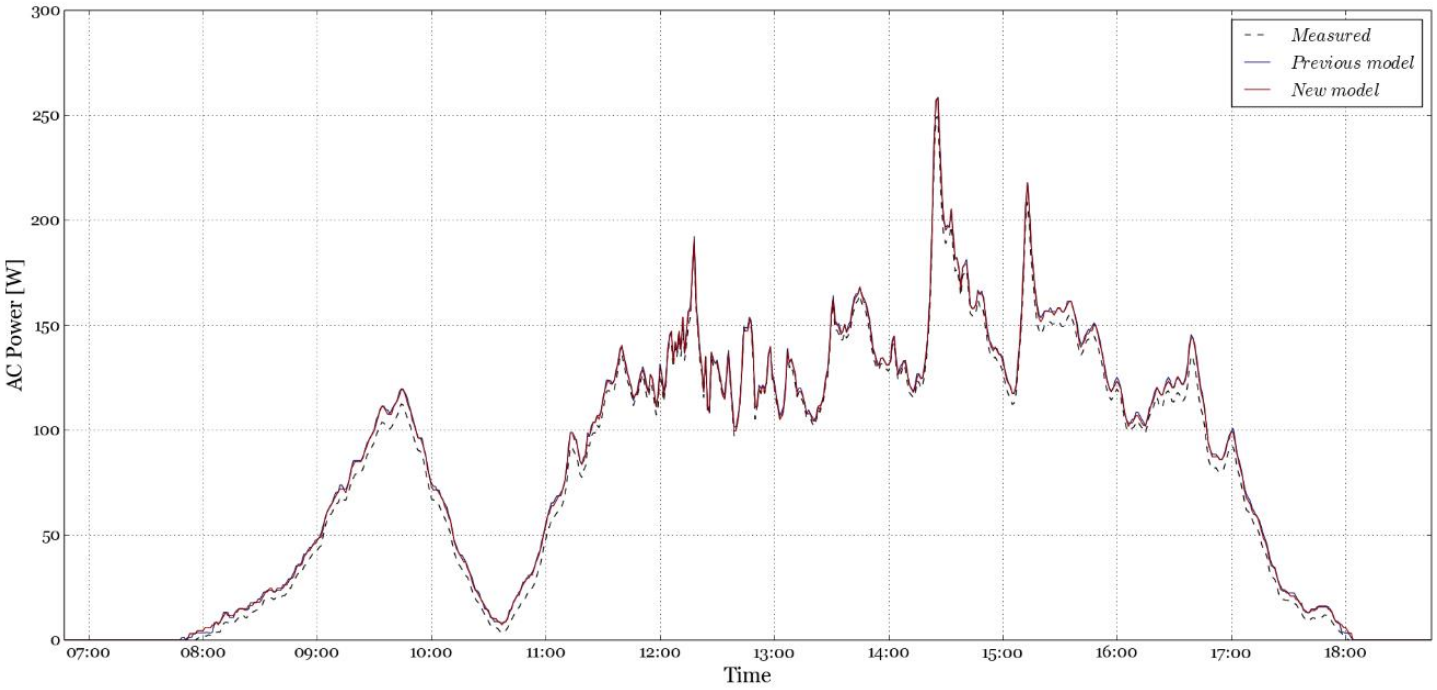


*Figure Lc: Simulated and measured Heliox system yield for an overcast day (March 20th 2015). Red indicates the minutely results for the updated model, blue does so for the previous yield model. Measured minutely data is shown using dashed black lines.*

The deviation of the updated model yield with respect to that of the former version (Sinapis, et al., in press) is determined as follows:

$$Model\ dev. = 100\% \cdot (E_{sim,new} - E_{sim,old})/E_{sim,old} \quad \text{(L.1)}$$

The deviation of the updated model yield with respect to the real measured yield is calculated as follows:

$$Meas.dev. = 100\% \cdot (E_{sim,new} - E_{measured})/E_{measured} \quad \text{(L.2)}$$

Table L.1 shows the values of these deviations as expressed in Equations L.1 and L.2.

Table L.1 – Heliox daily system yield values resulting from validation procedure

| | **New simulation** | **Previous simulation** | **Measured value** | **Model dev.** | **Meas. dev.** |
|---|---|---|---|---|---|
| *CLEAR DAY – 17-07-2015* | | | | | |
| | 10.5778 kWh | 10.6006 kWh | 9.8601 kWh | | |
| | | | | - 0.215 % | + 6.78 % |
| *OVERCAST DAY – 20-03-2015* | | | | | |
| | 0.96911 kWh | 0.97466 kWh | 0.92137 kWh | | |
| | | | | - 0.569 % | + 5.18 % |
| *PARTLY CLOUDED DAY – 27-03-2015* | | | | | |
| | 5.02334 kWh | 5.04710 kWh | 4.59240 kWh | | |
| | | | | - 0.471 % | + 9.38 % |